



저작자표시-비영리-변경금지 2.0 대한민국

이용자는 아래의 조건을 따르는 경우에 한하여 자유롭게

- 이 저작물을 복제, 배포, 전송, 전시, 공연 및 방송할 수 있습니다.

다음과 같은 조건을 따라야 합니다:



저작자표시. 귀하는 원저작자를 표시하여야 합니다.



비영리. 귀하는 이 저작물을 영리 목적으로 이용할 수 없습니다.



변경금지. 귀하는 이 저작물을 개작, 변형 또는 가공할 수 없습니다.

- 귀하는, 이 저작물의 재이용이나 배포의 경우, 이 저작물에 적용된 이용허락조건을 명확하게 나타내어야 합니다.
- 저작권자로부터 별도의 허가를 받으면 이러한 조건들은 적용되지 않습니다.

저작권법에 따른 이용자의 권리는 위의 내용에 의하여 영향을 받지 않습니다.

이것은 [이용허락규약\(Legal Code\)](#)을 이해하기 쉽게 요약한 것입니다.

[Disclaimer](#)

이학박사학위논문

Glacial History and Depositional Changes
in the Arctic Ocean after the Middle Pleistocene Transition
based on Seafloor Morphology, High-resolution
Seismostratigraphy, and Lithostratigraphy

해저지형, 고해상 탄성파층서 및 암층서를 이용한 중기
플라이스토세 전이기 이후 북극해 빙하역사 및 퇴적환경 변화

제주대학교 대학원

지구해양과학과

조 영 진

2022년 8월

**Glacial History and Depositional Changes
in the Arctic Ocean after the Middle Pleistocene
Transition based on Seafloor Morphology, High-
resolution Seismostratigraphy, and
Lithostratigraphy**

지도교수 윤 석 훈

조 영 진

이 논문을 이학 박사학위 논문으로 제출함

2022 년 8 월

조영진의 이학 박사학위 논문을 인준함

심사위원장	문재홍	(인)
위 원	윤석훈	(인)
위 원	남승일	(인)
위 원	우경식	(인)
위 원	장광철	(인)

제주대학교 대학원

2022 년 8 월

**Glacial History and Depositional Changes
in the Arctic Ocean after the Middle Pleistocene
Transition based on Seafloor Morphology, High-
resolution Seismostratigraphy, and
Lithostratigraphy**

Young Jin Joe
(Supervised by professor Seok-Hoon Yoon)

A thesis submitted in partial fulfillment of the requirement for
the degree of Doctor of Science

2022. 8

This thesis has been examined and approved.

Thesis director, Jae-Hong Moon, Jeju National University

Seok-Hoon Yoon, Jeju National University

Seung-Il Nam, Korea Polar Research Institute

Kyung Sik Woo, Kangwon National University

Kwangchul Jang, Korea Polar Research Institute

2022. 8

Department of Earth and Marine Sciences
GRADUATE SCHOOL
JEJU NATIONAL UNIVERSITY

CONTENTS

LIST OF TABLES	II
LIST OF FIGURES	III
ABSTRACT	VI
Chapter 1. Introduction	1
1.1. Backgrounds	
1.2. Reconstruction of the Arctic glaciations	
1.3. Objectives	
CHAPTER 2. Glacial history and depositional environments in the Little Storfjorden and Hambergbukta since the Younger Dryas	16
CHAPTER 3. Late Quaternary depositional and glacial history of the Arliss Plateau off the East Siberian margin in the western Arctic Ocean	55
CHAPTER 4. The repeated occurrences of a km-thick East Siberian marine ice sheet (ESIS) over the last 300 ka	81
CHAPTER 5. Conclusions	111
References	115
국문요지	126
감사의 글	130

LIST OF TABLES

Table 1.1. List of multiple core measurements conducted in this thesis.	15
Table 1.2. List of geophysical surveys and sediment coring conducted in study areas.	15
Table 2.1. Information on the cores investigated in this study.....	25
Table 2.2. AMS ¹⁴ C dates and calibrated dates for the studied cores.....	26
Table 2.3. Classified acoustic units (see Figs. 4 and 5 for their distribution).	33
Table 2.4. Lithofacies classified on the studied cores.	39
Table 3.1. Summary of lithofacies in core ARA02B/16B-GC. Black arrows indicate the intervals of TLm, TLs, and Hm facies. See Fig. 3.4 for the stratigraphic distribution of lithofacies.	67
Table 3.2. Estimated duration and sedimentation rates of lithostratigraphic units in core ARA02B/16B-GC based on the age model developed from lithostratigraphic correlations.	72
Table 4.1. Information of studied and referenced cores.	86

LIST OF FIGURES

Figure 1.1. Variations in the generalized benthic oxygen isotope reflecting the global climate evolution of the last 5 Ma (Tiedemann et al., 1994). This figure was taken from Stein (2008) and slightly modified. MPT indicates the Middle Pleistocene Transition.	3
Figure 1.2. Late Quaternary maximum configuration of the Arctic ice sheets (from Batchelor et al., 2019).	4
Figure 1.3. (A) A maximum reconstruction of the late-Würm Arctic Ice Sheet by Hughes et al. (1977). (B) The km-thick Arctic ice shelf condition during MIS 6 proposed by Jakobsson et al. (2016).	6
Figure 1.4. Sources of the empirical data to reconstruct the Arctic ice sheet configurations for six time-slices from Batchelor et al. (2019).	7
Figure 1.5. Glagigenic submarine landforms formed by the advance and retreat of the marine-based glaciers. This figure was taken from Batchelor and Dowdeswell (2015).	9
Figure 1.6. Schematic model of glacier-induced depositional processes (referred to Laberg and Vorren, 1995; Hesse et al., 1996).	11
Figure 2.1. Physiographic map of Arctic Ocean and Svalbard located in the east of Fram Strait (FS).	18
Figure 2.2. Zoom-in on Little Storfjorden and Hambergbukta.	21
Figure 2.3. Multi-beam bathymetry of Hambergbukta and a downstream region (Little Storfjorden).	28
Figure 2.4. Distribution of acoustic units (F-1 to F-4) re-defined in this study.	30
Figure 2.5. SBP profile (053 line) around the fjord mouth showing a grounding zone wedge below the TMC and the associated debris lobe.	31
Figure 2.6. Seismostratigraphies defined in (A) Noormets et al. (2021) and (B) this study.	32
Figure 2.7. Linescan images, X-radiographs, downcore distribution of lithofacies (Facies 1-5), physical properties (WBD and MS), the calendar ages of AMS ¹⁴ C dates, and grain size, including the content of coarse particles larger than 63 μm, and elemental geochemistry.	35

Figure 2.8. Comparison of sedimentation rates between Little Storfjorden (core 905) and eastern Storfjorden (HH12-1209-GC) based on the age model applying to the Marine 20 dataset (Heaton et al., 2020) and a regional ΔR of -61 ± 37 (Pieńkowski et al., 2021).	41
Figure 2.9. Downcore distribution of organic carbon stable isotope values ($\delta^{13}C$), TOC, TOC/ N_{org} and N_{org}	42
Figure 2.10. Correlation of the acoustic units with lithofacies of core 905 from Little Storfjorden.	44
Figure 2.11. Reconstruction of depositional environment and glacial history in the Hambergbukta and Little Storfjorden since Younger Dryas.	49
Figure 2.12. Comparison between the LIA maximum extents suggested by this study and Noormets et al. (2021).	52
Figure 3.1. (A) (A) Index physiographic map of the study area showing the location of cores ARA02B/16B-GC (this study), ARA03B/28B-GC (Schreck et al., 2018), and HLY0503-8JPC (Adler et al., 2009). MR, Mendeleev Ridge; AP, Arliss Plateau; CB, Chukchi Basin; CP, Chukchi Plateau; NR, Northwind Ridge. The solid line tracks sub-bottom profiler data. The bathymetric contour interval is 250 m. (B) Broader physiographic/paleogeographic context with inferred ice-sheet maxima shown by semi-transparent white fill (Svendsen et al., 2004; Niessen et al., 2013; Stokes et al., 2016). (C) Multibeam bathymetry of the Arliss Plateau shows several generations of Mega-Scale Glacial Lineations. The bathymetric contour interval is 100 m.	57
Figure 3.2. Sub-bottom profiler from Arliss Plateau to Chukchi Basin across the site of core ARA02B/16B-GC (red vertical bar in panel B).	59
Figure 3.3. Down-core distribution of sediment lightness (L^*), Mn/Al and Ca/Al ratios, IRD numbers, and grain size in core ARA02B/16B-GC.	63
Figure 3.4. Split-core photos, X-radiograph images, and lithofacies (see Table 3.1 for details). Indices for lithological units (B1-B5 and G1-G4) and the detrital carbonate layer W3 are shown on the core photo.	68
Figure 3.5. Lithostratigraphic correlation of core ARA02B/16B-GC with ARA03B/28B-GC (Schreck et al., 2018) and HLY0503-8JPC (Adler et al., 2009) based on sediment color and variations of Mn/Al and Ca/Al.	71
Figure 3.6. Correlation of the sub-bottom data with core ARA02B/16B-GC. Surficial reflector R1 is the seafloor. Strong reflectors R2 and R3 correspond to prominent lithological changes at the boundaries of fine-grained sediments and IRD-rich layers W3 and PW2. Estimated marine isotope stages are shown on the right.	74

Figure 3.7. Schematic model of sedimentary processes on the Arliss Plateau and adjacent Chukchi Basin during major depositional regimes from the MIS 4 glaciation to the Holocene.	79
Figure 4.1. A) Bathymetry of the East Siberian and Chukchi margins. Three arrows indicate estimated ice flow directions by the Laurentide Ice Sheet (pink) and East Siberian and Chukchi Seas Ice Sheet (gray and black). The Yellow line shows the SBP track line during the ARA06C cruise. For the X-X' cross-section (red line), the SBP profile is shown in Fig 4.2. In the upper right panel, the maximum extent of the Late Quaternary Arctic ice sheets was mapped using the MIS 12 maximum model from Batchelor et al. (2019). (B) Streamlined glacial lineations (SGLs) and recessional moraines on the western Chukchi Rise were defined by Kim et al. (2020). (C) Several sets of SGLs and debris lobes on the Arliss Plateau and adjacent area were introduced by Niessen et al. (2013). Yellow and white circles indicate the locations of the studied and referenced cores (Table 4.1).	83
Figure 4.2. High-resolution sub-bottom profile from the Chukchi Rise to Kucherov Terrace with the seismostratigraphic units (SSUs) defined in this study.	89
Figure 4.3. Results of multiple lithostratigraphic measurements for ARA06C/04JPC (see Fig. 4.4 for details of lithofacies). Brown stars indicate IRD-rich layers with relatively high values of Ca/Sr ratio.	92
Figure 4.4. Core surface images, x-radiographs, and lithofacies of ARA06C/04JPC.	93
Figure 4.5. Lithostratigraphy of two cores ST13 and ST08 based on stratigraphic correlation with core 04JPC and a reference core (ARA02B/16B-GC) (Joe et al., 2020).	95
Figure 4.6. Distribution of dolomite, Plagioclase, kaolinite, , and illite in core 04JPC. $K_{\text{clay sum}}$ and $I_{\text{clay sum}}$ indicate kaolinite and illite portions of the sum of four major clay mineral groups (illite, kaolinite, chlorite, and smectite).	97
Figure 4.7. The age model for core 04JPC based on correlation with cores HLY0503-8JPC and ARC6-C22 (Xiao et al., 2020; Wang et al., 2021).	99
Figure 4.8. Core-seismic correlations based on down-core variations in acoustic impedance of core 04JPC (A) and sand to gravel content ($>63 \mu\text{m}$) of core ST13 (B).	102
Figure 4.9. For core 04JPC, Mn/Fe, Ca/Sr, and mineral composition time series. LR04 $\delta^{18}\text{O}$ was referred by Lisiecki and Raymo (2005).	106
Figure 4.10. Ice configuration of ESIS and ice shelf extending from LIS since MIS 8.	109

ABSTRACT

The climate-sensitive Arctic Ocean is the best place to understand global climate changes. In the Arctic Ocean, continental ice sheets and marine-based glaciers have played an important role in regulating the global climate and sea level in the past, and thus reconstruction of the Arctic glacial history is necessary to better understand the past climate changes. The purpose of this thesis is to reconstruct precisely the glacial history and glacier-induced depositional environments in the Arctic Ocean during the Late Quaternary based on detailed bathymetry, high-resolution seismostratigraphy, and lithostratigraphy/lithofacies of studied sediment cores. This thesis dealt with the glacial history of centennial to millennial and orbital timescales.

The first study reconstructed the glacial history and depositional environments in the Little Storfjorden and its tributary, Hambergbukta, in southeastern Svalbard since the Younger Dryas (YD) on centennial to millennial timescales. Combined with seismostratigraphy and age-constrained sediment cores, the sediment records in Hambergbukta represent glacimarine sediments deposited after 1900 years. A sediment core HH19-905-GC taken from Little Storfjorden contains the glacial sediments deposited during the Younger Dryas (YD). Little Storfjorden bathymetry shows two NE-SW-oriented ridges (R1, R2) in the vicinity of Hambergbukta. The core-seismic integration presents that a glacial diamicton at the bottom of core 905 corresponds to the top of R2. This suggests that R2 represents the marginal position of the marine-based glacier in Little Storfjorden during YD. Based on sediment records of core 905, the marine-based glacier in Little Storfjorden rapidly melted out during the early Holocene. In this condition, winnowing by strong bottom currents led to very low sedimentation rates during the late period of the early to middle Holocene. During

the late Holocene, Little Storfjorden was most likely influenced by seasonal sea ice. Noticeable advances (or surges) and retreats of tidewater glaciers in coastal tributary fjords including Hambergbukta were identified as the deposition of IRD-rich surficial sediments after ~1000 years BP in Little Storfjorden. These results differ from the earlier estimation in the previous study, suggesting that a terminal moraine complex (TMC) enclosing the Hambergbukta fjord basin indicates the maximum extent of a glacier advance during the Little Ice Age.

In the second study, the glacial history and depositional environments in the Arliss Plateau (AP) and the adjacent Chukchi Basin (CB) in the western Arctic Ocean off the East Siberian margin during marine isotope stage (MIS) 4 were reconstructed through lithostratigraphy and lithofacies analysis along with multi-beam bathymetry and seismostratigraphy. Based on the lithostratigraphic correlation, ARA02B/16B-GC obtained from the AP lower slope records glacier-related depositional history during the last 100 ka. The sedimentary record shows different interglacial (interstadial) and glacial (stadial) patterns. Interglacial sediments are relatively thin and characterized by bioturbated sandy mud, indicating hemipelagic deposition. On the other hand, glacial to deglacial sediments during MIS 4/3 and MIS 2/1 reflect several modes of glaciogenic deposition by drifting icebergs, suspension settling from turbid meltwater plumes and/or detached underflows, and turbidity currents. Based on strong seismic reflectors with good lateral continuity, a downslope sub-bottom profile from AP to CB is divided into seismostratigraphic units (SSU) 1 and 2. Based on the core-seismic correlation, SSUs 1 and 2 are constrained to MIS 3-1 and MIS 5c-3, respectively. An acoustically transparent lens within SSU 2 correlates on the upper slope to debris lobes downslope from the AP top covered by megascale glacial lineations. The

geomorphic/sedimentary pattern indicates a glacial erosional impact on the AP and proglacial deposition of eroded sediments on the slope and in the basin. Combined with the lithostratigraphy and lithofacies, the last debris lobe horizon was deposited in glacial/deglacial environments during late MIS 4 to early MIS 3. The absence of similar glaciogenic debris lobes within SSU 1 indicates no direct glacial impact on the AP during the Last Glacial Maximum (LGM). These results suggest that the last glacial erosion of the AP occurred during or immediately after MIS 4, possibly related to major glaciation in northern Siberia at ~50-70 ka.

As an extension of the second study, the third study reconstructed the longer-term glacial history in the East Siberian and Chukchi margins over the last 300 ka. This study presents the seismostratigraphy from the Chukchi Rise to Kuchеров Terrace and a ~14 m-long high-resolution sediment record (ARA06C/04JPC, hereafter 04JPC) from the Chukchi Basin. In addition, to assess the East Siberian marine ice sheet (ESIS) that extended to the western Chukchi Rise during MIS 4 to early MIS3, two short gravity cores (ARA09C/ST13, ST08) from the western Chukchi Rise were additionally analyzed. Four seismostratigraphic units (SSUs 1-4) were defined based on laterally continuous strong reflectors. SSUs were characterized by glaciogenic debris lobes stacked in the basin-ward slopes. In core 04JPC, sixteen brown layers (B1-16) representing interglacial/interstadial periods were defined, composed of bioturbated sandy mud to mud (Bsm/Bm). Among the brown layers, greyish glacial sediment layers (G1-16) present differences in thickness and lithofacies. With high sedimentation, G1-5 and G7 are mainly composed of crudely laminated mud (CLm), couplets of thinly laminated mud (TLm) and homogeneous mud (Hm). Notably, the thickest G16 (~600 cm) presented a ~25 cm-thick thinly interlaminated sand layer

(TLs), couplets of TLs and Hm, CLm, and debris flow deposits (Dm). These lithofacies suggest glacier-derived conditions including meltwater discharges, glacial turbidity currents, and debris flows. Applying the age model of core 04JPC, the distribution of glacial lithofacies indicates that the ice-grounding events can be constrained to MISs 2, 4/3, 5d or 5b, 6, and 8. Combined with emplacements of glacial debris flows, the deposition of G2, G7, and G16 indicates that occurrences of the huge ESIS may have entirely covered the East Siberian and Chukchi margins during MISs 4/3, 6, and 8. Furthermore, for core 04JPC, multiple lithostratigraphic parameters including elemental composition, lithofacies, and mineralogy indicate that the Chukchi Basin has experienced complex glaciations by the ESIS and the ice shelf extending from the LIS. The volume of the huge ESIS is approximately a quarter of that ($\sim 4.67 \times 10^6 \text{ km}^3$) of the Arctic ice shelf during MIS 6, affecting the eustatic sea level by $\sim 0.08 \text{ m}$. These findings provide valuable information to better understand global climate and sea-level changes during the Late Quaternary.

This thesis presented that integrating multi-beam bathymetry, high-resolution seismostratigraphy, and sediment records allow a better understanding of the Late Quaternary glacial impacts associated with the continental ice sheets around the Arctic and/or marine-based glaciers. To reconstruct the past glacial history more precisely, it is necessary to establish an accurate chronology for the recovered sediment records. For the older chronology beyond the ranges of ^{14}C dating, the Arctic chronological lithostratigraphy has uncertainties yet. In this work, however, reliable chronology during MIS 8 can be constrained based on high-resolution lithostratigraphy from the Chukchi Basin using several lithostratigraphic parameters that correlate well with previously developed stratigraphic records. Regardless of the chronology, this thesis

provided geological evidence for the occurrences of huge ESIS, possibly affecting sea level during the last 300 ka.

CHAPTER 1

Introduction

1.1. Backgrounds

1.1.1. Arctic Ocean

Recent global warming has been identified as the significant increase in the Arctic temperature over the last two decades (Serreze and Barry, 2011). This polar amplification results from changes in the surface albedo, ocean-atmosphere heat exchange, and greenhouse gas release in response to ice sheet retreat, sea ice reduction, and permafrost thawing (Miller et al., 2010; Stroeve and Notz, 2018; Meredith et al., 2019), indicating that climate changes depend on strong positive feedback within the Arctic system. Therefore, the study of climate-sensitive Arctic nature is needed to understand global climate changes.

In the northern hemisphere, the first ice growth occurred between 3.15 and 2.5 Ma (Tiedemann et al., 1994), which characterized dramatical changes in the behavior of glacial cycles from a low amplitude of 41 ka to a high amplitude of 100 ka through the Middle Pleistocene Transition (MPT) from 1250-700 ka (Fig. 1.1). During the Middle to Late Pleistocene, the amplified environmental changes were also evident in the Arctic Ocean sediments and Circum-Arctic continents (Phillips and Grantz, 2001; Spielhagen et al., 2004; Polyak et al., 2004, 2009; Melles et al., 2012). The growth of the Arctic ice sheets caused additional cooling by regionally increasing albedo and the average surface elevation (Miller et al., 2010). With abrupt global warming, the catastrophic melting of the continental ice sheets extended around the Arctic discharged huge amounts of fresh meltwater, triggering

the weakening of the formation of the North Atlantic deep water, consequently leading to an abrupt climate cooling (Broecker et al., 1989; Not and Hillaire-Marcel, 2012). The presence of the ice sheets in the high-latitude Arctic has played an important role in regulating the Earth's climate in the past, representing the importance of reconstructing the Quaternary glacial history in the Arctic Ocean to better understand the global climate changes.

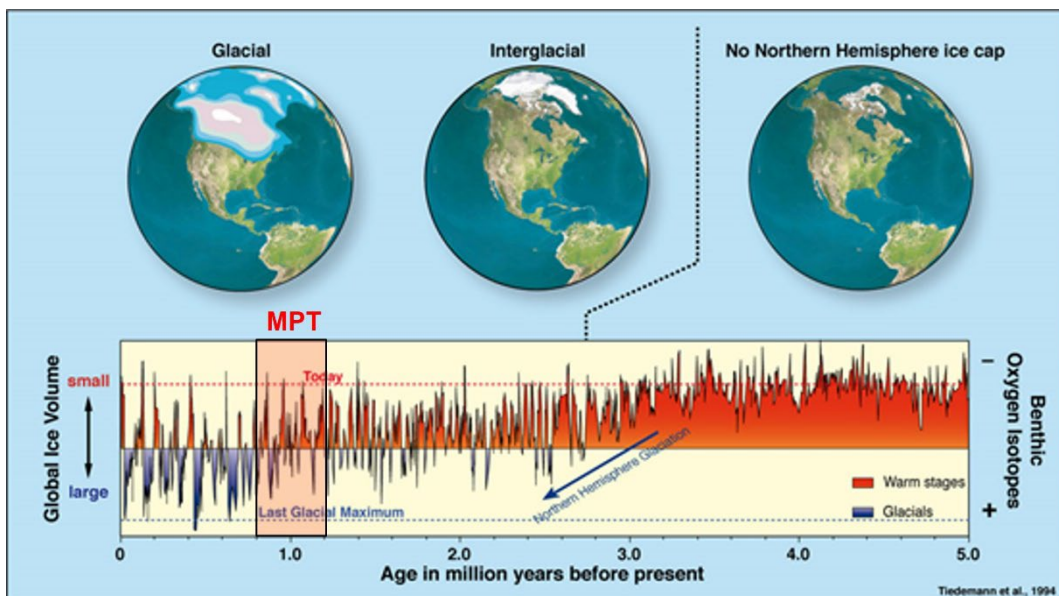


Fig. 1.1. Variations in the generalized benthic oxygen isotope reflecting the global climate evolution of the last 5 Ma (Tiedemann et al., 1994). This figure was taken from Stein (2008) and slightly modified. MPT indicates the Middle Pleistocene Transition.

1.1.2. Late Quaternary Arctic glaciations

The penultimate Quaternary Arctic ice sheets have been relatively well-investigated in the Circum Arctic continents (e.g., Svendsen et al., 2004; Batchelor et al., 2019 and references therein). Generally, it is well known that the Arctic continents were occupied by huge ice sheets including the Eurasian Ice Sheet (EIS), Greenland Ice Sheet (GIS), Laurentide Ice Sheet (LIS), and Cordilleran Ice Sheet (CIS) during the glacial maxima (Fig. 1.2) (e.g., Svendsen et al., 2004; Ehlers and Gibbard, 2007; Jakobsson et al., 2014; O'Regan et al., 2017; Batchelor et al., 2019). It was recently suggested that the East Siberian marine ice sheet (ESIS) had also repeatedly existed during the Late Quaternary glacial-interglacial cycles (Niessen et al., 2013).

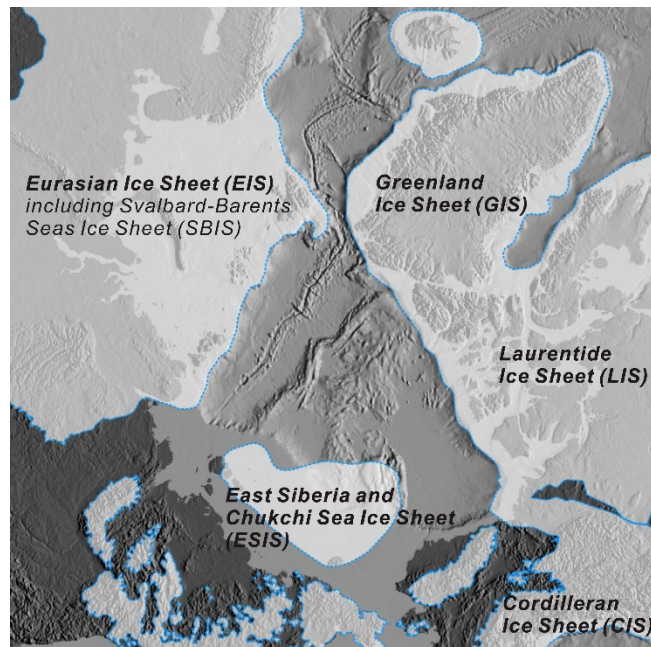


Fig. 1.2. Late Quaternary maximum configuration of the Arctic ice sheets (from Batchelor et al., 2019).

Compared with the Arctic continents, ice conditions in the Arctic Ocean interior during the glacial maxima were highly speculative due to the lack of direct observational data until the late 1900s. In 1966, Donn and Ewing suggested the sea ice-free environment for the Arctic Ocean interior because the open marine condition can only allow moisture supply for building the large Arctic ice sheets. On the other hand, Mercer (1970) hypothesized thick ice shelf conditions based on physiographic analogies between the Arctic Ocean and Western Antarctica. The thick ice shelf was further argued to be a critical stabilizing element for marine ice sheets grounded on continental shelves and flowing into the Arctic Ocean (Grosswald and Hughes, 1999). Over the last two decades, lots of geophysical surveys have been conducted on the Yermak Plateau off northern Svalbard (Vogt et al., 1994), Lomonosov Ridge (Jakobsson et al., 2008), Chukchi Borderland (Polyak et al., 2001; Dove et al., 2014), and East Siberian margin (Niessen et al., 2013; O'Regan et al., 2017). Accumulating morphological evidence in the Arctic Ocean and marginal seas has confirmed ice groundings on the seafloor down to approximately 1 km below the present sea level, raising the Arctic Ocean, which has re-raised the km-thick Arctic ice shelf condition similar to that of the “maximum ice” scenario (Fig. 1.3A) as hypothesized by Hughes et al. (1977) (Jakobsson et al., 2016) (Fig. 1.3B).

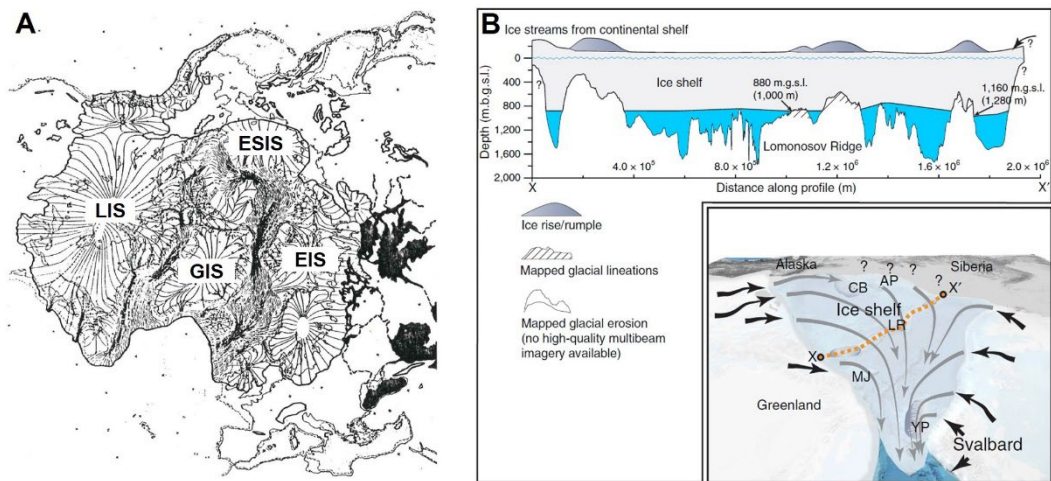


Fig. 1.3. (A) A maximum reconstruction of the late-Würm Arctic Ice Sheet by Hughes et al. (1977). (B) The km-thick Arctic ice shelf condition during MIS 6 proposed by Jakobsson et al. (2016).

Based on the occurrences of *Emiliania huxleyi* used to define the MIS 5 interval in sediment records on top of the ice-scoured surfaces on the Lomonosov Ridge and the adjacent area of the Arliss Plateau in the East Siberian margin, Jakobsson et al. (2016) proposed that a km-thick ice shelf of $4.67 \times 10^6 \text{ km}^3$ volume covering the entire Arctic Ocean occurred during the MIS 6 or older (Fig. 1.3B), which affects the eustatic sea level by $\sim 0.34 \text{ m}$. However, the occurrences of *E. huxleyi* are not unique for one specific time interval (Schreck et al., 2018). In addition, Jakobsson et al. (2016) reported the *E. huxleyi* zone in the sedimentary record near the Arliss Plateau, which was recently constrained to MIS 3 (Wiers et al., 2020). In this context, the glacial erosion in the adjacent area of the Arliss Plateau could be younger than MIS 6.

Repeated occurrences of a km-thick marine ice sheet (ESIS) were corroborated by several sets of streamlined glacial lineations in the East Siberian

margin (Niessen et al., 2013). The timings for ESIS occurrences were roughly postulated as the Pleistocene glaciations before the Last Glacial Maximum (LGM) (Niessen et al., 2013). Given the limited dataset in these regions (Fig 1.4) (Batchelor et al., 2019 and references therein), a precise and accurate reconstruction of the ESIS history is required based on reliable age constraints and geological evidence. Notably, the occurrence of ESIS may explain the discrepancy between the ice volume inferred from the global $\delta^{18}\text{O}$ variations in benthic foraminifera and geological sea-level records (Broecker, 1975; Williams et al., 1981; Pico et al., 2017).

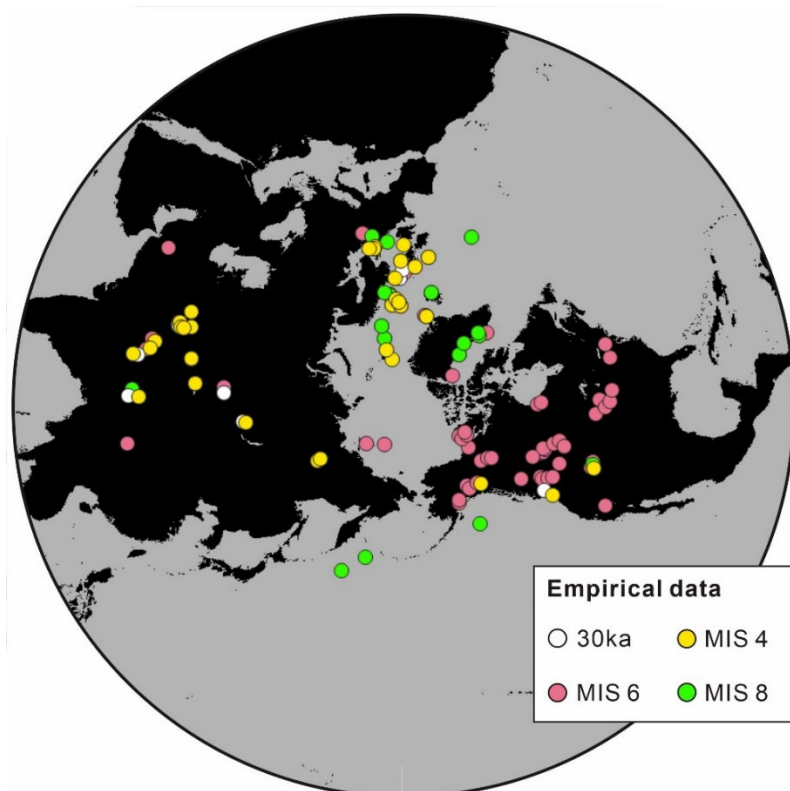


Fig. 1.4. Sources of the empirical data to reconstruct the Arctic ice sheet configurations for six time-slices from Batchelor et al. (2019).

1.2. Reconstruction of the Arctic glaciations

Previous proxy-based reconstructions of paleo-sea-ice conditions, oceanographic changes (influenced by the glacier melting), and sediment provenance have provided a better understanding of the Arctic glacial impacts during the Late Quaternary (Poore et al., 1999; Spielhagen et al., 2005; Belt et al., 2007; Knies et al., 2007; Jang et al., 2013; Xiao et al., 2015a, b; Dong et al., 2017, 2020). However, they do not provide direct evidence for the Arctic ice sheets and/or marine-based glaciers. On the other hand, detailed bathymetric mapping and high-resolution sub-bottom profiling provide direct evidence for the occurrences of the ice sheets and/or marine-based glaciers. Combined with the morphological evidence, attendant glacial sediment records allow precise reconstructions of the glacial history related to the growth and decay of the Arctic (marine) ice sheets.

1.2.1. Identification of glacialic submarine landforms

Evidence of the past ice sheets can be preserved in sea-floor morphology. At the grounding zone of marine-terminating glaciers or ice sheets, ice-proximal submarine landforms including grounding zone wedges and/or terminal moraines, ice-proximal fans, and recessional moraines have formed (Fig. 1.5) (Lønne, 2001; Powell and Alley, 1997; Batchelor and Dowdeswell, 2015). The fast-flowing ice over a sedimentary substrate often produces streamlined bedforms parallel to the ice flow in variable scales (Clark et al., 1994). The upper surface of subglacial till

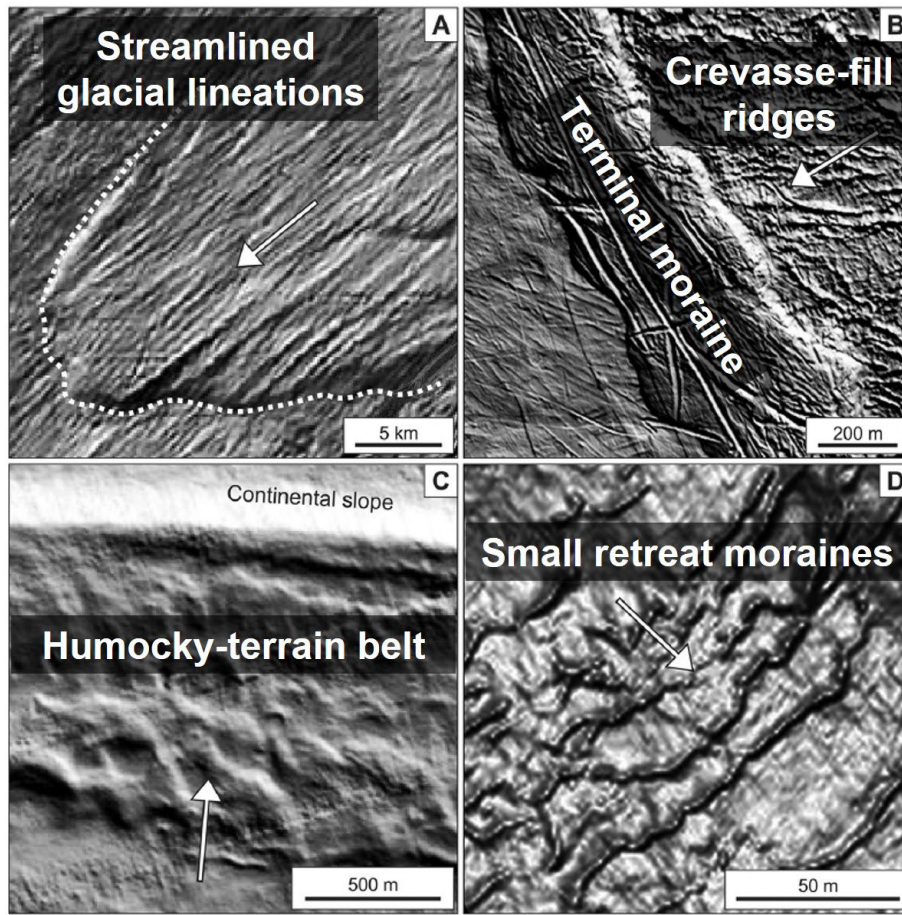


Fig. 1.5. Glacigenic submarine landforms formed by the advance and retreat of the marine-based glaciers. This figure was taken from Batchelor and Dowdeswell (2015).

deposits can be streamlined into glacial lineations by the fast-flowing ice streams (Ottesen and Dowdeswell, 2006; Batchelor and Dowdeswell, 2015). Therefore, identifying these glacigenic submarine landforms allows for determining the main direction, extent, and thickness of the former ice sheets and marine-based glaciers.

Furthermore, the high-resolution sub-bottom profiling on the glacigenic submarine landforms provides seismic records of glacial to interglacial deposits during the Late Quaternary. Identified in the seismic profiles, internal reflection

patterns can define stratigraphic relations between glacial subaqueous landforms and glaciomarine (or open-marine) sediments (e.g., Polyak et al., 2007; Jakobsson et al., 2010; Niessen et al., 2013; Kim et al., 2021).

1.2.2. Glacier-induced depositional processes

The advance and retreat of ice sheets or marine-based glaciers cause various glacier-induced depositional processes (Fig. 1.6), resulting in variability in sediment texture, structure, origins (color and mineralogy), and sedimentation rates. During the glacial periods, the seafloor of the glaciated shallow continental margins can be eroded and/or deformed by the advancing grounding ice. As the grounding ice advances, the glacial bulldozing causes to supply of numerous sediments towards the Arctic deep sea. As a result, the sediments eroded from the glaciated continental margin to the continental slope could be reworked as debris flows and turbidity currents (Powell, 1990; Kleiber et al., 2000; ÓCofaigh et al., 2003; Batchelor and Dowdeswell, 2015). As the glacier retreats, turbid meltwater plumes are discharged repeatedly at the termini of the marine-terminating glaciers. Repeated changes in the physical conditions close to the glacier front have been identified as laminated or stratified sequences in the sediment records (Hesse et al., 1996; Kleiber et al., 2000; ÓCofaigh et al., 2003; Forwick and Vorren, 2009; Lucchi et al., 2013). Due to the influx of a large volume of glacial sediments during this period, instability of continental slope possibly causes glacial debris flows. In addition, icebergs calved from glacier fronts drift along the Arctic Ocean surface

currents, releasing coarse debris (ice-rafted debris, IRD) to the Arctic seafloor. On the other hand, under thick and permanent sea-ice conditions, the sedimentation rates significantly decrease, possibly causing sediment hiatus (Polyak et al., 2007; Chui et al., 2017). Hence, glacier-induced depositional patterns provide a better understanding of changes in glacial environments.

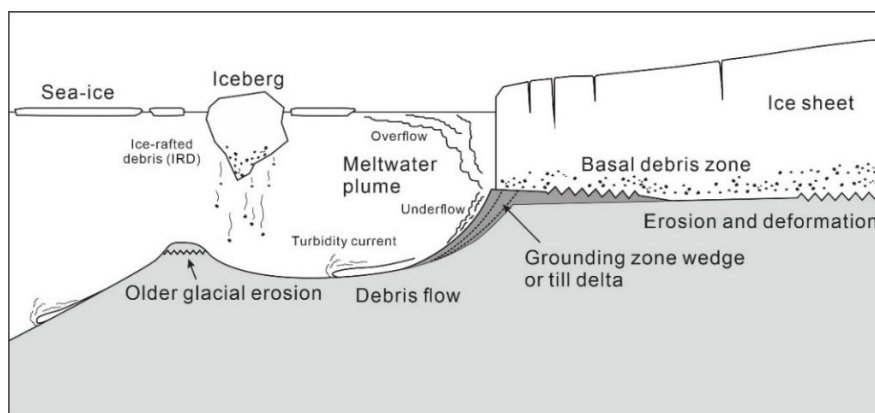


Fig. 1.6. Schematic model of glacier-induced depositional processes (referred to Laberg and Vorren, 1995; Hesse et al., 1996).

1.2.3. Age framework

A reliable chronological framework must first be established to reconstruct the Arctic glacial history. Using biogenic carbonates (calcareous tests), AMS ^{14}C age dating provides the absolute ages of the uppermost Quaternary chronology. For older chronology, lithostratigraphy is generally used for the typical age framework of the Arctic Ocean sediments at present (e.g., Xiao et al., 2020; Wang et al., 2021; Zhao et al., 2022). Combined with the ^{14}C -calibrated amino acid racemization (AAR) data of planktic foraminifera and the optically stimulated luminescence

(OSL) study, distinct variations in lithological and geochemical composition, stable isotope, foraminifera, and attendant sediment properties have developed the Arctic lithostratigraphy (Jakobsson et al., 2003; Kaufman et al., 2008; Adler et al., 2009; Polyak et al., 2009; O'Regan et al., 2019). The prominent contrast in sediment color, texture, and geochemical composition corresponds to glacial-interglacial variability (Jakobsson et al., 2000; Polyak et al., 2004, 2009; Stein et al., 2010). The Late Quaternary Arctic sediments are characterized by alternating dark brownish sandy mud and olive/greyish, finer-grained sediment units (Phillips and Grantz, 1997; Polyak et al., 2004, 2009; Adler et al., 2009; Stein et al., 2010; Schreck et al., 2018). The brown color is generally governed by manganese (Mn) content. High Mn content in brownish units has mainly resulted from increased Mn supply from the Siberian continental margin during interglacial/interstadial periods (Jakobsson et al., 2000; Polyak et al., 2004, 2009; März et al., 2013; Löwemark et al., 2014; Ye et al., 2019).

However, typically low sedimentation rates and bioturbation in the Arctic Ocean hamper a consistent lithostratigraphic correlation due to a merging of interglacial sediment layers accompanied by a glacial hiatus (Chiu et al., 2017). Furthermore, the complex overprint of glacial impacts and the poor preservation of biogenic components complicates defining the coherent Arctic lithostratigraphy (Backman et al., 2004; Darby et al., 2006; Stein, 2008; Polyak et al., 2009; Polyak and Jakobsson, 2011). To resolve the lithostratigraphic uncertainty, it is necessary to define the Arctic lithostratigraphy thoroughly using multiple lithostratigraphic

parameters such as down-core variations in elemental composition, foraminiferal abundance, and paleomagnetic inclinations (Xiao et al., 2020; Wang et al., 2021; Zhao et al., 2022).

1.3. Objectives

This thesis used multi-beam bathymetry, high-resolution sub-bottom profiles, and sediment core records to reconstruct accurately the glacial history and glacier-induced depositional environments associated with glacial-interglacial cycles over the last 300 ka. Glacigenic submarine landforms and seismostratigraphy provide dynamics and dimensions of ice sheets and/or marine-based glaciers. Summarized in Table 1.1, multiple core measurements were conducted to constrain lithostratigraphic chronology and to define lithofacies of the investigated sediment cores. Notably, using the sediment cores with reliable age constraints, core-seismic correlation enables accurately determining the timing when glacigenic submarine landforms were formed. These results allowed precise reconstructions of glacier-induced depositional environments in the Svalbard fjords and the western Arctic Ocean.

The study in chapter 2 mainly focused on the reconstruction of glacier behavior and its dynamics in Arctic Svalbard fjords since the Younger Dryas. This study presents a reconstruction of glacial history and depositional environments in Hambergbukta and Little Storfjorden, southern Svalbard using multi-beam

bathymetry, high-resolution sub-bottom profiles, and sediment gravity cores obtained during the 3rd Korea-Norway joint Svalbard cruise with RV *Helmer Hanssen* in 2019 (Table 1.2).

For the longer-term glacial history and glacier-induced depositional environments during the Late Quaternary, multi-beam bathymetry, high-resolution sub-bottom profiles, sediment gravity cores, and a long piston core have been acquired from the Chukchi Basin and the surrounding East Siberian and Chukchi margins in the western Arctic Ocean. In the western Arctic Ocean, all of the studied materials were acquired during several RV *Araon* Arctic Expeditions in 2012-2019 (Table 1.2). In chapter 3, the last glacial erosion on the Arliss Plateau and attendant depositional environment in the adjacent Chukchi Basin off the East Siberian margin in the western Arctic Ocean were reconstructed using multiple data sets. These results provided geological evidence for the occurrence of huge ESIS causing the last glacial erosion of the Arliss Plateau during or immediately after MIS 4.

Chapter 4 deals with the longer-term glacial impacts of ESIS over the last 300 ka as an extension of the previous study in Chapter 3. This chapter suggests different ice-grounding events on the East Siberian and Chukchi margins during MISs 2, 4/3, 5d or 5b, 6, and 8. Notably, the time intervals of MISs 4/3, 6, and 8 characterized the huge ESIS that fully covered the East Siberian and Chukchi margins. These results provide new insight into the Late Quaternary ice conditions of the Arctic Ocean.

Table 1.1. List of multiple core measurements conducted in this thesis.

Measurement	Objective	Organization
Multi-sensor-core-logging (MSCL)	Density, P-wave velocity, magnetic susceptibility	AWI, UiT
X-ray fluorescence (XRF) core-scanning	Elemental geochemistry, split-core surface image, color index	KIGAM, KOPRI, UiT
X-ray diffraction analysis (XRD)	Mineralogy	Bremen Univ.
X-radiography	Sedimentary internal structure	KOPRI, UiT
Grain-size analysis	Sedimentary texture	KIGAM, KOPRI
Paleomagnetic measurement	Variations of magnetic inclination	Bremen Univ.
Organic chemistry measurement	TOC, $\delta^{13}\text{C}$, TOC/N _{org}	KOPRI
AMS ^{14}C age dating	Absolute age	AWI, Beta

Table 1.2. List of geophysical surveys and sediment coring conducted in study areas.

Study area	Data type	Expedition	Year
East Siberian margin	MBES	ARA03B	2012
	SBP	ARA02B, 06C	2011, 2015
	Coring	ARA02B	2011
Chukchi margin	MBES	ARA07C, 09C, 10C	2016, 2018, 2019
	SBP	ARA09C	2018
	Coring	ARA09C	2018
Chukchi Basin	SBP	ARA06C, 09C	2015, 2018
	Coring	ARA06C	2015
Svalbard (Hambergbukta fjord)	MBES SBP Coring	HH19	2019

CHAPTER 2

Glacial history and depositional environments in the Little Storfjorden and Hambergbukta since the Younger Dryas

This chapter was prepared for submission to Frontiers in Earth Science

2.1. Introduction

During the last glacial maximum (LGM), the Svalbard-Barents Ice Sheet (SBIS) reached its maximum extent, covering the Svalbard archipelago and the Barents Sea shelf (Svendsen et al., 2004; Dowdeswell et al., 2010; Hughes et al., 2016; Wiberg et al., 2022). After the LGM, atmospheric warming and the increased inflow of warm Atlantic Water associated with sea-level rise triggered the collapse and rapid retreat of the marine-based SBIS (Hughes et al., 2016). As a result, glaciers extending beyond the Svalbard archipelago rapidly retreated into the fjords (Svendsen et al., 1996; Landvik et al., 2005; Jessen et al., 2010; Hughes et al., 2016; Rasmussen and Thomsen, 2021). The retreat was interrupted by several cooling episodes, and regional differences in glacial response between the fjords were observed (Svendsen et al., 1996; Forwick and Vorren, 2009; Bartels et al., 2017; Rasmussen and Thomsen, 2015; Nielsen and Rasmussen, 2018; Allaart et al., 2020; Jang et al., 2021; Rasmussen and Thomsen, 2021). Notably, in southern Svalbard, this included a re-advance(s) of an outlet glacier into Storfjorden and the Storfjorden Trough (Nielsen and Rasmussen, 2018; Rasmussen and Thomsen, 2021).

At the grounding zone of marine-terminating ice sheets or glaciers, ice-proximal submarine landforms, such as grounding zone wedges, ice-proximal fans, and recessional moraines, are deposited during still-stands or re-advances of the ice margin (Lønne, 2001; Powell and Alley, 1997; Batchelor and Dowdeswell, 2015). Hence, identifying these glacialic submarine landforms and their formation provides essential information about the behavior of past marine-based glaciers. Multiple investigations have focused on understanding the glacial dynamics and history during

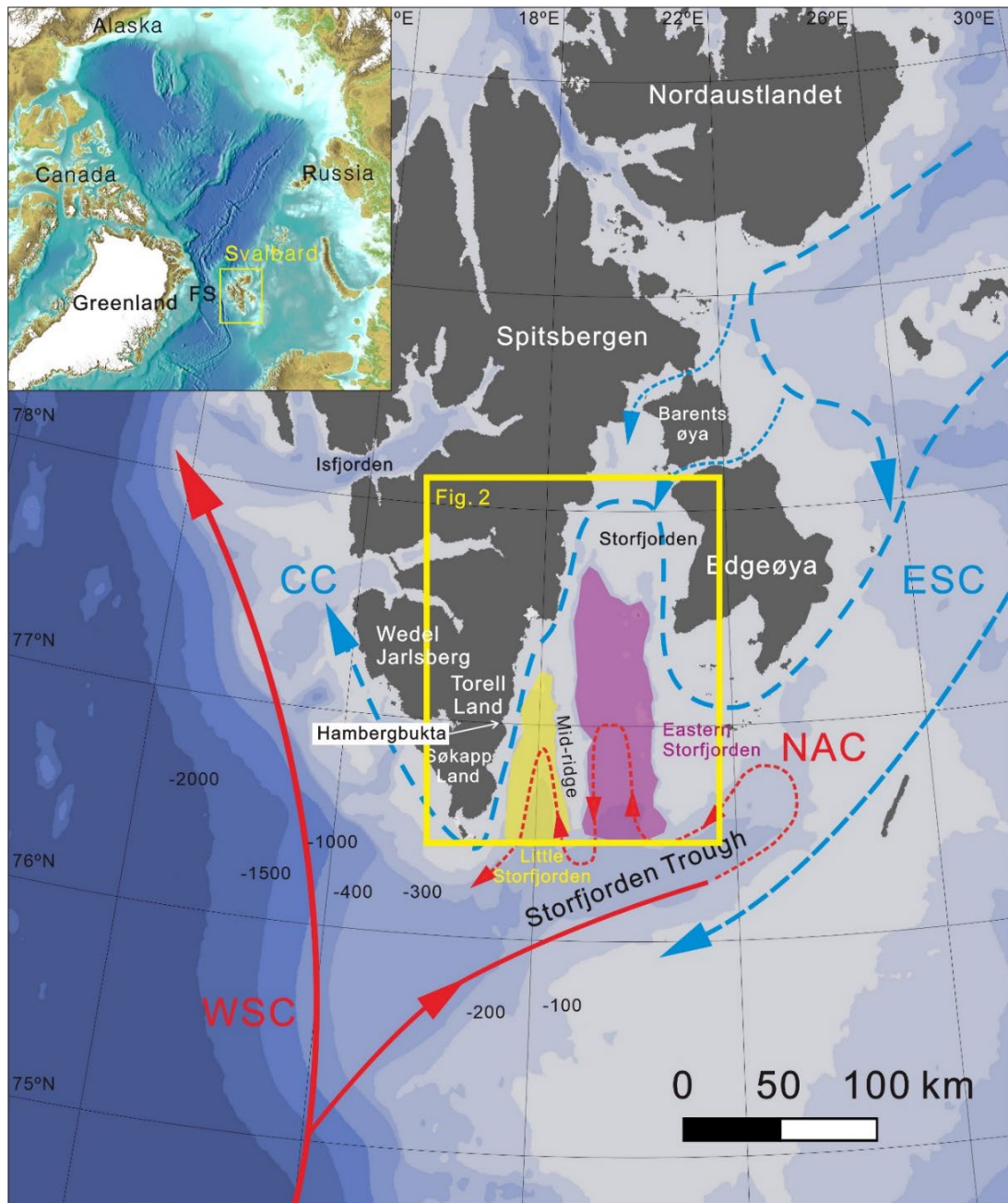


Fig. 2.1. Physiographic map of Arctic Ocean and Svalbard located in the east of Fram Strait (FS). The ocean circulation patterns of the East Spitsbergen Current (ESC)/Coastal Current (CC) and West Spitsbergen Current (WSC)/ Norwegian Atlantic Current (NAC) were based on Skogseth et al. (2005).

the last deglaciation in the eastern part of Storfjorden (Jessen et al., 2010; Lucci et al., 2013; Łacka et al., 2015; Nielsen and Thomsen, 2018; Rasmussen and Thomsen, 2021). Storfjorden is divided by the N-S trending central ridge (Mid-ridge) into western, i.e., Little Storfjorden, and eastern parts, as well as the Storfjorden trough offshore southern

Svalbard (Fig. 2.1). In eastern Storfjorden, the three NE-SW oriented grounding zone wedges (G1-G3) indicate that the ice front had larger re-advances and/or relatively long-lasting still-stands between 15.3 and 11.7 ka (Nielsen and Rasmussen, 2018). By integrating geophysical survey data and sediment core records with a robust chronological framework (Rasmussen and Thomsen, 2014; Nielsen and Rasmussen, 2018), it was suggested that the ice stream/marine-based glacier in eastern Storfjorden advanced southwards at least 20 km during Younger Dryas (YD, 13-12 ka) and retreated rapidly during the YD-Holocene transition (12-11.7 ka) (Fig. 2.2A). Furthermore, Nielsen and Rasmussen (2018) suggested that the retreating ice in Little Storfjorden would experience short, temporary halts compared to the eastern Storfjorden based on the glacier retreat dragging laterally by the Mid-Ridge and the inflow of subsurface Atlantic water to the east. However, the accurate timing, configuration, behavior, and the dynamics of the past glacier in, Little Storfjorden remain poorly known.

Little Storfjorden consists of several tributary fjords and bays. One of these is Hambergbukta, located between Torell Land and Sørkapp Land (Fig. 2.1). Hambergbukta has undergone repeated surges of a tidewater glacier (Hambergbreen) since the Little Ice Age (LIA) (Lefauconnier and Hagen, 1991; Pälli et al., 2003). Recently, Noormets et al. (2021) presented a bathymetric map and shallow gravity cores on the Hambergbukta fjord basin and reconstructed a glacial history of Hambergbreen since 1900. However, the long-term glacial history leading to the formation of glacial submarine landforms around the fjord mouth remains poorly known. In this study, we present new swath-bathymetry data, high-resolution seismic profiles, and three sediment core records from the Little Storfjorden and

Hambergbukta, respectively, to reconstruct a more detailed glacial history in the area since the YD. Furthermore, we provide improved age constraints for the glacial submarine landforms to better understand the past behavior of Hambergbreen before and during the Holocene, and the LIA surge event.

2.2. Physiography

Storfjorden is an overall N-S-oriented, funnel-shaped fjord system located offshore of the southeastern Svalbard archipelago (Fig. 2.1). At the fjord mouth, Storfjorden is connected to the NE-SW-oriented Storfjorden Trough that extends to the shelf break off southwestern Svalbard. The fjord is approximately 130 km long, divided by the N-S-oriented ridge called “Mid-ridge” (Nielsen and Rasmussen, 2018) into a broader and longer eastern Storfjorden, as well as a narrower and shorter Little Storfjorden in the west. The crest of Mid-ridge is deeper than ~65 m water depth.

Storfjorden is characterized by high variability in hydrographic conditions and surface ocean currents present a wind-driven circulation pattern (Skogseth et al., 2007). Cold and relatively fresh Arctic Water enters Storfjorden as the East Storfjorden is characterized by high variability in hydrographic conditions and surface ocean currents present a wind-driven circulation pattern (Skogseth et al., 2007). Cold and relatively fresh Arctic Water enters Storfjorden as the East Spitsbergen Current, continuing as a coastal current along the inner shelf offshore west Spitsbergen (Skogseth et al., 2005, 2007) (Fig. 2.1). Warm and relatively saline surface water (Atlantic Water), a branch of the Norwegian Atlantic Current/West Spitsbergen Current, enters the southern Storfjorden Trough (Schauer, 1995). This Atlantic Water branch presently flows

anticlockwise through eastern Storfjorden into Little Storfjorden, eventually flowing out the mouth of Storfjorden Trough (Fig. 2.1) (Skogseth et al., 2005). Storfjorden is generally covered by sea ice during winter and spring. During sea-ice freezing, resulting from strong north-easterly winds, the salinity of the surface water became denser and saltier, consequently leading to brine rejection to the seafloor. The sinking of dense, brine-enriched surface water entrains ambient water and fills the Storfjorden basin (Rasmussen and Thomssen, 2014). As the newly produced sea ice drifted away, a coastal polynya in the northern fjord persists until late winter (Anderson et al., 2004).

The seafloor of Little Storfjorden deepens southward from 40 m to 200 m (Fig. 2.2A). In the middle part of Little Storfjorden, two NE-SW-oriented ridges (R1, R2) are observed (Fig. 2.2). The height of the northern R1 ridge ranges from 7 to 14 m. R2

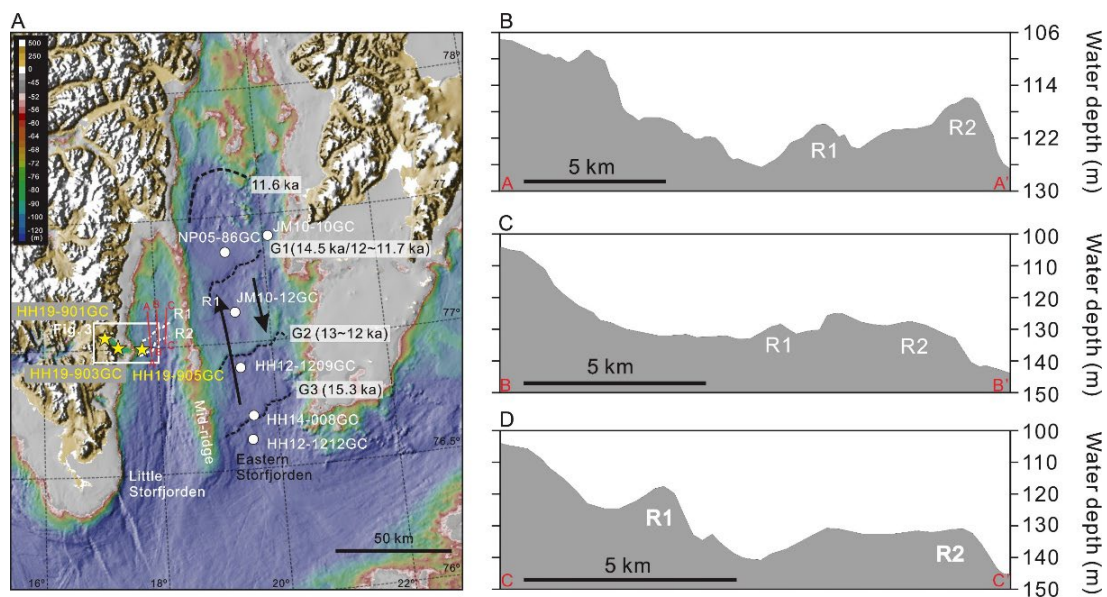


Fig. 2.2. (A) Zoom-in on Little Storfjorden and Hambergbukta. Three red lines indicate bathymetric cross-sections (A-A', B-B', and C-C') extracted from the Arctic Ocean bathymetric map (IBCAO v.4). Three yellow stars indicate the locations of the studied cores. White circles indicate reference cores from Nielsen and Rasmussen (2018). In panels (B), (C), and (D), three cross-sections show NE-SW-oriented ridges (R1 and R2). In the cross-section at the western (B), R2 shows an asymmetric morphology with a gentle stoss side and a steep lee side. Towards the east, the ridge becomes rounded and flat (D).

is located 3 km south of R1. This ridge is 15 m high and subparallel to R1. In particular, the western part of R2 shows an asymmetric geometry with a gentle inner (stoss) side and a relatively steep outer (lee) side (Fig. 2.2B). Towards the eastern part of R2, the crest is flatter (Fig. 2.2D).

Hambergbukta is a curved and W-E-oriented tributary fjord to Little Storfjorden (Fig. 2.2A). It is ~17 km long and narrows from ~8 km width at the fjord mouth to ~1.1 km at the head. In Hambergbukta, the fjord basin is shallower than 100 m water depth, which is bordered by a ~50 m-high large terminal moraine at the fjord mouth (Fig. 2.3A). The moraine was termed as the terminal moraine complex (TMC) in Noormets et al. (2021). Coinciding with the ice front in 1970, a ~15 m-high small terminal moraine (T1) divides the fjord basin into an inner and outer part, respectively. In both sub-basins, variable glacial sub-marine landforms are identified, indicating repeated glacier surges and retreats based on the occurrences of crevasse fill ridges on the proximal sides of end moraines (Noormets et al., 2021). In the innermost part of Hambergbukta, the current termini of Hambergbreen and Sykorabreen occur in a combined ice front. Small glaciers, including Kambreen, Bevanbreen, Coryellbreen, and Kanebreen, presently terminate on land along the southern coast (Fig. 2.3A). The mountains surrounding Hambergbukta are up to 500 m high. They are composed of Cretaceous shales, siltstones, and sandstones of the Helvetiafjellet and Carolinefjellet Formations from the Adventalen Group, overlain by Palaeocene shales, mudstones, and siltstones of the van Mijenfjorden Group (Fig. 2.3A) (Dallmann et al., 2002).

2.3. Materials and methods

2.3.1. Bathymetric mapping and seismic profiling

Bathymetric mapping and high-resolution (CHIRP) sub-bottom profiling (SBP) were conducted during the 3rd Korea-Norway joint cruise to Svalbard fjords with RV *Helmer Hanssen* in 2019 (HH19). Swath bathymetry data was acquired with a hull-mounted Kongsberg Maritime EM 302 multi-beam echo sounder (MBES). They were complemented by the regional bathymetry of the Arctic Ocean (IBCAO v.4; Jakobsson et al., 2020) (Fig. 2.3A). SBP profiles were acquired using a hull-mounted EdgeTech 3300-HM sub-bottom profiler with a 2-12 kHz frequency range during the cruise. In the SBP, the seafloor water depth was determined based on a p-wave velocity of 1500 m/s in the water column.

2.3.2. Core measurements

Three sediment gravity cores were retrieved from Hambergbukta (HH19-901-GC, HH19-903-GC) and Little Storfjorden (HH19-905-GC) using a 6 m-long gravity corer with a total weight of 1,900 kg (Table 2.1) (Fig. 2.2A). The inner diameter of the plastic liner was 10 cm.

The wet bulk density and magnetic susceptibility were measured at 1 cm steps on the whole core using a Geotek Multi-Sensor Core Logger at UiT The Arctic University of Norway in Tromsø. Line-scan images were acquired on split-half cores using the Avaatech X-ray fluorescence (XRF) core scanner with a Jai L-107CC 3CCD RGB line-scan camera. Sediment elemental composition was measured at 1 cm intervals with an Avaatech XRF core scanner using the following settings: 1) 10 kV,

1000 μA , 10s counting time, no filter, and 2) 30 kV, 1000 μA , 10s counting time, Pd-thick filter. In this study, we used Zr/Rb and Ca/Sr ratios to get more continuous values reflecting changes in grain size (Dypvik and Harris, 2001; Rothwell and Croudace, 2015; Zuchuat et al., 2020) and to determine detrital carbonate (Hodell et al., 2008), respectively. X-radiographs were acquired on split-half cores using a Geotek Standard X-ray CT System (XCT) at UiT.

The grain size was analyzed using about 130 mg of freeze-dried bulk sediments. Before the analysis, all samples were treated with 35% H_2O_2 for 24 h to decompose organic matter. After subsequent rinsing with deionized water, the sediment samples were treated with an ultrasonic vibrator to facilitate particle disaggregation before analysis. The measurements were conducted with a Malvern Mastersizer 3000 laser diffraction particle size analyzer at the Korea Polar Research Institute (KOPRI). The content of coarse particles ($>63 \mu\text{m}$) was additionally measured by wet sieving using 1-2 g of bulk sediments from the same sampling depths.

Measurements of the total organic carbon (TOC) content and carbon isotope of organic matter ($\delta^{13}\text{C}_{\text{org}}$) were performed on powdered samples treated with hydrochloric acid for 24 h to remove inorganic carbonate. The analytical precision for the organic carbon data is within 0.2‰. Organic nitrogen (N_{org}) was measured on powdered bulk sediments treated with a KOBBr-KOH solution to separate inorganic and organic nitrogen fractions (Silva and Bremner, 1966). The content of N_{org} was calculated by subtracting inorganic nitrogen (N_{inorg}) from total nitrogen determined using bulk sediments. TOC, $\delta^{13}\text{C}_{\text{org}}$, and N_{inorg} were measured with a Thermo Delta V Isotope Ratio Mass Spectrometer connected to a Thermo Flash 2000 CHNS/OH Elemental Analyzer at KOPRI. The measurement process was conducted based on Joo

et al. (2019).

For ^{14}C dating, we collected both intact and fragmented marine mollusk shells (Table 2.2). The AMS ^{14}C analyses were performed at the Beta Analytic Laboratory in Miami, Florida, the USA, and the MICADAS laboratory, Marine Geochemistry, Alfred Wegener Institute, Helmholtz Centre for Polar and Marine Research, Bremerhaven, Germany, respectively. To calibrate all ^{14}C dates, we used the Calib 8.1.0 program (Stuiver and Reimer, 1993) and the Marine 20 dataset (Heaton et al., 2020). Age data were converted to calendar years, applying a regional ΔR of -61 ± 37 after Pieńkowski et al. (2021). Median values of the calibrated ages ($\pm 2\sigma$) were used to determine the age-depth model of the HH19 cores (Table 2.2). The age-depth modeling was constrained by Bayesian age-depth modeling in BACON (v. 2.2.; Blaauw and Christen, 2011). We applied the same parameter settings in Jang et al. (2021) for the BACON modeling.

Table 2.1. Information on the cores investigated in this study.

Core	Latitude (N)	Longitude (E)	Water depth	Recovery
HH19-901-GC	77°03.151'	17°03.954'	77 m	90 cm
HH19-903-GC	77°00.979'	17°15.813'	97 m	179 cm
HH19-905-GC	76°59.131'	17°44.873'	112 m	241 cm

Table 2.2. AMS ¹⁴C dates and calibrated dates for the studied cores.

Lab ID	Core (HH19)	Depth (cm)	AMS ¹⁴ C age (yr)	Cal. age (yr)	Sample status (Mollusk)
Beta-546275	901	4-5	8800 ± 30	9520-9370	Fragmented
Beta-546276	901	49-50	8410 ± 30	8988-8714	Fragmented
Beta-546277	901	94-95	101.63 ± 0.38 pMC	post-1950	Fragmented
Beta-546279	903	69-70	105.37 ± 0.39 pMC	post-1950	Fragmented
AWI 5414.1.2	903	99-100	8322 ± 95	8995-8480	Fragmented
Beta-546280	903	164-165	8540 ± 30	9185-8951	Fragmented
AWI 5415.1.2	903	174-175	8989 ± 101	9869-9328	Fragmented
AWI 5416.1.3	905	19-20	1181 ± 65	759-521	Fragmented
AWI 5417.1.3	905	134-135	3797 ± 77	3808-3438	Intact (paired shells)
AWI 5418.1.2	905	159-160	9472 ± 105	10494-9890	Fragmented
Beta-546281	905	164-165	9350 ± 30	10175-9917	Fragmented
AWI 5419.1.2	905	216-217	10616 ± 120	12156-11234	Intact (paired shells)

2.4. Results

2.4.1. Glacigenic submarine landforms

1) Geomorphology

A detailed description and interpretation of submarine landforms in Hambergbukta were conducted by Noormets et al. (2021) using MBES and high-resolution SBP data. Our study area covers a narrower region of Hambergbukta than the area investigated in Noormets et al. (2021). However, it extends across the terminal moraine complex and farther into Little Storfjorden (Fig. 2.3A). Here, we first summarize the submarine landforms in the Hambergbukta fjord basin, supplemented by a description of the morphological features of the terminal moraine complex (TMC). Furthermore, this study provides the new morphological data on the distal side (Little Storfjorden) of TMC (Fig. 2.3).

Submarine landforms in the Hambergbukta. A small terminal moraine (T1) or end moraine, in conformity with Noormets et al. (2021), corresponding to the maximum extent of a tidewater glacier during the last surge (1961-1970), is observed in the middle part of the fjord basin (Fig. 2.3A). T1 divides the fjord into an inner and an outer basin, respectively. Streamlined glacial lineations and drumlins, oriented parallel to former ice flow, are partly recognized in both sub-basins (Figs. 2.3B, C). Rhombohedral small ridges, interpreted as crevasse-fill or –squeeze ridges, following Noormets et al. (2021), are abundant in both sub-basins, overlying the glacial lineations and drumlins (Figs. 2.3B, D). Towards the landside, the rhombohedral ridges become more sub-parallel and more perpendicular to the fjord axis (Fig. 2.3B). They are interpreted as annual push moraines by Noormets et al. (2021). On the distal slope of T1, debris lobes are identified, which partly cover the former crevasse-fill ridges in the outer basin (Fig. 2.3C). Towards the fjord mouth, sinuous submarine ridges up to approximately 25 m in height are observed (Fig. 2.3A). The majority of the ridges are symmetrical in cross-section (Fig. 2.4). They are subparallel and exhibit more lateral compression towards the south. In the southern part, crevasse-fill ridges are also recognized among the subparallel sinuous ridges (see Fig. 7 in Noormets et al., 2021).

The terminal moraine complex. At the mouth of Hambergbukta, a large terminal moraine with a height of up to 50 m is located (Figs. 2.3A, 5). The northern part of the moraine partly shows a dual-crested morphology with a patch of crevasse-fill or -squeeze ridges (Fig. 2.3A) (Noormets et al., 2021). Considering this morphological complexity, Noormets et al. (2021) termed it a terminal moraine complex (TMC), a term that we adapt here. The distal slope of the TMC is characterized by multiple debris lobes showing hummocky surface topography (Fig.

3E). On SBP data, reflections potentially identifying slip planes between the TMC and associated debris lobes are absent (Fig. 2.5).

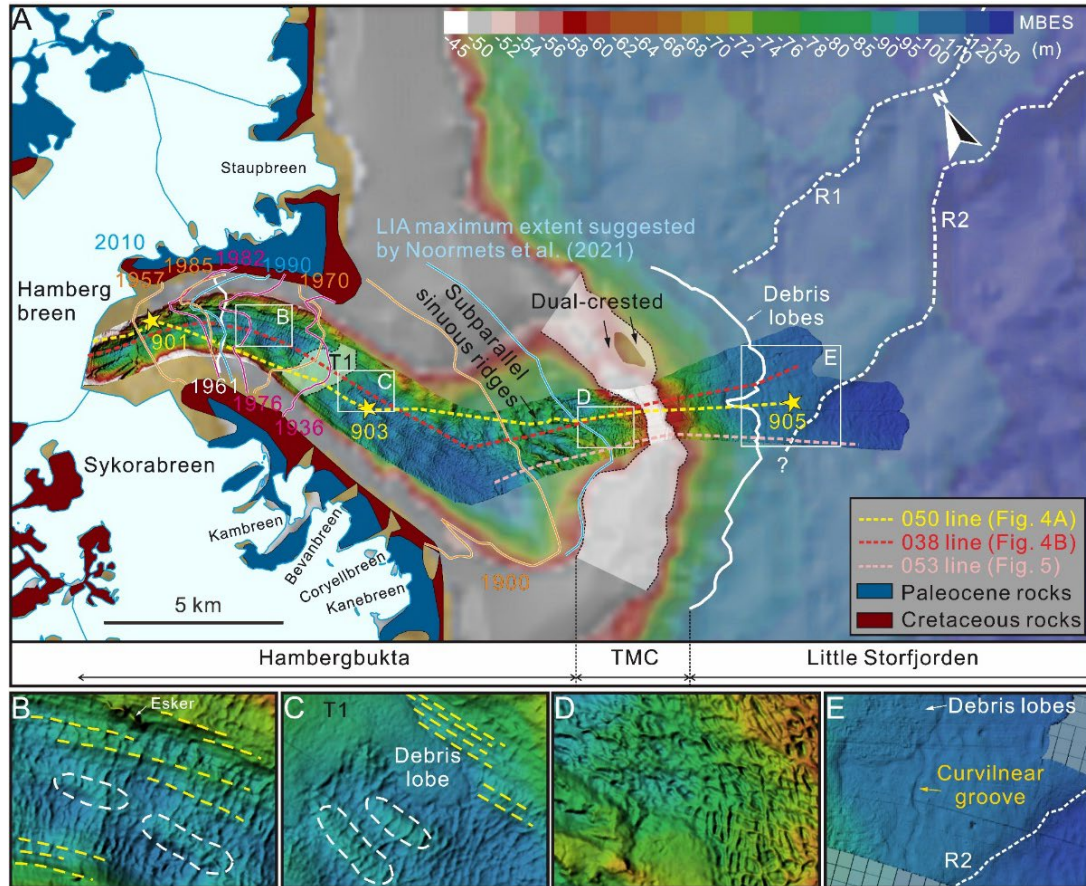


Fig. 2.3. (A) Multi-beam bathymetry of Hambergbukta and a downstream region (Little Storfjorden). Three yellow stars show gravity core locations. Yellow, red, and pink dotted lines are sub-bottom profiling (SBP) track lines. For the glacier extent in 2010, we used a shapefile of the 2001-2010 glacier area (Norwegian Polar Institute, 2013). The glacier fronts between 1900 and 1990 are based on Lefauconnier and Hagen (1991) and Noormets et al. (2021). On the distal side of the TMC, white solid and dotted lines indicate debris lobes (referred to Noormets et al., 2021) and NE-SW-oriented ridges (R1 and R2), respectively. Bedrock geology surrounding Hambergbukta is given according to the Norwegian Polar Institute. Panels (B) to (E) show high-resolution seafloor morphologies. In these panels, yellow dashed lines and white dashed circles indicate glacial lineations and drumlins. (B) Crevasse-fill ridges overlying drumlins in the inner basin, becoming subparallel towards the land. (C) A tongue of the debris lobe extends from the small terminal moraine (T1), partly covering former crevasse-fill ridges and lineations. (D) Crevasse-fill ridges on the proximal flank of TMC. (E) R2 and curvilinear grooves in the distal side of TMC.

Submarine landforms in the Little Storfjorden. A NE-SW striking ridge (R2) in Little Storfjorden is traced on our MBES (Figs. 3A, E) and SBP (053 line) data (Fig. 2.5). The southernmost part of R2 is located 3-5 km east of the crest of the TMC. On the SBP line (Fig. 2.5), R2 is recognized as a 12 m-thick and acoustically semi-transparent sediment wedge with a slope of 0.7 degrees dipping eastward (Fig. 2.5). Between the TMC and R2, the seafloor is relatively smooth without crevasse-fill ridges. However, overall N-S trending and curvilinear grooves are occasionally observed at about 100 m water depth (Fig. 2.3E). These grooves are 2 m deep with a relatively uniform width of about 100 m. Including these grooves, the sediment wedge (R2) is covered by an acoustically uniform sediment layer of 1 to 2 m in thickness (Fig. 2.5). As shown in the front of T1, several debris lobes extending outwards are also observed on the distal slope of the TMC (Fig. 2.3E). The debris lobe partly covers R2 (Fig. 2.5) and curvilinear grooves (Fig. 2.3E) draped by a relatively thin sediment drape.

2) Seismostratigraphy

High-resolution sub-bottom profiles from the Hambergbukta fjord head to Little Storfjorden present variable acoustic characteristics (Figs. 2.4, 2.5). In Hambergbukta, four acoustic units (F-1 to F-4) were defined in the previous study (Noormets et al., 2021). As the study area expanded to Little Storfjorden, we found the acoustic units older than the previously defined acoustic units. Furthermore, the acoustic units show different regional distributions and stratigraphic sequences. Hence, each acoustic unit was categorized into A, B, and C groups in this study to improve the previous seismostratigraphy (Fig. 2.6; Table 2.4).

Group (A). The acoustic units of Group (A) are distributed in the inner basin of Hambergbukta (Fig. 2.4). In Group (A), the lowermost unit (F-1A) is composed of the

small terminal moraine (T1) and associated debris lobes (Fig. 2.4), which is consistent with the earlier definition by Noormets et al. (2021). Above F-1A, a sediment layer is composed of F-3A and F-4A. F-3A is characterized by acoustic hyperbolas coinciding with crevasse-fill ridges and annual moraines (Fig. 2.4A). F-4A consists of acoustically (semi) transparent and uniform reflectors parallel to its lower boundary, which was interpreted as glaciomarine deposits by Noormets et al. (2021).

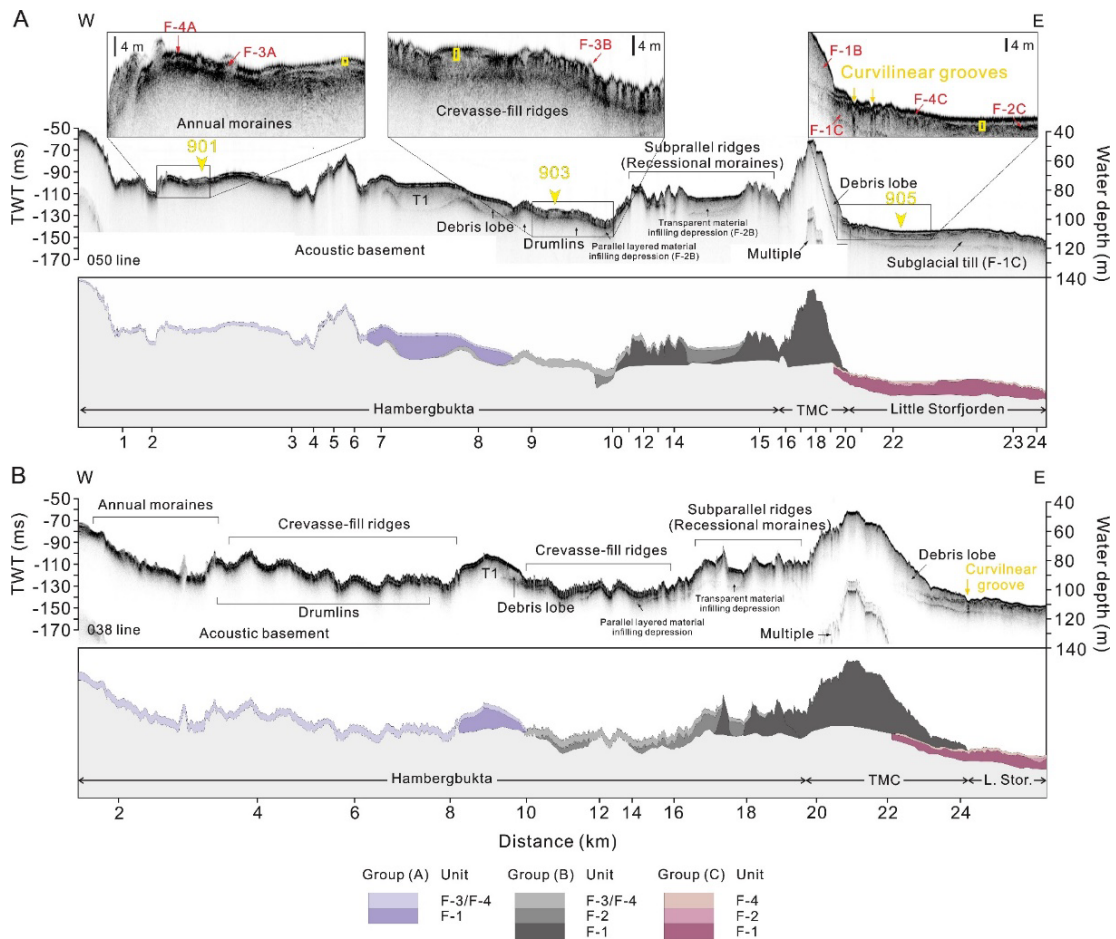


Fig. 2.4. Distribution of acoustic units (F-1 to F-4) re-defined in this study. (A) and (B) are SBP profiles on 050 and 038 track lines, respectively. Yellow boxes in panel (A) show the penetration depths for the studied cores. For the locations of gravity cores, see Fig. 2.3A.

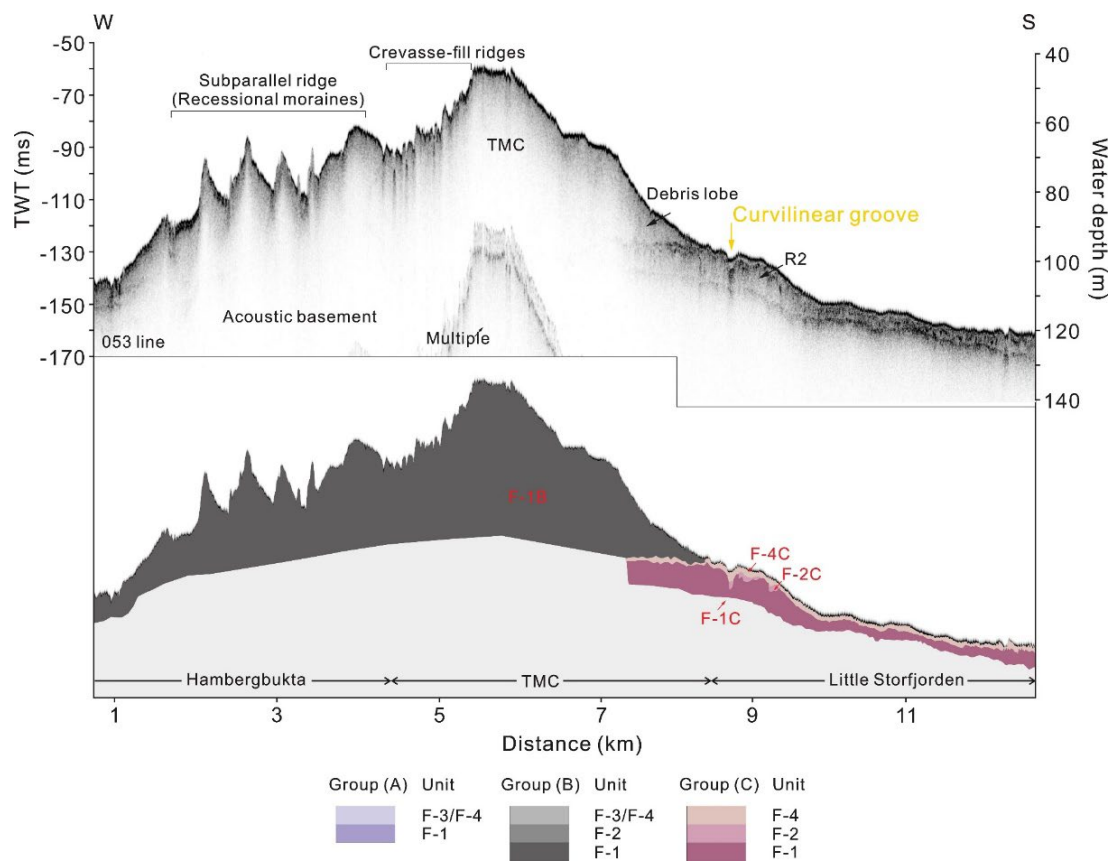


Fig. 2.5. SBP profile (053 line) around the fjord mouth showing a grounding zone wedge below the TMC and the associated debris lobe.

Group (B). At the proximal slope of T1, a debris lobe (F-1A) partly covers crevasse-fill ridges in the outer basin (Fig. 2.4A). Based on this stratigraphic relation, the acoustic units below F-1A are assigned to Group (B). F-1B is composed of TMC, associated debris lobes, and sub-parallel, sinuous ridges in the distal side of TMC (Figs 2.4, 2.5), which were defined as “F-1” in Noormets et al. (2021). Also, between the sinuous ridges and T1, hummocky morphologies, interpreted as drumlins (“F-1” defined in Noormets et al. 2021), were defined as the acoustic basement due to a lack of a reflection defining its lower boundary (Fig. 2.4A). F-2B is identified as the “Fill in” type in local depressions partly observed by F-1B geometry (Fig. 2.4). The unit is characterized by acoustically stratified and transparent reflection patterns in the outer

basin, interpreted as melt-out deposits of older, pre-surge, glacimarine, and/or marine sediments (Noormets et al., 2021). As the uppermost unit of Group (B), F-3B, featuring the crevasse-fill ridges, prevails in the outer basin, whereas F-4B is mainly observed in the seafloor of local depressions between sinuous ridges in the proximal side of TMC.

Group (C). This group is distributed on the distal side of TMC (Little Storfjorden) and stratigraphically below Group (B). Group (C) is composed of F-1C, F-2C, and F-4C. F-1C is a buried sediment wedge or subglacial till deposit corresponding to a NE-SW striking ridge (R2) in Little Storfjorden (Figs. 2.3, 2.5). F-2C is characterized by chaotic lenses (Table 2.3) between F-1C and F-4C (Fig. 2.5). In this region, the uppermost unit is defined as only F-4C due to the absence of diffraction hyperbolas coinciding with crevasse-fill ridges or annual moraines.

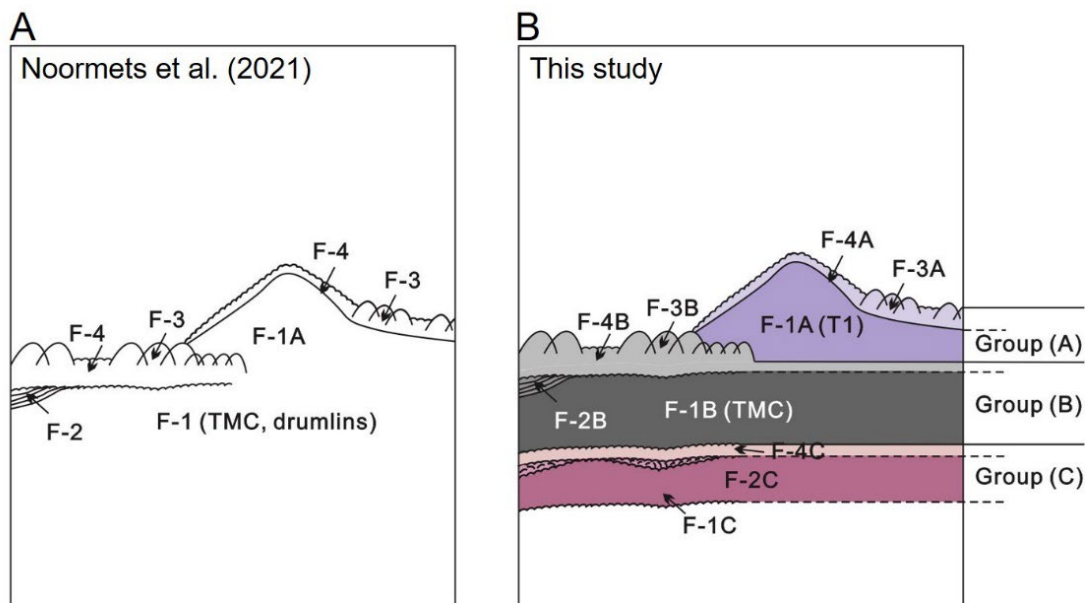
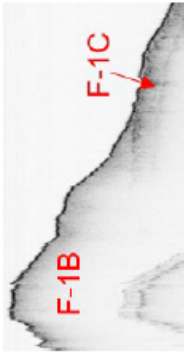
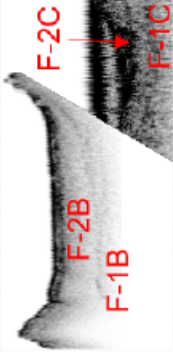
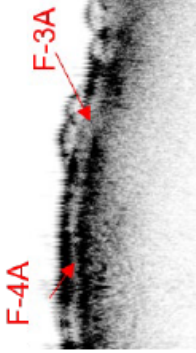


Fig. 2.6. Seismostratigraphies defined in (A) Noormets et al. (2021) and (B) this study. For interpretation and definition of acoustic units (F-1 to F-4), see Table 2.3.

Table 2.3. Classified acoustic units (see Figs. 4 and 5 for their distribution).

Acoustic unit		Description	Distribution	Interpretation
F-1	A		<p>F-1 unit is characterized by acoustically (semi) transparent, but occasional faint internal reflectors occur. Erosive and relatively flat lower boundaries were partly recognized. F-1A represents T1 and the associated debris lobe. The code was assigned to the definition by Noormets et al. (2021). F-1B is lower in the stratigraphic succession than F-1A, composed of TMC and the associated debris lobe and recessional moraines in the proximal side of TMC. F-1C is a grounding zone wedge in the distal side of TMC, located below F-1B.</p>	Subglacial till
	B			
	C			
F-2	A		<p>F-2 unit is composed of variable acoustic characteristics: the acoustically layered unit in front of T1 suggested F-2 by Noormets et al. (2021) and transparent depression-fill deposits between recessional moraines in the proximal side of TMC. These units generally overlie F-1B. Therefore, we defined this unit as F-2B in this study. Also, chaotic lenses occurred on the distal side of TMC. Based on its position that overlies F-1C, the chaotic lenses were defined as F-2C. F-2A was not determined.</p>	Glacial melt-out deposits
	B			
	C			
F-3 /F-4	A		<p>F-3 and F-4 units are the uppermost units of each group (A, B and C). F-3 is composed of overlapping diffraction hyperbolae (Noormets et al., 2021). F-4 consists of acoustically (semi) transparent and uniform reflectors, showing relatively parallel geometry to the lower boundary. In this study, the previously defined units F-3 and F-4 were sub-divided. Based on stratigraphic position, F-3 and F-4 units were defined as F-3/F-4A and F-3/F-4B in the inner and outer basins, respectively. On the distal side of TMC, only F-4C was defined due to the absence of diffraction hyperbola (F-3 type) on distal side of TMC.</p>	<p>F-3: crevasse-fill ridges and annual moraines. F-4: glaciomarine deposits.</p>
	B			
	C			

2.4.3. Sediment cores

In Hambergbukta, HH19-901-GC and HH19-903-GC (hereafter 901 and 903, respectively) were obtained from parts of the uppermost acoustic units (F-4A and F-4B, respectively) (Fig. 2.4A). They comprise olive-colored, stratified sediments with dark mottles (Figs. 2.7B, C). In Little Storfjorden, on the other hand, HH19-905-GC (hereafter 905) contains the top of a buried subglacial till deposit (F-1C) (Fig. 2.4A) and reveals distinct lithological changes in the overlying sediments (Fig. 2.7A). We defined five lithofacies based on sediment texture, structure, physical properties, and Zr/Rb and Ca/Sr ratios (For a summary of lithofacies, see Table 2.4). Whereas Facies 1 – 4 were identified in the core from Little Storfjorden, the entire cores from Hambergbukta are composed of facies 5.

Facies 1 is a massive diamicton composed of dark olive greyish, very poorly sorted, and semi-consolidated gravelly muddy sand (Fig. 2.7A), which is bounded at 226 cm in core 905 with a prominent lithological change. WBD is the highest (~ 2.3 g/cc) at the bottom and abruptly decreases above 237 cm core depth. On the other hand, MS is relatively constant with the highest values ($\sim 26\text{-}27 \times 10^{-5}$ SI) and decreases abruptly at the upper boundary. Zr/Rb and Ca/Sr ratios decrease upward with small amplitudes (Fig. 2.7A; Table 2.4). The massive diamicton Facies 1 is interpreted as a subglacial till (compare with Forwick and Vorren, 2009; Nielsen and Rasmussen, 2018), which is similar to the lowermost unit (till) of the previously investigated sediment cores in Hambergbukta (HH13-23 and HH13-21; Noormets et al., 2021).

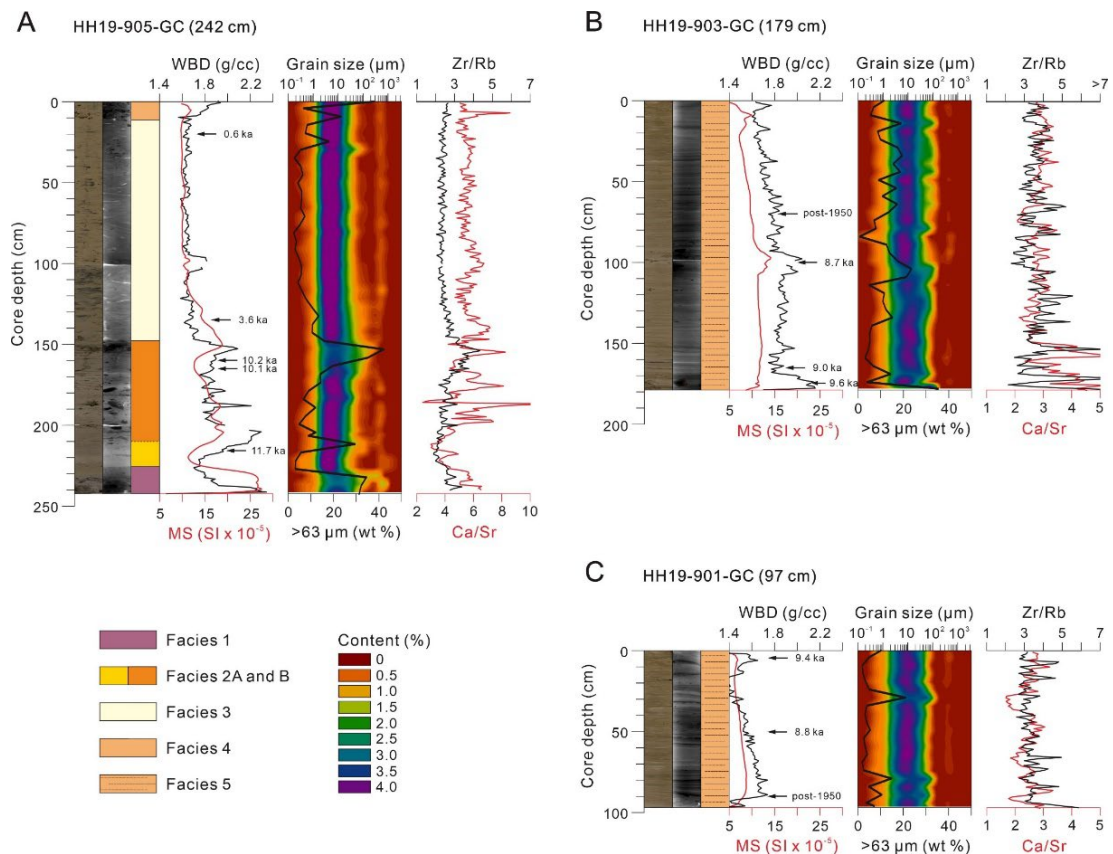


Fig. 2.7. Linescan images, X-radiographs, downcore distribution of lithofacies (Facies 1-5), physical properties (WBD and MS), the calendar ages of AMS ¹⁴C dates, and grain size, including the content of coarse particles larger than 63 μm, and elemental geochemistry. (A) is the result of core 905 obtained from the Little Storfjorden. (B) and (C) are cores 901 and 903 obtained from the fjord basin of Hambergbukta.

Facies 2 is olive-colored and massive, subdivided into Facies 2A (226-210 cm) and 2B (210-148 cm). Facies 2A is composed of sandy mud. Facies 2B is characterized by lots of dropstones (20-70 mm in diameter) (Fig. 2.7A). In Facies 2B, the content of coarse particles (>63 μm) increases at the bottom and top. Notably, the top of Facies 2B contains coarse particles of 40 weight percent (wt %) without dropstones. WBD and MS increase at the transition from Facies 2A to 2B. In Facies 2B, WBD and MS fluctuate, but decrease, upward but increase again at the top. The Zr/Rb ratio gradually increases toward the top, whereas the Ca/Sr ratio highly fluctuates. Above the subglacial till, deposition of a massive, finer-grained Facies 2A might reflect a slow

retreat or a relatively stagnant ice front, or a setting in which iceberg drifting suppressed due to perennial sea ice cover (Łącka et al., 2015). Also, it may reflect the cold sea water condition where drifting icebergs did not melt and released their debris. In Facies 2B, the occurrences of numerous dropstones suggest the enhanced deposition of iceberg-rafted debris (IRD) (Gilbert, 1990). Corresponding to the occurrence of dropstones, strong fluctuations of Ca/Sr reflect depositional variability of detrital carbonates as ice/iceberg-rafted debris. On the other hand, an upward increase of Zr/Rb means the sorting of coarse-grained siliciclastic sediments by enhanced winnowing of fine-grained sediments.

Facies 3 consists of olive-colored, bioturbated sandy mud with dispersed clasts (148-12 cm). The dispersed clasts are regular (2-4 mm) in size. However, relatively large clasts (up to 20 mm in diameter) are concentrated at 25-30 cm (Fig. 2.7A). The content of coarse particles slightly decreases upcore in the lower part (148-80 cm) and increases towards the top (Fig. 2.7A). At the transition between Facies 2 and 3, WBD decreases abruptly, whereas the MS gradually decreases upcore (148-100 cm). In Facies 3, WBD and MS are generally low and constant, but a small peak of WBD has been observed around 100 cm core depth. The Zr/Rb ratio is relatively stable around an average value of 2.4. The Ca/Sr ratio is overall stable but slightly increases at the bottom and 105-85 cm core depths. Abundant bioturbation in Facies 3 represents a glacier-distal glacialmarine environment with favorable living conditions for benthic organisms (Forwick and Vorren, 2009; Lucchi et al., 2013; Nielsen and Rasmussen, 2018). In Facies 3, the deposition of regular and small clasts can reflect the influence of sea ice-rafted debris (Gilbert, 1990) and icebergs drifting at a larger distance from the ice margin.

Facies 4 (12-0 cm) is olive-colored, slightly bioturbated sandy mud without large dropstones. The content of coarser particles ($>63 \mu\text{m}$) is up to 39%. However, lots of large clasts (1-20 mm in diameter) are observed on the x-radiograph (Fig. 2.7A). WBD increases towards the core top, whereas MS shows a small peak. The values of Zr/Rb remain constant across the Facies 3 to Facies 4 transition. However, a positive peak of Ca/Sr is observed in the transition between Facies 3 and 4. In Facies 4, the increase of various-sized clasts indicates that Little Storfjorden has been influenced mainly by drifting icebergs and sea ice (compare with Gilbert, 1990).

Facies 5 is characterized by olive-colored, well-stratified sandy muds with dispersed clasts, observed in two cores, 901 and 903 (Figs. 6B, C). Clasts are variable in size. Large dropstones of up to 7 cm in diameter are identified at 90-105 cm and the bottom of core 903 (Fig. 2.6B). The content of coarse particles ($>63 \mu\text{m}$) ranges from 2 to 22 wt %. Stratification occurs predominantly in the form of sub-horizontal lamination with irregular laminae thickness. However, some layers thicker than 1 cm occur occasionally. In core 901, WBD and MS overall decrease upward but increase in the uppermost part (15-0 cm). In core 903, WBD and MS show similar trends with core 901. However, WBD markedly increases corresponding to the occurrences of large dropstones in core 903. The Zr/Rb ratio strongly fluctuates in Facies 5. In particular, many positive peaks of Zr/Rb are well-matched with coarse-grained laminae and/or layers (Figs. 2.7B, C). In core 901, the Ca/Sr ratio increases in coarse-grained intervals in which outsized clasts were deposited. However, the ratio of core 903 highly fluctuates in the lowermost part. Cores 901 and 903 are consistent with the upper units that consist of mud with occasional outsized clasts and sandy layers and lenses of the Hambergbukta cores defined by Noormets et al. (2021). In particular,

well-pronounced stratification and some clasts in Facies 5 reflect recent glacial fluctuations, including the LIA surge event in Hambergbukta (Lefauconnier and Hagen, 1991; Ziaja and Ostafin, 2015; Noormets et al., 2021). The difference in Zr/Rb and Ca/Sr variations indicates different transport mechanisms. Coinciding with coarse-grained laminae and layers, many peaks of the Zr/Rb ratio reflect the deposition of siliciclastic sediments by meltwater plumes discharged repeatedly from the tidewater glacier (Hambergbreen) during the recent glacial fluctuations in Hambergbukta. On the other hand, an increase of the Ca/Sr ratio, related to the occurrences of coarse clasts including dropstones, would be caused mainly by detrital carbonate deposition by drifting ices calved from Hambergbreen.

Table 2.4. Lithofacies classified on the studied cores.

Sedimentary facies	Description	Age and genesis
Facies 1 Core 905 226-242 cm	Dark olive-grey, very poorly sorted, semi-consolidated gravely sandy mud with outsized clasts; massive, the highest values of WBD and MS were measured at the bottom, the values decrease upwards; Zr/Rb and Ca/Sr ratios decrease upward, ranging from 3.4 to 2.5 and 6.6 to 4.3, respectively.	Subglacial till deposits during the Younger Dryas
Facies 2 Core 905 148-226 cm	Olive, very poorly sorted, sandy mud to gravely sandy mud with clasts in various sizes (1-7 cm in diameter), the amount of clasts significantly increases above 210 cm (a black dashed line); massive, a distinct lithological change to Facies 1; this facies is divided into finer-grained Facies 2A and coarser-grained Facies 2B, the upper facies (2B) shows the highest content (up to 40%) of coarse particles (> 63µm); WBD and MS correlate with the content of coarse particles; Zr/Rb gradually increases upward (1.9 to 4.3), but high values of Ca/Sr are observed in clast-rich intervals.	IRD deposits by icebergs carving from the glacial front (in glacier-proximal setting) Facies 2A : Younger Dryas-Holocene transition (12-11.7 ka) Facies 2B : Early Holocene (11.7-10.1 ka)
Facies 3 Core 905 12-148 cm	Olive with dark mottles; sandy mud with dispersed clasts (2-4 mm in diameter), outsized clasts of up to 2 cm are rarely recognized but concentrated in the upper part (2.5-30 cm); bioturbated; a distinct lithological change to Facies 2; WBD is relatively low and constant, MS decreases upward in the lowermost part (100-148 cm); Zr/Rb is relatively low and constant with an average value of 2.4, multiple variations of Ca/Sr follow the content of coarse particles including outsized clasts.	Glacimarine deposits influenced by drifting sea ice during the Late Holocene (in glacier-distal setting) (3.7-0.4 ka)
Facies 4 Core 905 0-12 cm	Olive with some dark mottles; sandy mud with lots of clasts ranging from 1 mm to 2 cm in diameter, high contents (up to 39%) of coarser particles; slightly bioturbated; a relatively distinct lithological change to Facies 3; WBD markedly increases toward the top, whereas MS slightly increases; Zr/Rb is relatively low and constant with an average value of 2.4, Ca/Sr is also relatively low but reaches a peak of 8.58 between the transition Facies 3 and 4.	Glacimarine deposits influenced by drifting icebergs calving from tidewater glaciers and drifting sea ice (0.4 ka to present)
Facies 5 Core 901 Core 903	Olive, dark mottles are rarely observed; sandy mud with dispersed clasts ranging from 2 mm to 1 cm, outsized clasts of up to 7 cm in diameter are occasionally identified at 90-105 cm, and the bottom of core 903; well-stratified with sub-parallel laminae; WBD and MS overall decrease upwards, relatively higher WBD is observed at 90-105 cm of core 903 corresponding to the occurrence of outsized clasts; Increase of WBD is observed in the uppermost part (0-15 cm) of core 901; Zr/Rb is generally fluctuated, increase of Zr/Rb corresponds to coarse-grained laminae and layers, Ca/Sr increases in coarse-grained intervals than outsized clasts occurred.	Glacimarine deposits influenced by meltwater plumes and drifting icebergs discharged from Hambergreen (post-1950)

2.4.4. Chronostratigraphy and sedimentation rates

For the studied cores, AMS ^{14}C dates and converted calendar ages are summarized in Table 2. To constrain the age-depth modeling in BACON, we used four ages in core 905. An age point at 160-159 cm showing a small reversal was excluded from the modeling.

Based on the weighted mean values extracted by the BACON modeling, the bottom age of core 905 was calculated to be 12.4 ka (Fig. 8). Changes in the overall sedimentation rates of core 905 are similar to those of core HH12-1209 from a nearby site in eastern Storfjorden (Rasmussen and Thomsen, 2014) (Fig. 2.8). According to the age model, the diamicton Facies 1 was deposited before 12.0 ka. Facies 2A was constrained to 12.0-11.6 ka. Except for the very low sedimentation zone (~ 5.5 cm/kyr) between 10.1 ka and 3.7 ka, Facies 2B can be constrained to 11.6-10.1 ka. Between 12.0 ka and 10.1 ka, an average sedimentation rate is ~ 32.6 cm/kyr. Facies 3 was deposited after 3.7 ka with an average sedimentation rate of 37.5 cm/kyr. In Facies 3, an abrupt increase in large clasts is identified in the time interval from 0.9 ka to 0.7 ka (at 25-30 cm core depth). Facies 4 was deposited after 0.4 ka with an average sedimentation rate of 31.6 cm/kyr. Based on the occurrences of the materials younger than 1950 AD (Fig. 2.7B, C), two cores 901 and 903 are at least younger than 1900 years. Although significantly old materials were identified in both two cores, these are interpreted as reworked materials by sediment mixing and re-deposition after the LIA surge in Hambergbukta (Noormets et al., 2021). Assuming that the bottom age of core 901 is 1950 AD or younger, the minimum sedimentation rate in the Hambergbukta fjord basin can be calculated as higher than 1 cm per year, which is considerably higher than in core 905.

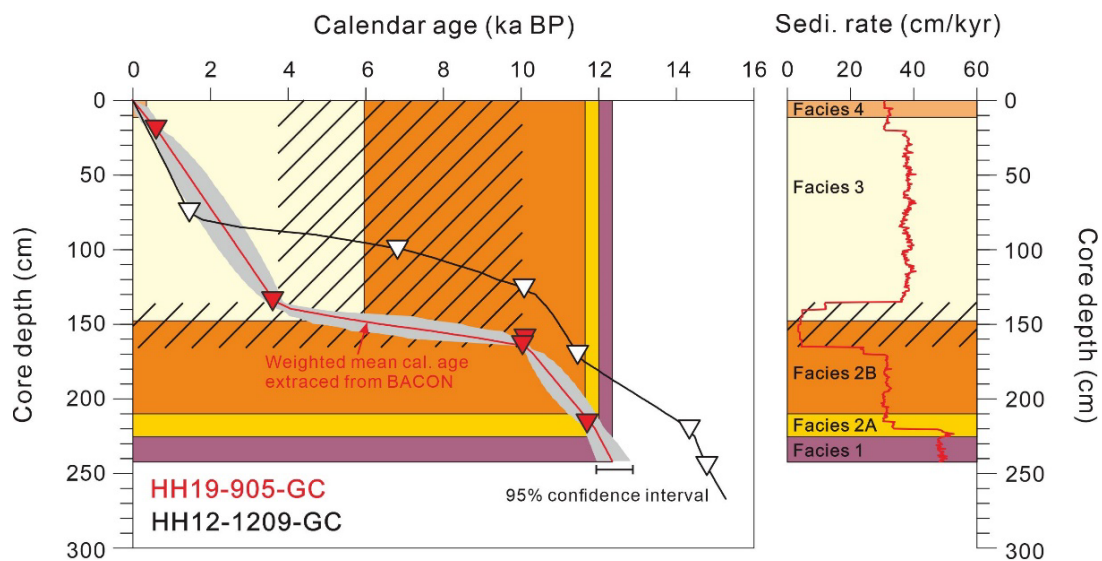


Fig. 2.8. Comparison of sedimentation rates between Little Storfjorden (core 905) and eastern Storfjorden (HH12-1209-GC) based on the age model applying to the Marine 20 dataset (Heaton et al., 2020) and a regional ΔR of -61 ± 37 (Pieńkowski et al., 2021). For comparison between the previously published age model (Marine 13) and the new age model of the six sediment cores in eastern Storfjorden (Fig. 2.2), see Supplementary Fig. 1.

2.4.5. Organic geochemistry

In the cores 901 and 903 (Hambergbukta), the TOC slightly fluctuates around average values of 1.28% and 1.24 %, respectively (Fig. 2.9). The $\delta^{13}\text{C}_{\text{org}}$ is more constant with an average value of approximately -24.9‰ in both cores. Organic nitrogen (N_{org}) is relatively low, ranging from 0.01 to 0.03%. Overall, the TOC/ N_{org} ratio is higher than 20. The ratio significantly increases below 50 cm core depth in both cores due to very low organic nitrogen of 0.01%.

In core 905 (Little Storfjorden), variations in TOC and $\delta^{13}\text{C}_{\text{org}}$ correspond to lithofacies changes (Fig. 2.9). As massive diamicton Facies 1 changes to dropstone-rich Facies 2B, TOC and $\delta^{13}\text{C}_{\text{org}}$ values decrease upward to 1.27% and -26‰ , respectively (Fig. 2.9). A transition between Facies 2 and 3 is characterized by an abrupt increase in the two parameters. The increased TOC remains constantly in Facies

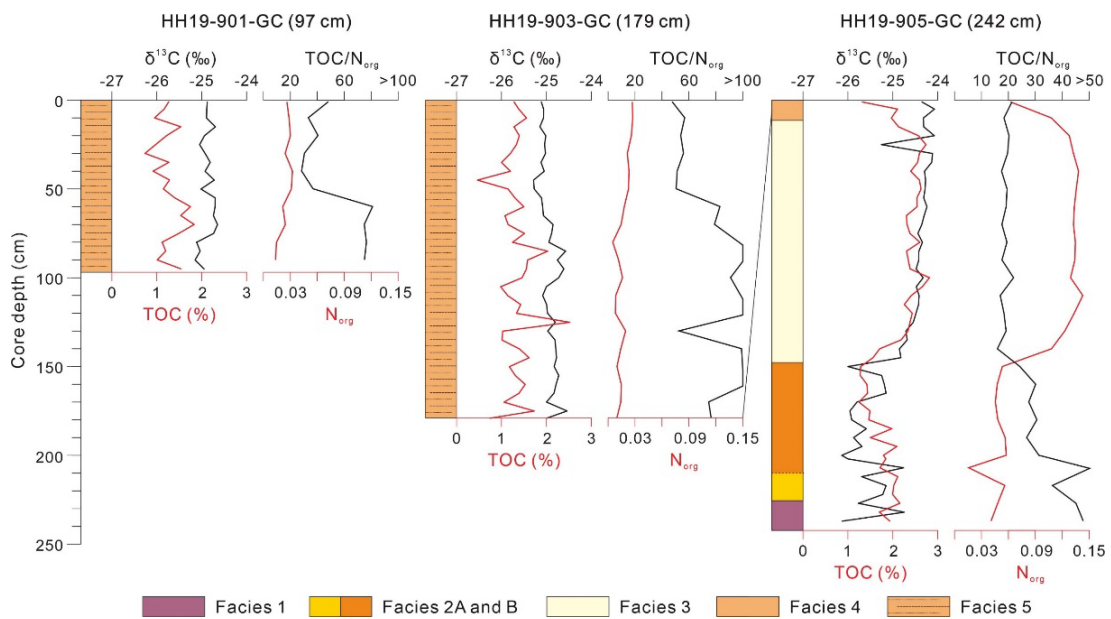


Fig. 2.9. Downcore distribution of organic carbon stable isotope values ($\delta^{13}\text{C}$), TOC, TOC/ N_{org} and N_{org} .

3 and then decreases to 1.32% in Facies 4. Overall, $\delta^{13}\text{C}_{\text{org}}$ values are higher than -25‰ in Facies 3 and 4. However, an abrupt decrease in $\delta^{13}\text{C}_{\text{org}}$ is observed in the interval where large clasts increase. The content of N_{org} in core 905 ranges from 0.04 to 0.14%. From Facies 1 to 2, the TOC/ N_{org} ratio generally decreases (47.64 to 24.18). However, the ratio is significantly increased up to 109.03 in a transition between Facies 2A to 2B (Fig. 2.9). Above Facies 2, the decreased TOC/ N_{org} ratio remains constant with an average value of 19.23.

2.5. Discussion

2.5.1. Age constraints of seismostratigraphy

Sub-bottom echo characters are well-correlated with lithological changes in core 905 (Fig. 2.10). The massive diamicton Facies 1 corresponds to the top of F-1C. Massive Facies 2 containing lots of dropstones is identified as chaotic lenses (F-2C) in the seismic record. Considering the bottom age (~12 ka) of Facies 2, the timing of deposition of F-1C is constrained to the Younger Dryas (YD). Therefore, the NE-SW-oriented R2 possibly indicates the maximum extent of the marine-based glacier in the Little Storfjorden during YD, which is closely related to the deposition (13-12 ka) of the middle grounding zone wedge G2 in eastern Storfjorden (Nielsen and Rasmussen, 2018). Except for the transition between Facies 2 and 3 characterized by the very low sedimentation, F-2C includes the time intervals of the YD-Holocene transition (12~11.7 ka) and parts of the early Holocene (11.7-10.1 ka). The acoustically uniform and transparent echoes of F-4C reflect relatively fine-grained and bioturbated Facies 3 with dispersed small clasts, representing the late Holocene. The strong surficial reflector of F-4C presumably includes the Facies 4 and uppermost parts of Facies 3, which might be deposited since approximately 1000 years BP.

Fig. 2.5 shows that the debris lobe extended from TMC, defined as F-1B, overlies F-4C. This stratigraphic relation indicates that TMC and the associated debris lobe have formed during the latest Holocene, possibly related to a glacial surge event during LIA. Alternatively, F-1B might also correlate with the upper part of F-4C. Therefore, it could not exclude that TMC is older than the LIA. The former is consistent with the initial estimation of Lefauconnier and Hagen (1991). On the other

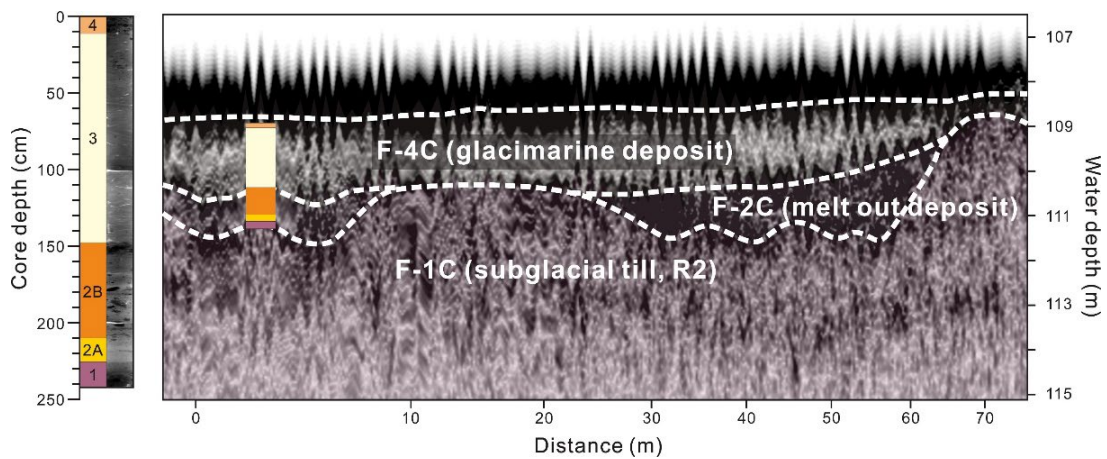


Fig. 2.10. Correlation of the acoustic units with lithofacies of core 905 from Little Storfjorden.

hand, the latter can be related to the recent estimation by Noormets et al. (2021). We will discuss these controversial estimates in chapter 5.3. Regardless of TMC, F-2B, F-3B, and F-4B in the proximal side of TMC are defined as deglacial sediments deposited after 1900 AD. Corresponding to the 1970 glacier front (Fig. 2.3A), the development of T1 and associated debris lobes (F-1A) indicates that F-3A and F-4A have been deposited since the last surge event (1961-1970).

2.5.2. Glacial history and depositional environments

1) Younger Dryas cold period

Based on the core-seismic correlation, the NE-SW oriented grounding zone wedge R2 represents the position of the YD glacier front in Little Storfjorden (Fig. 2.11A). Regarding age, orientation, and latitudinal position, R2 is similar to the middle grounding zone wedge G2 in eastern Storfjorden (Nielsen and Rasmussen, 2018).

The YD stadial is characterized by dramatic cooling based on Greenland ice core $\delta^{18}\text{O}$ -temperature reconstructions (Liu et al., 2012). This cooling event was recognized by the advances of ice streams in the northwestern, western, and southwestern portions

of the Laurentide Ice Sheet (e.g., Margold et al., 2018) and local glaciers in north Greenland (Larsen et al., 2016). However, the behavior of the Svalbard glaciers has shown regional differences. In several fjords of northwestern Svalbard, no sediment records indicate the significant advance of marine-based and/or tidewater glaciers (Bartels et al., 2017), although the possibility of re-advance was suggested (Allaart et al., 2020; Jang et al., 2021). In western Svalbard, the previous reconstruction and the compiled data sets in Isfjorden suggested a re-advance of tidewater glaciers during this period (Svendsen et al., 1996; Forwick and Vorren, 2009). Notably, a prominent re-advance of a marine-based glacier was identified in eastern Storfjorden of southern Svalbard during the YD period (Nielsen and Rasmussen, 2018; Rasmussen and Thomsen, 2021). Nielsen and Rasmussen (2018) inferred that the ice-proximal fan buried beneath G1 (Fig. 2.11A) was possibly deposited during the Allerød interstadial (14.5 ka), and an ice stream/marine-based glacier advanced southerly during YD (13-12 ka) led to the formation of G2. In particular, this scenario could explain the high sedimentation rates of coarse material in this time interval observed in two cores (HH12-1209GC and HH12-1212GC) from the distal side of G2 (Fig. 2.2A). Although we could not determine how far the ice stream of Little Storfjorden had retreated during the Allerød interstadial, since the survey area was limited to the vicinity of Hambergbukta, our result suggests that the marine-based glaciers in both western and eastern parts of Storfjorden were extended south around 77° N during YD.

2) Younger Dryas-Holocene transition and early Holocene

Facies 2 was deposited between 12 ka and 10.1 ka. Based on our age model, Facies 2A, containing relatively small amounts of IRD, was constrained to the YD-Holocene transition (12.0-11.6 ka). Before discussing this short time interval, we first

compared the previously published age model (Marine 13) and the new-age model for the six sediment cores in eastern Storfjorden reported by Rasmussen and Thomsen (2014) and Nielsen and Rasmussen (2018) (Supplementary Fig. 2.1). The result presents that the new age model does not substantially change the previously defined time intervals.

In core 905, lithological change from Facies 1 to Facies 2 suggests sediment deposition in an ice-proximal setting after YD. Deposition of finer-grained Facies 2A indicates that the glacial retreat during the YD-Holocene transition was relatively stagnant or the iceberg drifting suppressed due to perennial sea ice cover (Łącka et al., 2015). In eastern Storfjorden, a massive intrusion of warm Atlantic Water caused a rapid glacier retreat of 20 km during this period (Rasmussen and Thomsen, 2014; Nielsen and Rasmussen, 2018), identified as an increase in IRD and the formation of G1. During this period, deposition of finer-grained Facies 2A indicates a relatively weak melting of a marine-based glacier in Little Storfjorden. In this regard, we interpret that the intrusion of Atlantic Water might have gradually expanded to Little Storfjorden as the glacial retreat of eastern Storfjorden progressed (Fig. 2.11B). In addition, a narrow morphology of Little Storfjorden would have played an essential role in glacier stabilization, causing relatively slow glacial retreat. As a result, the marine-based glacier in Little Storfjorden started to retreat slower than eastern Storfjorden during this period, which is consistent with the earlier estimation by Nielsen and Rasmussen (2018). In this context, we infer that the occurrence of R1, located 3 km north of R2, might present the position of the Little Storfjorden glacier during the YD-Holocene transition (Fig. 2.11B). Further investigations in the inner (northern) part of Little Storfjorden are needed to confirm our estimation. Deposition

of the dropstone-rich Facies 2B indicates the collapse and substantial melting of the formed ice stream/marine-based glacier in Little Storfjorden near Hambergbukta at the onset of the Holocene. At the transition between Facies 2A and 2B, an abrupt increase of the TOC/N_{org} ratio indicates a strong terrestrial input to Little Storfjorden (Knies and Martinez, 2009), indirectly supporting our interpretation.

3) Middle to late Holocene

Coinciding with marked changes in WBD and organic geochemistry (Figs. 2.7, 2.9), a transition between Facies 2 and 3 is characterized by the very low sedimentation with an abrupt increase of coarse grains (up to 40%) between 10.1 ka and 3.7 ka (Fig. 2.7A). This time interval includes the late phase of the early Holocene and middle Holocene.

During the early to middle Holocene, the disappearance of marine-based glaciers/ice streams in southern Svalbard was marked by little or no IRD deposition and/or hiatus in eastern Storfjorden and Storfjorden Trough (Rasmussen and Thomsen, 2014, 2015; Łacka et al., 2015; Nielsen and Rasmussen, 2018; Rasmussen and Thomsen, 2021). Furthermore, the glacial lake sediment records suggested that the Svalbard glaciers retreated to their minimum extent during the beginning of the middle Holocene (Fansworth et al., 2020 and references therein). In the transition between Facies 2B and 3, changes in the TOC/N_{org} ratio and $\delta^{13}\text{C}_{\text{org}}$ indicate a reduced terrestrial input as the marine-based glacier was rapidly melted out in Little Storfjorden. Notably, in several cores from eastern Storfjorden, the increase of *Cibicides lobatulus* indicates that Storfjorden was affected by a strong bottom current during the early to middle Holocene (Rasmussen and Thomsen, 2015). Based on this foraminiferal proxy, we interpret that a coarse layer at the top of Facies 2B resulted from the winnowing

process by bottom current rather than glacial advance (Fig. 2.11C).

In Little Storfjorden, the late Holocene sediments are entirely bioturbated, containing dispersed clasts (Facies 3). This lithological characteristic indicates glacial-marine environments prevailed in the glacier-distal setting and oceanographic conditions (Forwick and Vorren, 2009; Lucchi et al., 2013; Rasmussen and Thomsen, 2014; Nielsen and Rasmussen, 2018). A scatter of regular and small-sized clasts can result from the deposition of debris governed by sea ice transportation (Gilbert, 1990). In Facies 3, high TOC (2.35%) and relatively heavy $\delta^{13}\text{C}_{\text{org}}$ (-24.49‰) indicate the enhanced primary productivity related to seasonal sea ice conditions. In the Arctic Ocean, the primary production increases at the sea ice edge and near the Arctic Front (Johannessen, 1987; van Aken et al., 1991; Wollenburg and Kuhnt, 2000). In Storfjorden, the high primary productivity reflects seasonal sea ice conditions (Winkelmann and Knies, 2005). Notably, most sediment records in eastern Storfjorden indicate seasonal sea ice conditions during the late Holocene, marked by the periodic maximum of brine formation (Rasmussen and Thomsen, 2014).

Some large clasts in Facies 3 possibly indicate the occurrence of the tidewater glaciers in the coastal areas, which reflects relatively cooler conditions in Svalbard during the late Holocene (Hald et al., 2014; Forwick and Vorren, 2009; Skirbekk et al., 2010; Rasmussen and Thomsen, 2014; Nielsen and Rasmussen, 2018; Jang et al., 2021). However, prominent glacier impacts did not occur in Little Storfjorden before 0.9 ka.

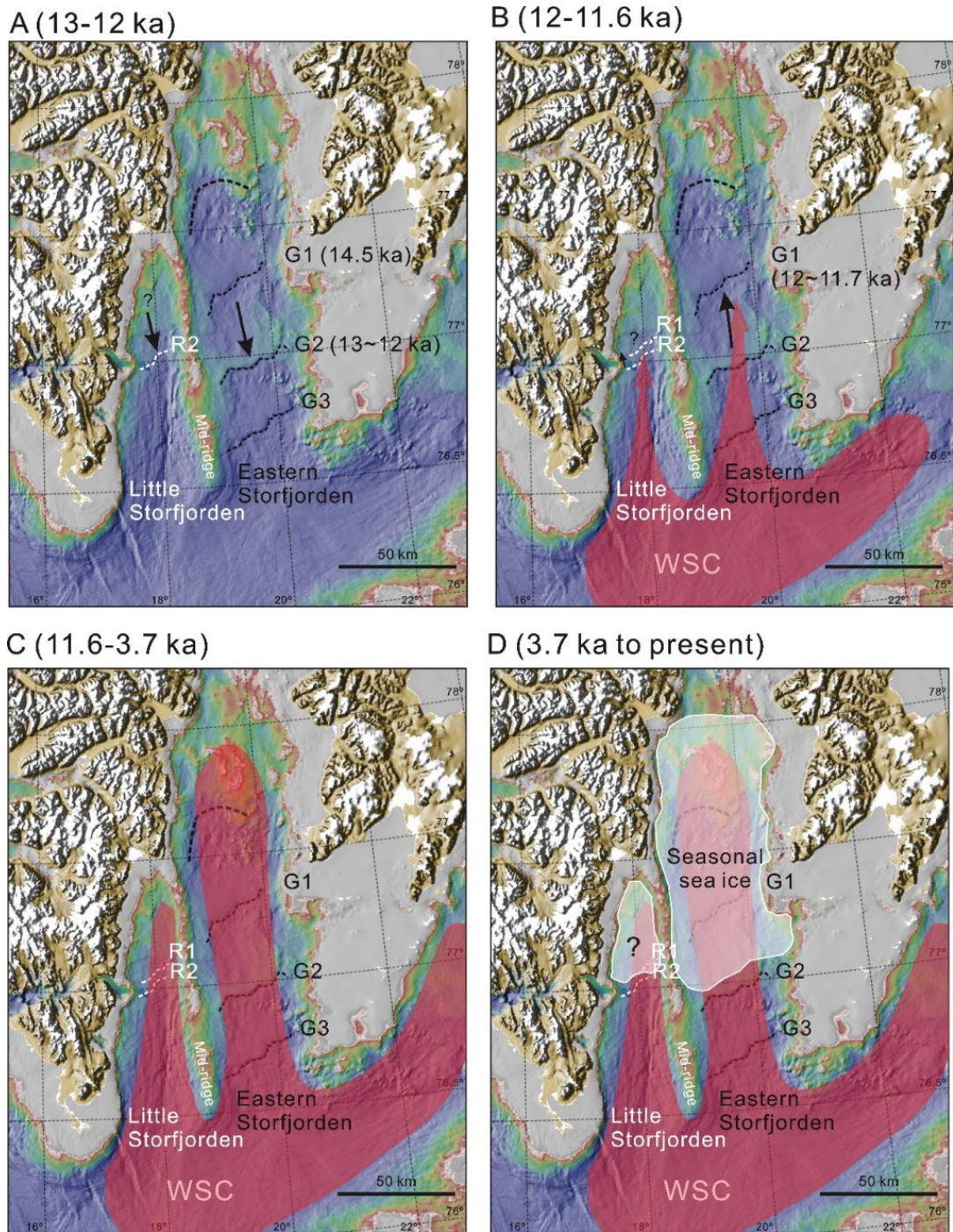


Fig. 2.11. Reconstruction of depositional environment and glacial history in the Hambergbukta and Little Storfjorden since Younger Dryas: (A) Younger Dryas stadial period (13-12 ka), (B) Younger Dryas to Holocene transition (12-11.6 ka), (C) the early to middle Holocene (11.6-3.7 ka), and (D) the late Holocene. The extent of seasonal sea ice in panel D was inferred based on sediment core records from Rasmussen and Thomsen (2015).

2.5.3. Large terminal moraine formed during LIA glacial surge

The fjord mouth of Hambergbukta is characterized by a large terminal moraine complex (TMC) and the associated debris lobes on its distal flank (Fig. 2.3A). In the proximal flank of the moraine (Fig. 2.3D), the occurrence of crevasse-fill ridges indicates that the moraine was deposited at the termination of a glacier surge in Hambergbukta (Solheim, 1991; Ottesen and Dowdeswell, 2006; Dowdeswell et al., 2016; Noormets et al., 2021). Previously, Lefauconnier and Hagen (1991) suggested that the terminal moraine would represent the maximum extent of the surging tidewater glacier in Hambergbukta during Little Ice Age (LIA). However, Noormets et al. (2021) recently interpreted the moraine as a terminal moraine complex (TMC) formed by repeated surge events before LIA. They suggested that the LIA surge and retreat caused deposition of the end-moraine zone (sinuous and subparallel ridges) on the proximal side of the terminal moraine (Fig. 3A).

Morphologically, Noormets et al. (2021) argued that the occurrence of crevasse-fill ridges between the two crests of the northern part of the TMC would indicate nonsynchronous glacial surge events. However, these features are only partially recognizable in the northern part of the terminal moraine, even compared with the inner fjord of Wahlenbergfjorden (Flink et al., 2017). Furthermore, multiple-crested terminal moraine can also be formed by glaciotectonic processes (Hambrey et al., 1997; Bennett et al., 1999; Boulton et al., 1999). In Svalbard fjords, glacial surges have formed terminal moraines and associated debris lobes (Boulton et al., 1996; Plassen et al., 2004; Ottesen and Dowdeswell, 2006; Dowdeswell et al., 2016). In Hambergbukta, a glacial surge event in 1961-1970 resulted in the formation of T1 (mid-fjord end moraine in Noormets et al., 2021) (Fig. 2.3A). Debris lobes extended from T1 partly

cover earlier crevasse-fill ridges (Figs. 2.3C, 2.4). If the subparallel sinuous ridges were formed by a glacial surge that occurred shortly before 1900 (Fig. 2.3A) (Noormets et al., 2021), the associated debris lobes would have partly covered the previously formed crevasse-fill ridges on the proximal flank of TMC. However, these features could not be identified in bathymetry and seismic data in this region.

For the timing of the TMC formation, the different estimations could result from insufficient chronological data (Lefauconnier and Hagen, 1991; Noormets et al., 2021). Our results could not provide direct evidence for constraining the exact timing of the LIA maximum in Hambergbukta either. However, the stratigraphic relation between F-4C and F-1B suggests that the large terminal moraine was formed during the late Holocene (see section 5.1). To better constrain the timing, we note the upper part of core 905 corresponding to F-4C (Fig. 2.10). In Little Storfjorden, the late Holocene sediments consist of Facies 3 and 4. In Facies 3, bulk organic chemistry is relatively constant (Fig. 2.9), suggesting that Little Storfjorden was in glacier-distal and/or open-marine conditions during the late Holocene. At 25-30 cm of core 905, an increase of large clasts might indicate a glacial surge. This interval was constrained to 0.9-0.7 ka, which belongs to the Medieval Warm Period (Rasmussen and Thomsen, 2015). Hence, during this warm period, the deposition of large clasts would indicate the glacial retreat of former tidewater glaciers on the western coast of Little Storfjorden. Noticeable deposition of IRD in Little Storfjorden is identified only in Facies 4 and the uppermost part of Facies 3 of core 905. These lithological characteristics suggest that prominent advances and retreats of tidewater glaciers in tributary fjords of Little Storfjorden including Hambergbukta have occurred after at least 1000 years BP, which differs from the earlier estimation by Noormets et al. (2021).

Based on sediment core records and seismostratigraphy, we suggest that the TMC represents the maximum extent of glacier advance (or surge) during LIA, and interpret the subparallel and sinuous ridges, interpreted as the end moraine zone by Noormets et al. (2021), into recessional moraines deposited after the LIA glacial surge until 1900 AD (Fig. 2.11).

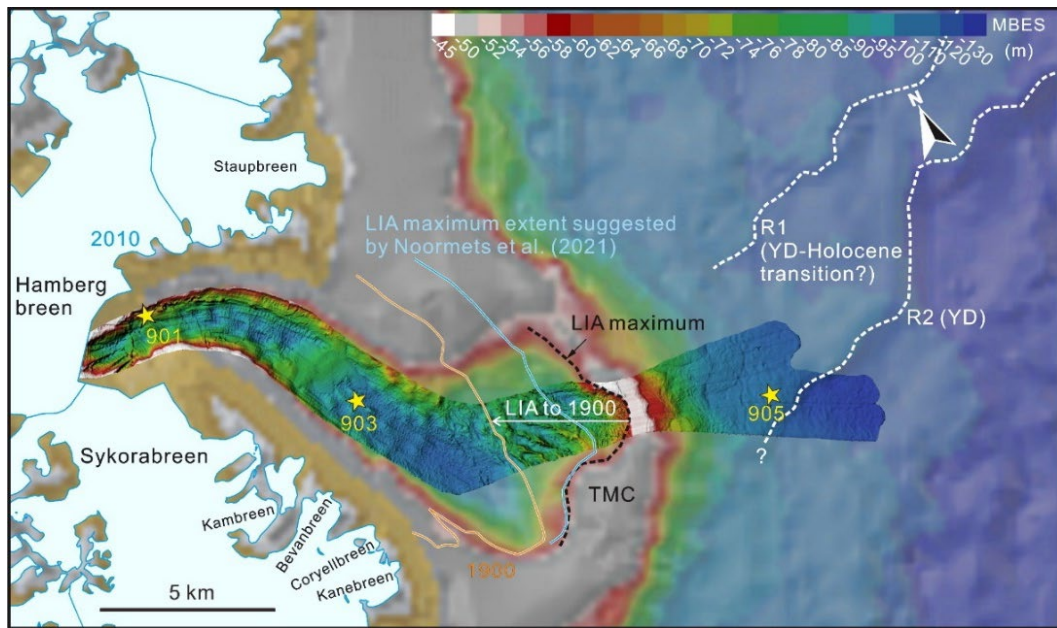
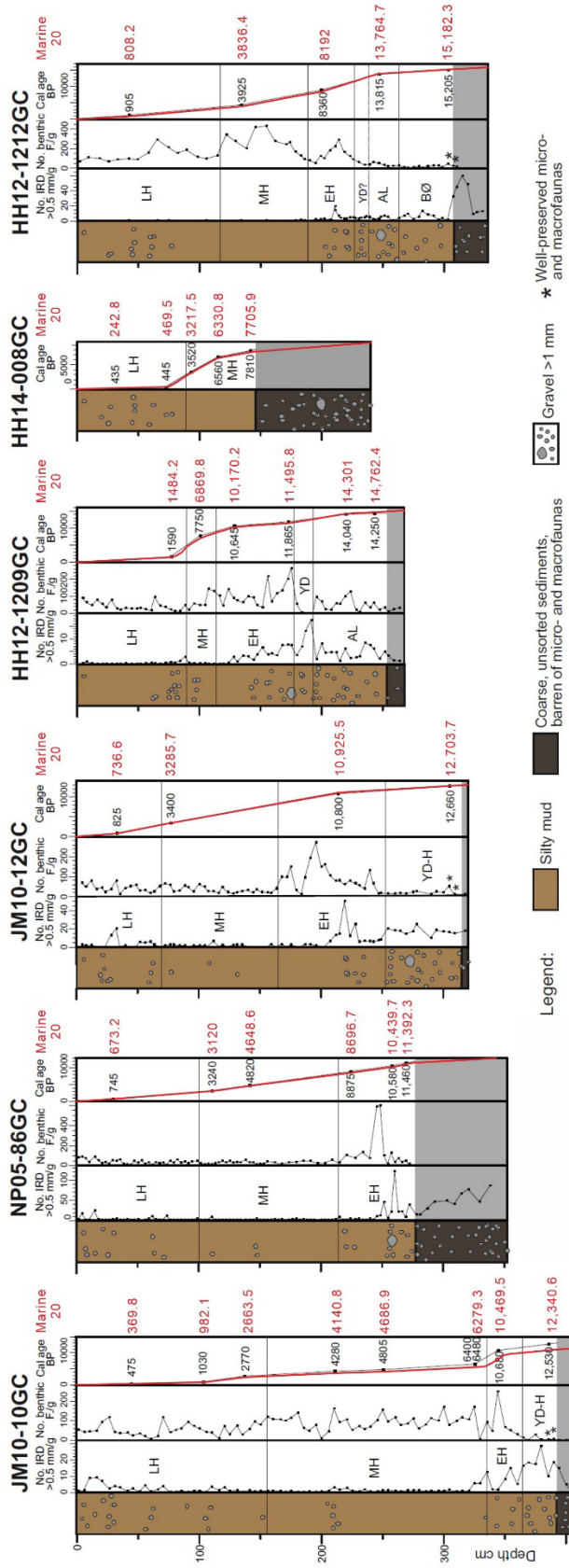


Fig. 2.12. Comparison between the LIA maximum extents suggested by this study and Noormets et al. (2021).

2.6. Conclusions

In this study, we reconstructed glacier-induced depositional environments in Little Storfjorden since YD but also in Hambergbukta. Combined with core-seismic correlation, the occurrence of R2, the NE-SW-oriented grounding zone wedge, indicates the marine-based glaciers/ice streams in Little Storfjorden extended southerly to the vicinity of Hambergbukta during the YD stadial period. Subsequent retreat temporarily stagnated during the YD-Holocene transition compared to eastern Storfjorden. This slow retreat or temporary stagnation indicates the influence of glacial stabilization by the narrow Little Storfjorden and the delayed inflow of warm Atlantic Water. As the Holocene began, the glacier melted out rapidly. In this condition, winnowing by strong bottom currents led to the deposition of a coarser sediment layer in very low sedimentation rates during the late phase of early Holocene to middle Holocene. During the late Holocene, Little Storfjorden was influenced by seasonal sea ice and tidewater glaciers in the coastal areas. However, sediment records indicating noticeable advances (or surges) and retreats of a tidewater glacier in Hambergbukta were identified after approximately 1000 years BP. Based on our results, we suggest that the terminal moraine complex in the fjord mouth of Hambergbukta represents the maximum extent of the LIA Surge.

Supplementary figure 1. Comparison between the previous age model (marine 13) and new age model (marine 20) on the eastern Storfjorden cores (Nilesen and Rasmussen et al. 2018).



CHAPTER 3

Late Quaternary depositional and glacial history of the Arliss Plateau off the East Siberian margin in the western Arctic Ocean

This chapter has been published in Quaternary Science Reviews, 2020. 106099

3.1. Introduction

Over the last two decades, multiple geophysical investigations along with sedimentary records revealed that the Arctic East Siberian and Chukchi continental margins have been repeatedly glaciated during the Pleistocene (Jakobsson et al., 2008, 2014; Polyak et al., 2007; Niessen et al., 2013; Dove et al., 2014; O'Regan et al., 2017). In particular, streamlined glacial lineations and related diamicton deposits identified by swath seafloor and sub-bottom profiling on the East Siberian margin, including the adjacent part of the Mendeleev Ridge known as the Arliss Plateau (AP) (Fig. 3.1C), indicate the repeated development of up to 1 km-thick marine ice sheets/ice shelves (Niessen et al., 2013). However, the age framework for these glacial events, and thus, their relation to a broader paleoclimatic context, is not well understood. Recently, Schreck et al. (2018) provided lithostratigraphic insight on glacial impacts on the East Siberian margin in the Late Pleistocene, concluding that the last major regional ice grounding occurred during MIS 4 to 3 (60-70 ka). This conclusion differs from the notion that this event was coeval with the deepest glacial erosion on the Lomonosov Ridge in the central Arctic Ocean (Jakobsson et al., 2016; O'Regan et al., 2017), which has been constrained to MIS 6 (Jakobsson et al., 2001).

To better constrain the timing of ice grounding events and their spatial pattern, it is important to link the geophysical records and sediment core stratigraphy. This task requires analyzing representative sedimentary records accompanied by sub-bottom seismic profiles and detailed multibeam bathymetry from the areas affected by glaciations. However, most areas of continental margins as well as bathymetric highs on the oceanic ridges and plateaus, impacted by glacial erosion or iceberg turbation,

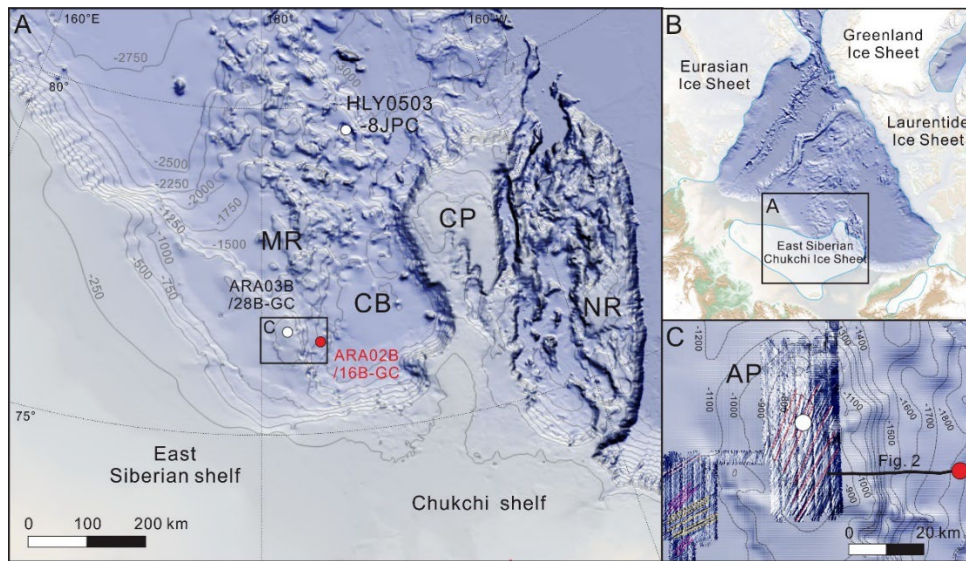


Fig. 3.1. (A) Index physiographic map of the study area showing the location of cores ARA02B/16B-GC (this study), ARA03B/28B-GC (Schreck et al., 2018), and HLY0503-8JPC (Adler et al., 2009). MR, Mendeleev Ridge; AP, Arliss Plateau; CB, Chukchi Basin; CP, Chukchi Plateau; NR, Northwind Ridge. The solid line tracks sub-bottom profiler data. The bathymetric contour interval is 250 m. (B) Broader physiographic/paleogeographic context with inferred ice-sheet maxima shown by semi-transparent white fill (Svendsen et al., 2004; Niessen et al., 2013; Stokes et al., 2016). (C) Multibeam bathymetry of the Arliss Plateau shows several generations of Mega-Scale Glacial Lineations. The bathymetric contour interval is 100 m.

are unsuitable for recovering well-preserved, stratigraphically coherent records (Polyak et al., 2007; Jakobsson et al., 2008; Dove et al., 2014). In comparison, the adjacent slopes and basins may hold more expanded, better-preserved stratigraphies, provided their depositional context, which is sufficiently constrained by geophysical data. In particular, the slope of the AP and the adjacent Chukchi Basin (CB) was chosen for this study as a relatively well-surveyed area of deposition for glaciogenic material originating from the East Siberian continental margin (Niessen et al., 2013; Jakobsson et al., 2014; Schreck et al., 2018). This study uses a sediment core collected on a CHIRP sub-bottom profile (SBP) from the AP top to the CB (Fig. 3.1) to reconstruct the depositional history of the East Siberian margin during and since the last glacial grounding event.

3.2. Regional setting

3.2.1. Seafloor morphology and sedimentary cover

The CB is bounded by the Mendeleev Ridge/AP and the Chukchi Plateau and shelf and is connected to the north with the Canada Basin (Fig. 3.1). The CB covers ~43,000 km² (Jakobsson et al., 2003) and has a relatively flat and smooth seafloor ranging from 1,800 m to 2,300 m water depth, and is comprised of well-stratified deposits (Dove et al., 2014). The tops of both the Arliss and the Chukchi plateaus are covered by streamlined morphological features interpreted as megascale glacial lineations (MSGL), complicated in some areas with transverse ridges (Niessen et al., 2013; Dove et al., 2014; Jakobsson et al., 2014, 2016). The outer parts of the East Siberian and Chukchi margins at water depths to 700 m feature extensive till wedges and recessional moraines related to repeated glacial advances and retreats (Niessen et al., 2013; Dove et al., 2014; Jakobsson et al., 2014). Further downslope these margins as well as adjacent borderlands, including the AP, hold large, lens-shaped debris lobes (Fig. 3.2), similar to seismostratigraphic features observed in the glacial trough mouth fans in front of large ice streams (Batchelor and Dowdeswell, 2014; Jakobsson et al., 2014; O'Regan et al., 2017).

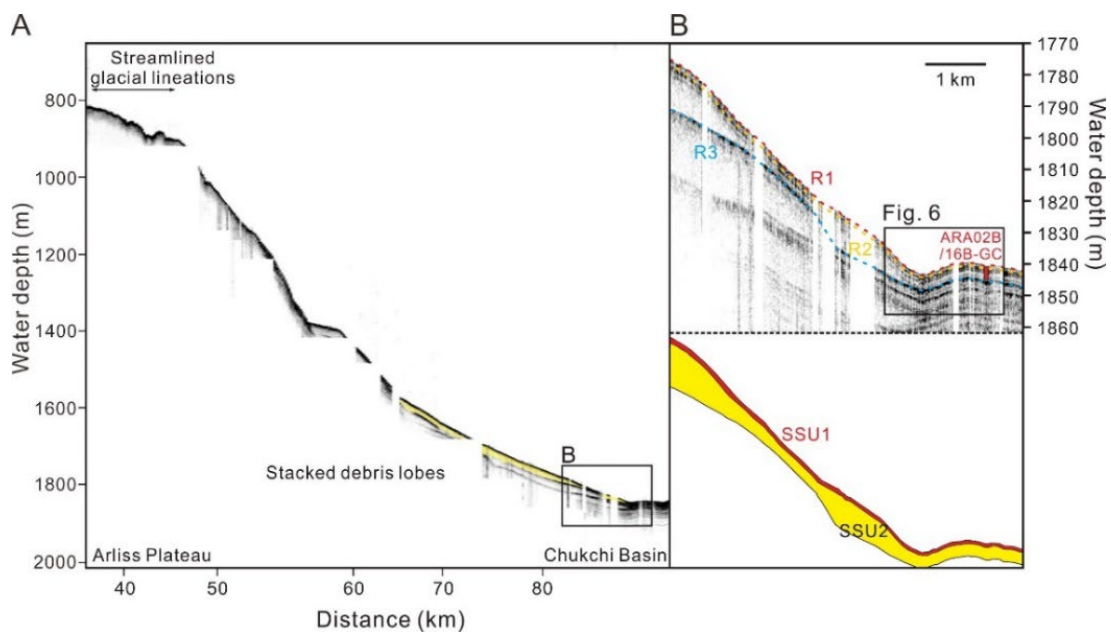


Fig. 3.2. Sub-bottom profiler from Arliss Plateau to Chukchi Basin across the site of core ARA02B/16B-GC (red vertical bar in panel B). Seismostratigraphic units SSU 1 and 2 are bounded by distinct reflectors R1 to 3. The uppermost glaciogenic debris lobes on the slope are correlated with the lower part of SSU 2. The black box shows the position of Fig. 3.6.

3.2.2. Sediment stratigraphy in the western Arctic Ocean

The Quaternary western Arctic sediments are generally characterized by the cyclical pattern of dark brownish and olive/greyish units (Phillips and Grantz, 1997; Polyak et al., 2004, 2009; Adler et al., 2009; Stein et al., 2010; Schreck et al., 2018). This color contrast was shown to be controlled by the content of manganese (Mn) (oxyhydr)oxides, with higher values in brown units attributed to Mn inputs from the continental margins at higher sea levels during interglacial/major interstadial periods (Jakobsson et al., 2000; Polyak et al., 2004, 2009; März et al., 2011; Löwemark et al., 2014; Ye et al., 2019). While Mn-enriched intervals can be affected by diagenetic remobilization and redistribution of this redox-sensitive element, their stratigraphic pattern is consistent throughout the central Arctic Ocean (März et al., 2011; Löwemark et al., 2014; Schreck et al., 2018). Their correlation is corroborated in multiple cores

by the distribution of other lithostratigraphic parameters, such as sediment density, ice-rafted debris (IRD), and biogenic proxies. The brown, Mn-enriched units (layers), interpreted as interglacial/major interstadial sedimentary intervals, are typically characterized also by low to moderate amounts of coarse IRD, intense bioturbation, and relatively abundant microfossils (Polyak et al., 2004, 2009; Adler et al., 2009; Stein et al., 2010; Löwemark et al., 2012). In comparison, olive/greyish, Mn-depleted units, related to glacial periods, are composed of fossil-poor sediments with strongly variable IRD amounts (Polyak et al., 2004, 2009; Adler et al., 2009; Stein et al., 2010). Fine-grained and IRD-rich lithological types of grey sediments have been attributed to glacial maxima and deglacial depositional environments, respectively. At sites proximal to glaciated areas, deglacial sediments may have expanded thicknesses indicative of high depositional rates (Polyak et al., 2007; Wang et al., 2013; Schreck et al., 2018). Some of the IRD peaks have characteristic sediment compositions used as provenance indicators. In particular, detrital carbonates (mostly dolomites) are related to the Paleozoic platform of the Canadian Arctic eroded by the Laurentide Ice Sheet (LIS) (Bischof and Darby, 1997; England et al., 2009; Polyak et al., 2009; Stein et al., 2010; Bazhenova et al., 2017; Dong et al., 2017). Peaks of this material forming characteristic pinkish-white (PW) layers in sediment cores (Clark et al., 1980) can be used to track the distribution of icebergs in the Arctic Ocean during the LIS collapse events.

3.3. Materials and methods

3.3.1. Materials

This study uses a 378-cm-long, 12-cm in diameter gravity sediment core ARA02B/16B-GC (hereafter 16B-GC) and high frequency (2.5-6.5 kHz) sub-bottom CHIRP profiler data collected on the AP slope (Fig. 3.1) during the 2nd RV *Araon* Arctic Expedition (ARA02B) in 2011. Multibeam bathymetry mapping of the AP top (Fig. 3.1C) was subsequently conducted in 2012 (ARA03B). The 16B-GC coring site (76° 24' N, 175° 58' W, 1841 m water depth (mwd)) was selected based on the AWI Parasound data acquired previously on the 2008 RV *Polarstern* Arctic expedition ARK-24/3 (Jokat, 2008). The site is located ~1 km downslope from the foot of glaciogenic debris lobes and features a relatively flat and smooth seafloor with acoustically well-stratified sub-bottom reflectors (Fig. 3.2). A 38-cm-long box core 16B-BC was taken at the same site to recover the surficial sediment. Based on the comparison with 16B-BC, about 10 cm of top sediment is lost in 16B-GC, including the surficial brown lithological unit B1, which was spliced for a composite record of 16B-BC (Figs. 3.3, 3.4).

3.3.2. Methods

After a visual description of the split core, its line-scan images and elemental geochemistry were acquired with an AVAATECH XRF-core scanner at the Korea Institute of Geoscience and Mineral Resources (KIGAM). Line-scanning was conducted using a Jai CV L107 camera with red-green-blue (RGB) channels. L* (lightness) and a* (red-green color space) data were used for correlation with

previously published sediment records (Schreck et al. 2018). Sediment elemental composition was measured at 5-mm intervals using X-ray fluorescence (XRF) AVAATECH scanner settings reported in Schreck et al. (2018). Mn and calcium (Ca) XRF data used in lithostratigraphic correlation were normalized to aluminum (Al) to eliminate the potential dilution effect of background sedimentation (e.g., März et al., 2011). It notes, however, that Mn and Ca variations in Arctic sediments are largely independent of the background lithogenic elements as shown in prior studies (e.g., Löwemark et al., 2014; Dong et al., 2017).

X-radiographs were performed for detailed sediment structure on 1 x 10 x 30 cm slabs. X-ray images were taken with SOFTEX m-100w digital x-ray scanner (EZ-320) and instantly processed using iX-Pect X-Ray imaging software. Darker objects in X-radiographs presented in this study display dense material, such as lithic fragments. Coarse debris >2 mm in diameter was counted at every 1 cm, according to Grobe (1987). Samples for sediment texture were taken at 10 cm intervals and treated with 35% H₂O₂ to decompose organic matter. Sand-sized and coarser grains were separated by wet sieving at 63 µm and dry sieving at 2 mm standard sieves. The grain size of <63-µm sediment was measured with a Micromeritics Sedigraph 5000D.

The multibeam bathymetric survey was performed using a hull-mounted EM122 echosounder. Acquired bathymetric data were processed onboard using the specialized software CARIS. Sub-bottom seismic-reflection data were acquired with the CHIRP SBP-120 profiler with the vertical resolution on the 10 cm scale in acoustically stratified sediments. The SBP data were logged in the TOPAS raw format, which was converted to an SEG-Y format and allowed for post-processing with standard software packages. The estimated sound velocity of 1500 m/s was used to convert the signal

travel time into sediment depth for comparison with core lithostratigraphy.

3.4. Results

3.4.1. Lithostratigraphy

Core 16B is composed of sandy to fine-grained mud displaying a general cyclic depositional pattern characterized by an alternation of brown to dark brown and yellow to olive greyish sedimentary units (Figs. 3.3, 3.4). The concentration of coarse IRD (>2 mm) increases at lithological boundaries and within some brown units, whereas IRD within yellow to olive greyish units is typically rare.

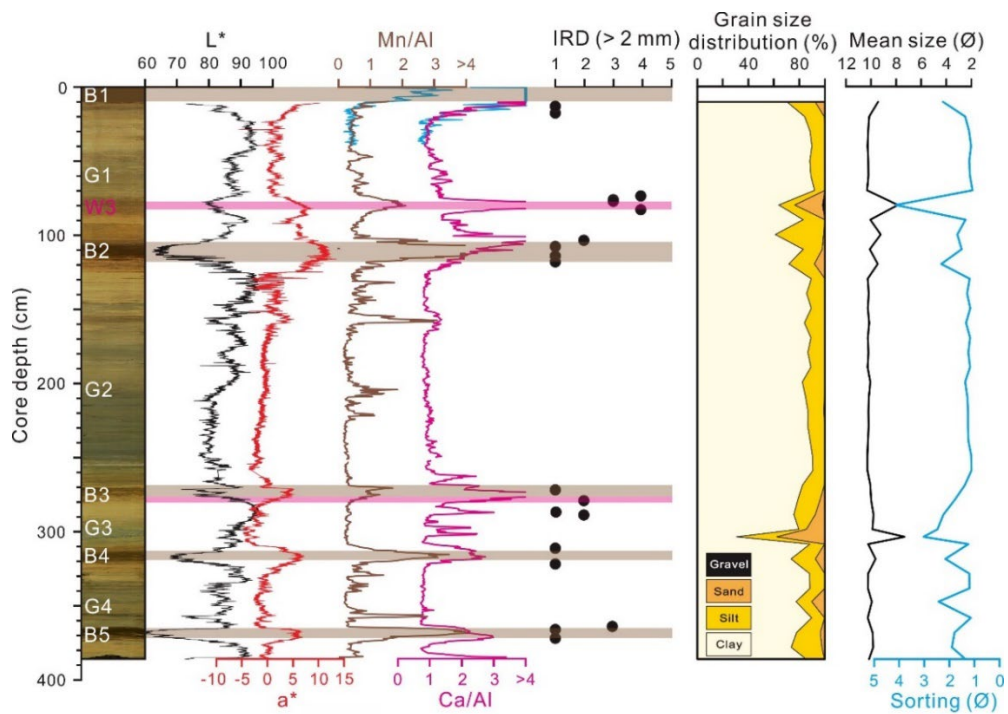


Fig. 3.3. Down-core distribution of sediment lightness (L^*), Mn/Al and Ca/Al ratios, IRD numbers, and grain size in core ARA02B/16B-GC. Top 10 cm are estimated to be missing due to overpenetration; XRF data for this interval (blue-colored solid lines) are spliced from the box core 16B-BC. High Mn/Al and Ca/Al ratios in surficial sediment may be partially due to high water content (Thallingii et al., 2007).

A total of five Mn-rich brown units, B1 to B5, are identified in the recovered stratigraphy based on sediment color, and Mn/Al ratio (Fig. 3.3) along with sedimentary structure and texture (Fig. 3.4), including the upper unit B1 spliced from the box core 16B-BC. The brown units show a characteristic low-L* (darker) and high-a* (more reddish) color pattern with a relatively symmetrical distribution across each unit (Fig. 3.3). High Mn/Al ratios in surficial sediments may be partially due to high water content (Thallingii et al., 2007), but that does not affect the stratigraphic distribution of Mn values, which are high in unit B1. The brown units mostly consist of slightly sandy mud with scattered IRD and have relatively sharp upper boundary and uneven, bioturbated (mottled) lower boundary (Fig. 2.4). Yellowish to olive-grey units are generally thicker than brown units and are mostly composed of fine-grained mud without coarse IRD. In particular, the second grey unit between B2 and B3 is the thickest interval recovered (~150 cm) with a consistent lithology. Two PW carbonate layers, consisting of sandy-gravelly mud and expressed as relatively solid lenses and adjacent scattered speckles, are identified above B2 and at the base of B3, corresponding to prominent Ca/Al peaks (Figs. 3.3, 3.4).

3.4.2. Lithofacies

The sediment record of core 16B was classified into five major lithofacies based on sedimentary structure, texture, and color (Fig. 3.4, Table 3.1): bioturbated sandy mud (Bsm), bioturbated mud (Bm), crudely laminated or layered mud (CLm), thinly laminated mud/muddy sand (TLM/TLs), and homogeneous mud (Hm).

1) Bioturbated sandy mud (Bsm) is mostly identified in brown units and PW carbonaceous layers and is characterized by strong bioturbation overprinting primary sedimentary structures, sharp upper- and uneven, mottled lower-boundaries (Fig. 3.4). This facies mainly consists of very poorly sorted ($2 - 4 \Phi$) sandy mud with coarse particles randomly scattered within the fine matrix (Fig. 3.3). In comparison with the brown units, Bsm in the PW layers contains higher sand content, up to 22% (Fig. 3.3), and more coarse particles. Bioturbated mud (Bm) generally occurs at the transitions between brown and olive-grey units and is characteristic for the olive-grey units underlying B1, where Bm is interbedded with the crudely laminated or layered mud facies (CLm), and below B3 (Fig. 3.4). Similar to Bsm, the Bm facies also has a mottled structure but is composed of more fine-grained muds with gradual facies boundaries. The sediment sorting index in this facies ($1 - 1.5 \Phi$) is lower than in Bsm due to a lack of coarse particles (Figs. 3.3, 3.4).



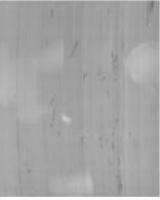

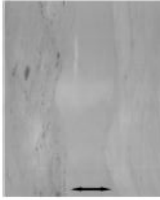
2) Crudely laminated or layered mud (CLm) is characterized by the alternation of planar to sub-parallel silt- and clay-rich laminae or layers with weak bioturbation (Fig. 3.4). Individual laminae are generally difficult to discern. Clayey laminae/layers are mostly thicker ($4 - 12 \text{ mm}$) than their silt-rich counterparts ($1 - 3 \text{ mm}$). Vertical changes in lamina thickness and composition appear to be random, and the sediment is overall weakly sorted ($1 - 1.5 \Phi$). Facies CLm is predominant within the second

olive-grey unit bounded by B2 and B3 and is also interbedded with the Bm facies in the first olive-grey unit.

3) Thinly laminated mud/muddy sand facies (TLm/TLs) can be subdivided into silt-rich mud (TLm) and muddy sand (TLs). This distinct facies has a laterally continuous lamination (a few millimeters thick), typically identified as couplets with overlying homogeneous mud facies Hm (Fig 3.4). TLm/TLs laminae show sharp lower and gradational upper boundaries, and relatively regular thicknesses (Fig. 3.3). TLm/TLs facies occur episodically in the second and third olive-grey intervals, between B2 – B3 and B3 – B4, respectively (Figs. 3.3, 3.4).

4) Homogeneous mud facies (Hm) consists of fine-grained muddy sediment characterized by an overall absence of primary structures, bioturbation, or any grading. This facies is mostly interbedded with the thinly laminated facies TLm/TLs on millimeter scales as couplets. Independently occurring Hm facies (3 cm thick) is identified only in the upper part of the third olive-grey interval below B3 (Fig. 3.4).

Table 3.1. Summary of Lithofacies in core ARA02B/16B-GC. Black arrows indicate the intervals of TLm, TLs, and Hm facies. See Fig. 3.4 for the stratigraphic distribution of lithofacies.

Facies	Description	Depositional process
Bioturbated sandy mud (Bsm)		Brown to dark brown and pinkish; (gravelly) sandy mud, IRD-rich; Hemipelagic settling affected by very poorly sorted; intensely bioturbated, absence of primary structure; relatively sharp and flat upper boundaries and mottled lower basal contact
Bioturbated mud (Bm)		Yellow to olive grey; fine-grained mud, IRD is rare or absent; poorly sorted; located near brown and pinkish layers, repeatedly alternated with poorly defined laminated facies; gradual facies boundaries
Crudely laminated or layered mud (CLm)		Yellow to olive grey; silty mud to clayey mud, IRD is absent; poorly sorted; weakly bioturbated, planar and sub-parallel lamina or layers, lamination is laterally discontinuous and poorly defined, clayey lamina or layer is thicker (4-12 mm) than silty lamina (1-3 mm), non-systematic vertical changes, gradual facies boundaries
Thinly laminated mud/sand (TLm/TLs)		Olive grey; silt-rich mud/sandy mud; IRD is absent; distinct and laterally continuous laminae are coupled with homogenous muds, relatively regular lamina thickness (1-3 mm), sharp lower boundaries and gradational upper boundaries
Homogeneous mud (Hm)		Olive grey; fine-grained mud, IRD is absent; poorly sorted; absence of primary structure as well as any grading and bioturbation; generally coupled with TLm/TLs facies

Black arrows indicate each facies (TLm, TLs, and Hm)

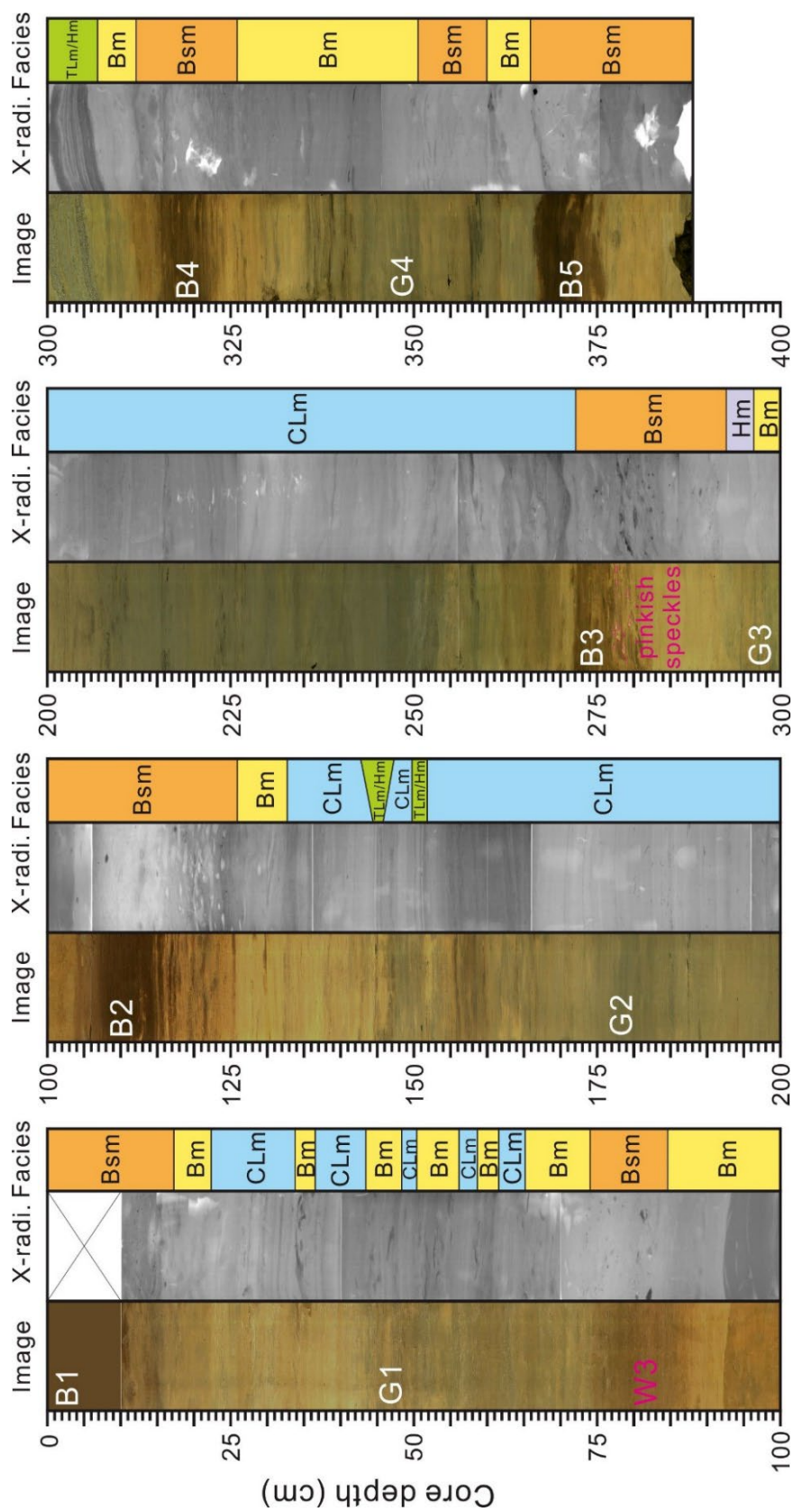


Fig. 3.4. Split-core photos, X-radiograph images, and lithofacies (see Table 3.1 for details). Indices for lithological units (B1-B5 and G1-G4) and the detrital carbonate layer W3 are shown on the core photo.

3.4.3. Geomorphology and seismostratigraphy of the AP basinward slope

The seafloor of the AP top shows several sets of streamlined morphological features (Fig. 3.1C) interpreted in prior studies as megascale glacial lineations (Niessen et al., 2013; Jakobsson et al., 2016). The youngest set of lineations of SSW-NNE orientation is traced to water depths of ~950 m in the southern part of AP, compared to somewhat shallower depths of 850 m in the northern part. The lineated surface is covered by ~3-m thick, acoustically stratified sediment (Niessen et al., 2013). The sub-bottom data from the basin-ward middle to the lower slope of the AP (~1600-1800 mwd) show stacked series of debris lobes of ~10-20 km long and up to 25 m thick (Fig. 3.2A). The debris deposits are covered by acoustically stratified sediments (Figs. 3.2B, 3.2C). Three distinct acoustic reflectors (R1 – R3) were identified by lateral continuity and strong reflectivity. The reflectors divide the upper part of the sediment cover into two major seismostratigraphic units, SSU 1 and 2.

The surficial unit SSU 1 bounded by reflectors R1 (seafloor) and R2 is laterally continuous and has bedding parallel to R2 (Figs 3.2B, C). SSU 1 is characterized by transparent to slightly fuzzy sub-bottom echoes, with a laterally discontinuous, weak reflector also recognized within this unit (Fig. 3.2B). SSU 1 thins out from the core 16B site towards the steep middle slope (Figs. 3.2B, C) and is indistinguishable further up-slope near the AP top.

As seen on records from the basin and lower slope (Fig. 3.2B), the underlying unit SSU 2, bounded by R2 and R3, is generally characterized by parallel lamination with variable amplitudes and transparent acoustic signature in the middle part of the unit. Further up-slope, two coeval debris lobes are recognized in the lower part of SSU 2, covered by acoustically stratified sediment comprised of the remaining part of SSU

2 and overlying SSU 1 (Figs. 3.2B, C). Two thin reflectors with low to moderate reflectivity are identified in the lowermost part of SSU 2 in the basin, but cannot be found near the debris lobes on the upper slope (Fig. 3.2B).

3.5. Discussion

3.5.1. Age model

As core 16B-GC lacks calcareous material for ^{14}C dating, its age model is constrained by lithostratigraphic correlation with the earlier investigated core ARA03B/28B-GC from the AP top (Schreck et al., 2018) and core HLY0503-8JPC from the foot of the Mendeleev Ridge ~350 km north (Adler et al., 2009). The latter core record has the best regional age control constrained by multiple ^{14}C datings in the upper part of the stratigraphy (MIS 1 to 3, units B1-B3), ^{14}C -calibrated amino-acid racemization (AAR) rates extending to MIS 5 (Kaufman et al., 2008; Adler et al., 2009), and coccolith occurrences (Backman et al., 2009). The correlation is primarily based on sediment color and distribution of Mn and Ca content showing a regionally consistent pattern (Fig. 3.5) (Polyak et al., 2009; Stein et al., 2010; Schreck et al., 2018). According to ^{14}C dating, brown, Mn-rich units B1 and B2, including the detrital carbonate layer W3, represent MIS 1 (~ 9 ka) and MIS 3 (34-45 ka) interglacial/interstadial environments, respectively (Fig. 3.5; Table 3.2). The intermittent grey unit G1 thus corresponds to the last glaciation/deglaciation (MIS 2 to 1) and the youngest, pre-glacial part of MIS 3.

Brown units B3 to B5 recovered by core 16B-GC have been attributed in the reference cores to pre-MIS 3 interstadials ranging to MIS 5c, with some variance.

Based on coccolith distribution in HLY0503-8JPC, Backman et al. (2009) suggested that B5 represents MIS 5a, while Adler et al. (2009) assigned its age to MIS 5c, consistent with AAR ages (Kaufman et al., 2008). This age model was also used by Schreck et al. (2018), who pointed out that the coccolith stratigraphy cannot pinpoint a specific time interval within MIS 5. In any case, core 16B-GC does not reach the prominent detrital carbonate layer PW2 identified in multiple cores across the western Arctic Ocean, including HLY0503-8JPC (Fig. 3.5), and attributed to MIS 5d (e.g., Stein et al., 2010; Bazhenova et al., 2017; Dong et al., 2017). Overall, we consider MIS 5c, with the approximate age of ca. 100 ka, as a reasonable estimate for the bottom of 16B-GC.

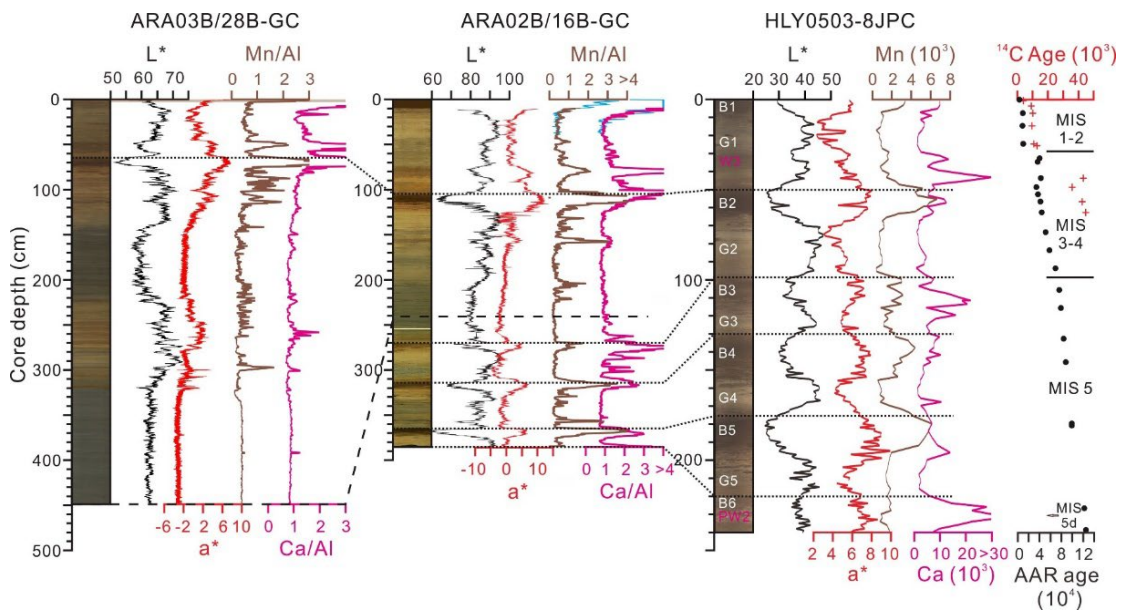


Fig. 3.5. Lithostratigraphic correlation of core ARA02B/16B-GC with ARA03B/28B-GC (Schreck et al., 2018) and HLY0503-8JPC (Adler et al., 2009) based on sediment color and variations of Mn/Al and Ca/Al. The tops of major brown units (B2-B5) are correlated by dotted lines; the bottom of core ARA03B/28B-GC is projected onto ARA02B/16B-GC by the dashed line. Estimated Marine Isotope Stages and radiocarbon/AAR ages (Adler et al., 2009) are shown next to core HLY0503-8JPC.

Table 3.2. Estimated duration and sedimentation rates of lithostratigraphic units in core ARA02B/16B-GC based on the age model developed from lithostratigraphic correlations (Fig. 3.5).

Lithostratigraphy	Thickness (cm)	Duration (kyr)	Sedi. Rate (cm/kyr)
B1	10 (0-10)	9 (0-9)	0.83
G1	68 (10-78)	25 (9-34)	2.72
W3-B2	37 (78-115)	11 (34-45)	3.36
G2	157 (115-272)	26 (45-71)	6.04
B3-B5	104 (272-375)	25 (71-96)	4.12

The developed lithostratigraphic framework indicates that a ~150-cm thick grey unit G2 pre-dates the MIS 3 interstadial, likely being contained in the time interval from MIS 4 to early MIS 3. This prominent lithostratigraphic unit can be traced in multiple cores from the Siberian margin to the Arctic Ocean interior (e.g., Spielhagen et al., 2004; Polyak et al., 2009; Dong et al., 2017; Wang et al., 2018), and has been proposed to correlate to the last pre-LGM glaciation in northern Eurasia with a glacial maximum around 50-60 ka (Svendsen et al., 2004).

In comparison to this, regionally consistent age model, the B2 unit in a very similar nearby record was assigned to MIS 5 based solely on the presence of rare coccoliths, including *E. huxleyi* (SWERUS-L2-13PC; <https://bolin.su.se/data/swerus/physical.php>; Fig. 3.1) (Jakobsson et al., 2016). The occurrence of *E. huxleyi* clearly indicates that the sediments of this unit are younger than MIS 8/7 (Thiersten et al., 1977; Backman et al., 2009). However, due to an overall limited occurrence of coccoliths, *E. huxleyi* presence may not be used to identify specific substages within MIS 5 as attempted previously (e.g., Jakobsson et al., 2001; Spielhagen et al., 2004) because this species can potentially occur in other relatively warm intervals of Arctic sediments. In particular, MIS 3 is a very pronounced interstadial unit in Arctic paleoceanographic records, as exemplified by a high content of Mn and high

productivity indicated by abundant planktic and benthic microfossils (Nørgaard-Pedersen et al., 1998; Adler et al., 2009; Hanslik et al., 2010; Schreck et al., 2018). Some authors further inferred reduced sea ice and enhanced the advection of Atlantic waters during this time (Cronin et al., 2012; Poirier et al., 2012). We note that in another SWERUS core from the Siberian margin further west, *E. huxleyi* was also found in B2 with a ^{14}C age of 33 ka just a little above this finding (O'Regan et al., 2017).

3.5.2. Core-seismic correlation

Distinct acoustic reflectors on seismic records can be formed by vertical changes in acoustic impedance controlled by sediment density and p-wave velocity. Deep-sea Arctic Ocean sediments generally consist of relatively soft fine-grained muds, which are occasionally intercalated with denser, coarse sediment layers mostly attributed to iceberg sedimentation during deglacial events (Clark et al., 1980; Polyak et al., 2009; Stein et al., 2010; Dong et al., 2017; Schreck et al., 2018). In particular, detrital carbonate IRD layers, such as W3 and PW2 captured by western Arctic Ocean sediments, are characterized in cores from the study region by a remarkably high density and p-wave velocity compared to the enclosing fine-grained muds (Matthiessen et al., 2010; Stein et al., 2010; Schreck et al., 2018). These layers, marking the LIS iceberg discharge from the Canadian Arctic, thus have the potential to form strong reflectors.

A comparison of the sub-bottom acoustic reflection data and core 16B record (Fig. 3.6) confirms that the surficial reflector R1 represents the seafloor, the interface between bottom water and relatively dense surficial sediments of unit B1. Fine-grained

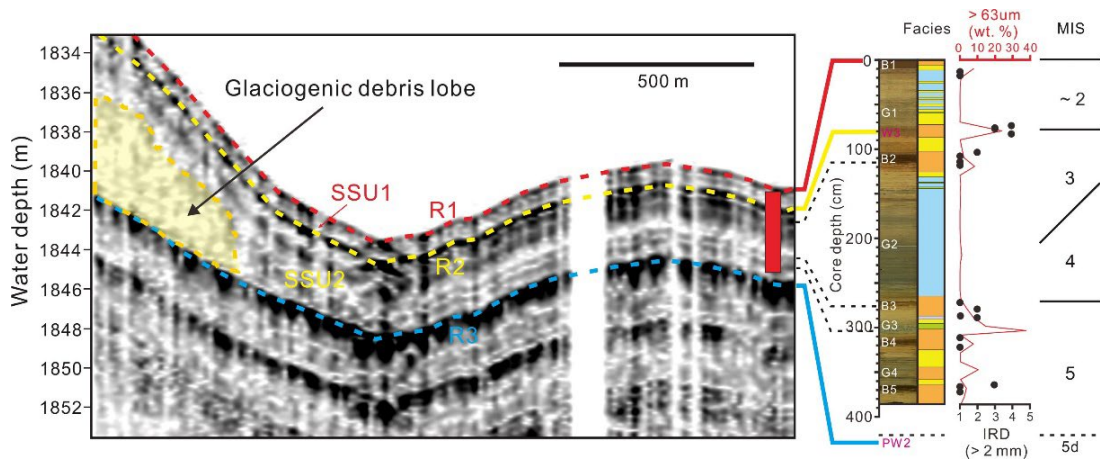


Fig. 3.6. Correlation of the sub-bottom data with core ARA02B/16B-GC. Surficial reflector R1 is the seafloor. Strong reflectors R2 and R3 correspond to prominent lithological changes at the boundaries of fine-grained sediments and IRD-rich layers W3 and PW2. Estimated marine isotope stages are shown on the right.

unit G1 characterized by a relatively constant density and p-wave velocity in multiple records from the study region (Matthiessen et al., 2010; Stein et al., 2010; Schreck et al., 2018) defines a mostly transparent echo characteristic of SSU 1. A strong reflector R2 probably indicates a pronounced lithological change from the IRD-rich interval, including the W3 layer to the overlying fine-grained unit G1 (Fig. 3.6). A relatively strong reflector in the uppermost part of SSU 2, partially divided into two layers, appears to be associated with a relatively coarse unit B2 (Fig. 3.6). A transparent echo signature similar to that in SSU 1 characterizes the upper part of SSU 2 corresponding to the fine-grained, thickest unit G2. Two thin reflectors of low to moderate amplitude in the lower part of SSU 2 appear to correspond to a relatively sandy unit B3, especially its detrital carbonate-rich base layer, and an intermittent sandy layer within G3 (Fig. 3.6). While core 16B-GC does not extend to the depth of R3, a likely candidate for this strong reflector is a prominent, IRD-rich, detrital carbonate layer PW2 that underlies unit B6 and is barely reached by 16B-GC (Fig. 3.5). PW2 is characterized by a significantly higher wet bulk density and p-wave velocity than other Upper Quaternary

sediments in the study region (Matthiessen et al., 2010; Schreck et al., 2018).

3.5.3. Glaciogenic debris lobes on the AP slope

The presence of debris lobes in the lower part of SSU 2 up-slope from core 16B (Fig. 3.2) is likely related to glacial scouring on the AP crest. While debris flows can potentially originate from various slope instability processes, the consistent occurrence of these lobes in the Arctic Ocean downslope from continental margins and plateaus characterized by glacial erosion/deposition indicates their glaciogenic origin. In particular, the CB features debris lobes on both the AP and Chukchi Plateau slopes (Niessen et al., 2013; Dove et al., 2014 and reference therein), indicating glaciogenic inputs from both sides. The mechanisms for debris flows could include sediment bulldozing on the tops by grounded ice and/or rapid deposition of deglacial sediments, e.g., from glacial underflows (e.g., Powell, 1990; Batchelor and Dowdeswell, 2015). The timing of debris lobe emplacement would thus correspond to glacial advance or early deglaciation stages.

The SSW-NNE orientation and southward inclination of the youngest set of glacial lineations on the AP top indicate that the eroding ice was sourced from the East Siberian margin (Niessen et al., 2013). According to the age constraints developed for core 16B-GC and a correlative core 28B-GC from the AP top (Fig. 3.5), this event occurred before the MIS 3 interstadial and was possibly related to a major glaciation in northern Siberia dated to the time interval between ~70 and 50 ka (Svendsen et al., 2004; Möller et al., 2015).

3.5.4. Glacier-induced depositional environments

Based on the developed age model, sedimentary unit G2 (MIS 4 to early MIS 3) that is characterized by laminated mud facies, has a relatively high sedimentation rate of ~6 cm/kyr as compared to more bioturbated units G3 and G4 (Fig. 3.4, Table 3.2). Laminated structures of glaciogenic sediments in the high-latitude oceans can be potentially formed under various depositional settings such as permanent sea ice, turbid meltwater plumes, distal fine-grained turbidity currents, and contour currents (Hesse et al., 1996; Darby et al., 1997; Kleiber et al., 2000; ÓCofaigh et al., 2003; Matthiessen et al., 2010). However, contour currents are unlikely to be strong in a semi-enclosed Arctic deep-sea basin, while sedimentation rates under perennial sea ice are too low to form a laminated sedimentary sequence. Couplets of TLm/TLs and Hm facies similar to those observed in 16B-GC (Fig. 3.4) have been interpreted in previous studies as deposition from underflow turbidity currents in combination with rapid settling from fine-grained suspension plumes in the attenuation stage of the carrying current (Piper, 1978; Chough, 1984; Yoon et al., 1991). The occurrence of TLm/TLs facies within G2 and G3 suggests that turbidities could be associated with the glaciogenic debris flows emanating from their front on a relatively steep AP slope (Fig. 3.2B). The development of CLm facies may reflect deposition from turbid meltwater plumes repeatedly discharged from ice-sheet termini (Hesse et al., 1996; Kleiber et al., 2000; ÓCofaigh et al., 2003).

Glacial erosion on glaciated continental margins plays an important role in delivering large amounts of sediments to the continental slope and the adjacent basins, thus leading to the formation of debris flows (Vorren et al., 1998; Kleiber et al., 2000; Dowdeswell and Elverhøi, 2002; Jakobsson et al., 2008). Based on our

seismostratigraphic and sediment core data, this scenario applies to the AP during MIS 4, when large volumes of eroded sediment may have been transported as proglacial under- and overflows into the adjacent deep basin. This rapid sediment deposition likely caused slope instability and thus triggered debris flows. Suspended fine sediments could have been detached from the slope and transported into the interior of the Arctic Ocean at the density boundaries between different water masses with subsequent deposition. Prolonged glacial erosion could have also formed repeatedly detached turbid layers, leading to the formation of crudely laminated mud (CLm) facies (Fig. 3.7A). As the grounded ice retreated, turbid meltwater underflow plumes were likely repeatedly discharged from the grounding line, thereby depositing CLm facies (Hesse et al., 1996; ÓCofaigh et al., 2003) (Fig. 3.7B). These glacier-induced processes could lead to the deposition of fine-grained, fully laminated sediments with fairly high sedimentation rates (unit G2) during the MIS 4 deglaciation that may have extended to early MIS 3.

Bioturbated sediments of B2 and the overlying W3 layer are interpreted to represent hemipelagic depositional environments with drifting icebergs during a relatively warm period of MIS 3 (Fig. 3.7C). In general, Mn-enriched, brown sediments are believed to reflect elevated sea levels and/or reduced sea-ice conditions, under which sediment from the Siberian shelves could be transported to the central Arctic basins (Jakobsson et al., 2000; Polyak et al., 2004, 2009; Stein et al., 2010; Löwemark et al., 2014; Ye et al., 2019). Overall, sedimentary properties of G2 and overlying facies indicate depositional environments affected by the advance and retreat of a marine-based ice sheet grounded on the AP top.

The absence of glaciogenic debris lobe within SSU 1 indicates that the AP has

not encountered glacial erosion during MIS 2, consistent with previous studies from the Arctic Ocean off the Siberian margin (Niessen et al., 2013; Schreck et al., 2018) as well as terrestrial studies from adjacent islands and the East Siberian mainland (Romanovskii et al., 2004; Gualtieri et al., 2005). Nevertheless, the presence of CLm facies within unit G1, most of which is attributed to MIS 2 (Figs. 3.3, 3.4), reflects glacier-induced depositional processes, such as the suspension settling of turbid meltwater plumes and detached turbid layers (Figs 3.7D, E). This lithology indicates the influence of a limited glaciation in the study region, although its location and distribution pattern (e.g., grounded ice vs. ice shelf) needs to be further investigated. There is no evidence for the LGM glaciation at the East Siberian margin, but data from the eastern Chukchi shelf margin show glaciogenic bedforms indicative of grounded ice, age-constrained to MIS 2 (Polyak et al., 2007). These bedforms are restricted to water depths of less than ~450 m, but we cannot exclude that this grounded ice extended over the Chukchi shelf to its western margin bordering the Chukchi Basin.

The predominance of the bioturbated sandy mud (Bsm) facies in the uppermost unit B1 reflects hemipelagic deposition with sea-ice and/or iceberg debris rafting during much of the Holocene (Fig. 3.7F). Intense bioturbation indicates a relatively elevated export of primary production to the seafloor, and thus moderate sea-ice conditions, and/or enhanced oxygenation of surface sediments.

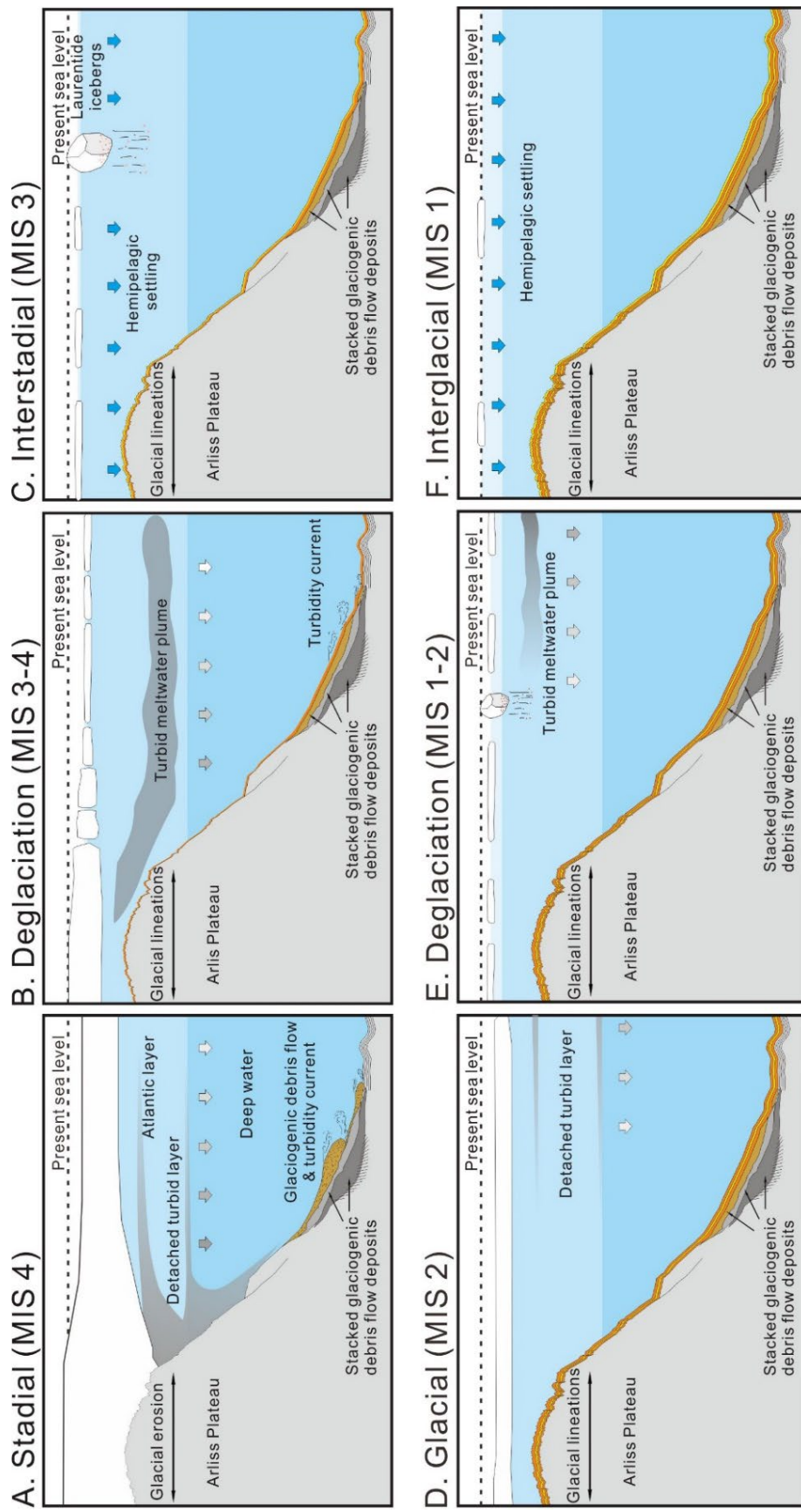


Fig. 3.7. Schematic model of sedimentary processes on the Arliss Plateau and adjacent Chukchi Basin during major depositional regimes from the MIS 4 glaciation to the Holocene.

3.6. Conclusions

A combination of litho- and seismostratigraphy on the basinward slope of the Arliss Plateau depicts a glacier-induced depositional history in front of the East Siberian continental margin since estimated MIS 5c (~100 ka). The age constraints were obtained by correlation of the studied core ARA02B/16B-GC with earlier developed stratigraphies (Adler et al., 2009; Schreck et al., 2018). Based on this age model and the core-seismic correlation, deposition of the youngest glaciogenic debris lobes on the slope, indicative of the last glacial erosion of the AP top, occurred within seismostratigraphic unit SSU 2 during MIS 4 to early MIS 3. This event may be correlative to a major glaciation in northern Siberia that has been constrained to the time interval between ~70 and 50 ka (Svendsen et al., 2004; Möller et al., 2015). Laminated lithofacies and sedimentation rates as high as ~6 cm/kyr in the respective core interval (lithological unit G2) reflect glacier-induced sediment deposition. This enhanced sedimentation probably resulted from detached turbid layers, turbidity currents, and meltwater discharge pulses during glaciation/deglaciation. The absence of glaciogenic debris lobes within the upper seismostratigraphic unit SSU 1 (late MIS 3 to 1) indicates that glacial erosion unlikely impacted the AP during the LGM, consistent with previous inferences (Niessen et al., 2013; Schreck et al., 2018). Nevertheless, the presence of laminated facies within the corresponding core interval G1 may indicate a limited glaciation at a nearby continental margin.

CHAPTER 4

The repeated occurrences of a km-thick East Siberian marine ice sheet (ESIS) over the last 300 ka

This chapter was prepared for submission to Frontiers in Marine Science

4.1. Introduction

In the early 2000s, East Siberian and Chukchi margins were considered to be glacier-free during the Late Quaternary (Alekseev, 1997; Ehler and Gibbard, 2007; Stauch and Gualtieri, 2008; Hu et al., 2010). However, morphological evidence in these areas has corroborated the occurrence of marine-based glaciers over the last two decades (Jakobsson et al., 2014 and references therein). The accumulation of geophysical data (submarine landforms and seismic data) on these areas corroborated that the East Siberian and Chukchi margins had been affected by a km-thick marine-based glacier, several hundred meters-thick ice caps (possibly sourced from Chukchi shelf) and/or ice shelves (extended from Laurentide Ice Sheet, LIS) on both regions during the Late Quaternary glacial periods (Fig. 4.1A) (Polyak et al., 2007; Jakobsson et al., 2008; Niessen et al., 2013; Dove et al., 2014; O'Regan et al., 2017; Kim et al., 2021). Notably, the occurrences of the East Siberian marine ice sheet (ESIS) can potentially affect eustatic sea-level changes as an additional glacier source.

Despite the importance of ESIS to a better understanding of the Arctic ice conditions and climate changes, its time constraints were roughly postulated as the Pleistocene glaciations before the Last Glacial Maximum (LGM) (Niessen et al., 2013). The last occurrence of the huge ESIS that eroded the crest of the Arliss Plateau was recently constrained to the marine isotope stage (MIS) 4, and the attendant depositional environments and glacial history were reconstructed in the Arliss Plateau and Chukchi Basin-ward slope (e.g., Joe et al., 2020). However, the longer-term glacial history is still poorly understood. This study shows multi-beam bathymetry, high-resolution sub-bottom profiles, and lithostratigraphy in the Chukchi Basin and its outside slopes to

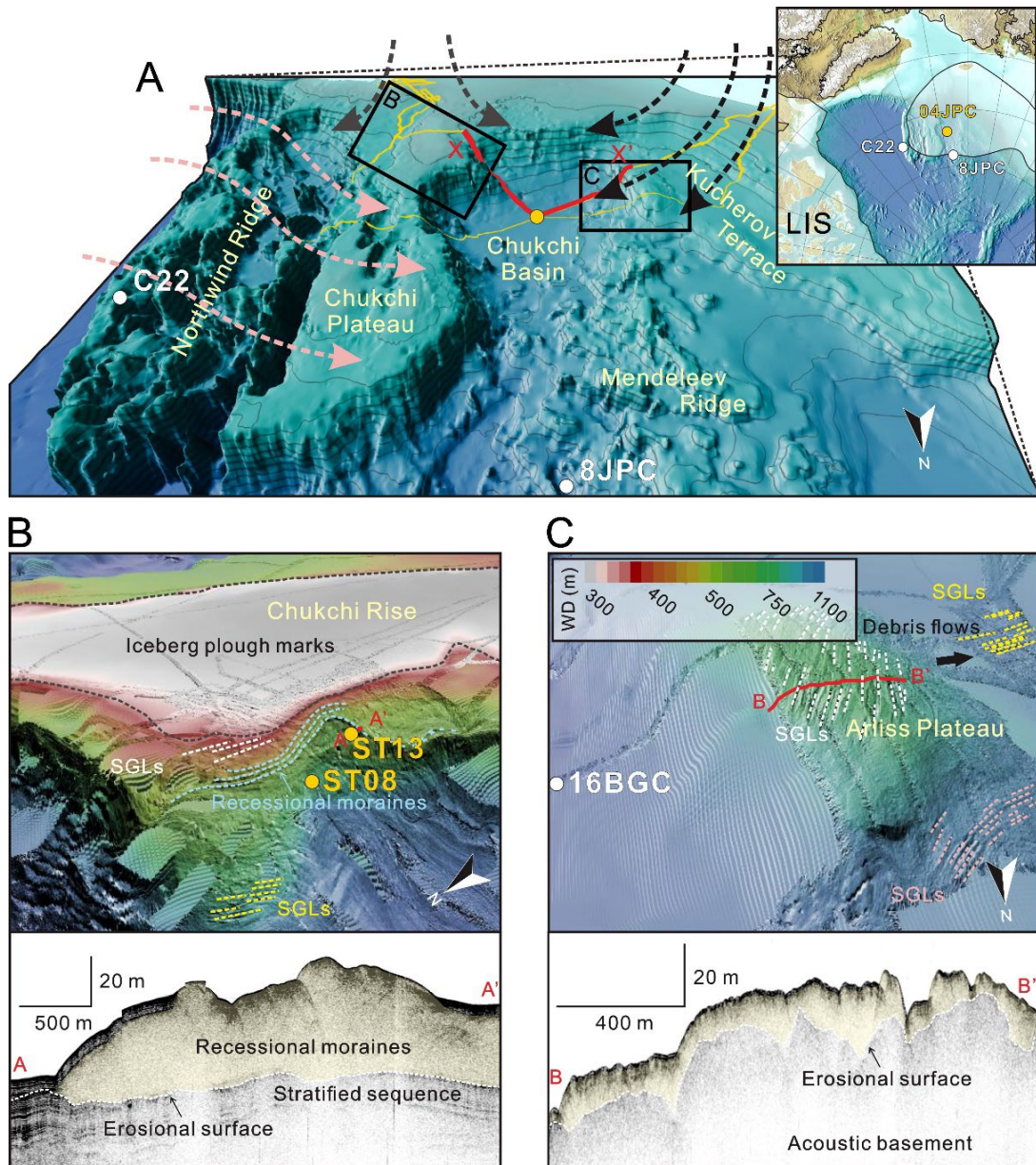


Fig. 4.1. (A) Bathymetry of the East Siberian and Chukchi margins. Three arrows indicate estimated ice flow directions by the Laurentide Ice Sheet (pink) and East Siberian and Chukchi Seas Ice Sheet (grey and black). The Yellow line shows the SBP track line during the ARA06C cruise. For the X-X' cross-section (red line), the SBP profile is shown in Fig 4.2. In the upper right panel, the maximum extent of the Late Quaternary Arctic ice sheets was mapped using the MIS 12 maximum model from Batchelor et al. (2019). (B) Streamlined glacial lineations (SGLs) and recessional moraines on the western Chukchi Rise were defined by Kim et al. (2020). (C) Several sets of SGLs and debris lobes on the Arliss Plateau and adjacent area were introduced by Niessen et al. (2013). Yellow and white circles indicate the locations of the studied and referenced cores (Table 4.1).

reconstruct longer-term glacial history on the East Siberian and further Chukchi margins. Notably, a ~14 m-long piston core (ARA06C/04JPC) obtained from the Chukchi Basin interior preserves the high-resolution glacial sediment records. Combined with morphological data, the glacial records provide geological evidence for the additional occurrences of the ESIS during MISs 6 and 8.

4.2. Study area: Chukchi Basin

The Chukchi Basin is surrounded by the East Siberian and Chukchi margins in the western Arctic Ocean (Fig. 4.1A). In a prominent flat platform (Kuchеров Terrace) northerly extending from the East Siberian shelf, the Arliss Plateau and adjacent slopes are characterized by several sets (NE-SW, NEE-SWW) of streamlined glacial lineations (SGLs) at water depths of ~950 m and 1,200 m (Niessen et al., 2013). These lineations are partly covered by glacial debris lobes (Fig. 4.1C). On the western Chukchi Rise (Fig. 4.1B), contour-parallel morainic ridges at 400-630 m water depths and two sets (N-S and NNW-SSE) of SGLs at different water depths (380-410 m and 780-940 m) indicate repetition of ice-grounding events on this area (Kim et al., 2021). Across the shelf edges of the East Siberian and Chukchi margins, the marine Neogene deposits on the outer shelves and upper slopes are truncated by glacial sedimentary units on the preglacial strata (Niessen et al., 2013; Dove et al., 2014). Notably, on the middle to lower slopes, several stacked debris lobes indicate that numerous sediments had been transported toward the Chukchi Basin due to the growth and retreat of marine-based glaciers or ice sheets on the continental shelves during the Late Quaternary (Dove et al., 2014; Joe et al., 2020; Kim et al., 2021).

Including sub-glacial tills on the bathymetric highs, debris lobes on the slopes, and thick and well-stratified glacial sediments, the glacial deposits suggested that the last glacial erosion on the Arliss Plateau may have occurred during MIS 4 to early MIS 3 (Schreck et al., 2018; Joe et al., 2020), possibly consistent with a major glaciation in northern Siberia between ~70 and 50 ka (e.g., Svendsen et al., 2004; Möller et al., 2015). However, the older glaciations are more speculative (Niessen et al., 2013). Despite extensive and complex ice configurations based on glacialigenic submarine landforms (Jakobsson et al., 2014 and references therein), the attempt to constrain their formation on the Chukchi Borderland is quite lacking. At the southernmost part of the Northwind Ridge, at least two episodes of NE-SW-trending glacial erosions have been recognized at different depths to ~450 m and 750 m (Polyak et al., 2007), indicative of ice flows from the Laurentide Ice Sheet. Based on the sediment stratigraphy in these areas, the different diamicton horizons were formed during the last glacial maximum (LGM) and an earlier glacial event, possibly MIS 4 or 5d (Polyak et al., 2007).

4.3. Materials and methods

4.3.1. Materials

Detailed bathymetric mapping on the Arliss Plateau and western Chukchi Rise was introduced by Niessen et al. (2013) and Kim et al. (2021) using the multi-beam echo sounding (MBES) data during several Arctic expeditions (ARK-XXIII/3 and ARA03B-ARA10C) with the RV *Polarstern* in 2008 and RV *Araon* in 2012-2019. During the *Araon* cruises, seismic data were collected by high-resolution CHIRP sub-bottom profiling (SBP) with a frequency range of 2.5-7.0 kHz. To define

seismostratigraphy in the Chukchi Basin and adjacent slopes, the SBP data acquired during ARA06C and ARA09C cruises are analyzed, and three sediment cores were used in this study (Table 4.1). A ~14 m-long jumbo piston core ARA06C/04JPC (hereafter 04JPC) was obtained from the Chukchi Basin (Fig. 4.1A). Two short gravity cores ARA09C/ST13-GC and ARA09C/ST08-GC (hereafter, ST13 and ST08) were collected on the adjacent area in front of the recessional moraine on the western shelf-break of Chukchi Rise (Fig. 4.1B).

Table 4.1. Information of studied and referenced cores.

Site	Abbr.	Lati. (°N)	Long (°E)	WD (m)	Reference
ARA06C/04-JPC	04JPC	76.43	-172.68	2292	This study
ARA09C/ST08-GC	ST08	75.85	-169.85	813	This study
ARA09C/ST13-GC	ST13	75.67	-169.74	624	This study
ARA02B/16B-GC	16BGC	76.40	-175.97	1841	Joe et al. (2020)
HLY0503-8JPC	8JPC	79.59	-172.50	2729	Adler et al. (2009)
ARC6-C22	C22	77.19	-154.59	1025	Wang et al. (2021)

4.3.2. Methods

To understand the longer-term glacial history of the western Arctic Ocean, multiple lithological parameters were measured on core 04JPC. The parameters include physical property, core surface images, color index, elemental composition, grain size, sedimentary structure, bulk mineralogy, and geomagnetic data. I) Physical properties, including wet bulk density (WBD), p-wave velocity (V_p), and magnetic susceptibility (MS), were measured at 1 cm intervals on the whole core sections on board with a multi-sensor-core-logger. II) Measurements of high-resolution core surface images, color index, and elemental geochemistry were performed on split half sections of core 04JPC after splitting using AVAATECH XRF core scanner, which was equipped with rhodium X-ray source and a Canberra X-PIPS Detector SXD15C-150-

500 (resolution > 190 eV) at the Korea Institute for Geoscience and Mineral Resources (KIGAM). More details were described in Schreck et al. (2018). III) The grain size was analyzed on ~130 mg of freeze-dried samples, treated with 35% H₂O₂ for 24 h to decompose organic matter. After rinsing with distilled water, sediment samples were separated by wet sieving with a 1 mm standard sieve. The sediment samples were treated with an ultrasonic vibrator to facilitate particle disaggregation before analysis. Grain size analysis was performed with a Malvern Mastersizer 2000 laser diffraction particle size analyzer at the KIGAM. Coarse grains (> 1 mm in diameter) were counted in x-radiographs. IV) X-radiographs were collected for detailed sediment texture and structure on 1×10×30 cm slabs with SOFTEX m-100w distal x-ray scanner (EZ-320). Denser materials such as lithic fragments are identified as darker objects in x-radiographs. V) Bulk mineral composition was performed with a Philips X'Pert Pro multipurpose diffractometer equipped with a Cu-tube and monochromator at Bremen University. Dried bulk samples were grounded to a fine powder (<20 μm particle size) and prepared with the Philips backloading system. Measurement settings were introduced in Vogt (2009). Semi-quantification of mineral contents was conducted using the QUAX full-pattern analysis software (cf. Vogt et al., 2002). VI) To obtain downcore variations in paleomagnetic inclination, sediments were additionally subsampled with ~7 cm³ cubes at ~2.3 cm intervals (n=589). The paleomagnetic analysis was performed by Dr. Thomas Frederichs at Bremen University. Natural remanent magnetization (NRM) was measured on a three-axis superconducting rock magnetometer (2G Enterprises model 755 HR) after a systematic demagnetization treatment involving 15 steps for each sample applying 5 mT increments up to an alternating field of 50 mT and 10 mT increments in alternating fields between 60 and

100 mT. To determine the characteristic remanent magnetization (ChRM), vector analysis was applied to the results of Kirschvink (1980). VII) AMS ^{14}C age dating was performed at the Isotope Ecology and Environmental Science Laboratory of Alfred-Wegener-Institute (AWI) using planktic foraminifera *Neogloboquadrina pachyderma* sinistral. Calendar years were calculated using 800 and 1400 years as carbon reservoir correction for the Holocene and MIS 3, respectively (Coulthard et al., 2010; Hanslik et al., 2010).

Three measurements were conducted for two cores ST13 and ST08 to define short-term lithostratigraphy in the Chukchi Rise. I) Surface image and elemental composition were obtained using ITRAX X-ray Fluorescence (XRF) core scanner at the Korea Polar Research Institute (KOPRI). The core scanner was equipped with a Mo-ray source operating at 30 kV and 30 mA with measurement times of 10 s. II) Color index of two sediment cores was measured on board using a portable spectrophotometer (Minolta CM 2500d, lens diameter 8 mm, a field of view \varnothing 0.8 cm) at a wavelength from 400 to 700 nm (10 nm steps). III) Grain size was measured with a Mastersizer 3000 at the KOPRI without additional dry sieving.

4.4. Results

4.4.1. Seismostratigraphy

Based on strong amplitude and lateral continuity, we defined five major reflectors (R1-5) on the SBP profile of the Chukchi Basin and the outside slopes (Fig. 4.2A). Sub-seafloor reflectors (R2-5) mainly extend to erosional surfaces by debris lobes on the lower slopes of East Siberian and Chukchi margins (Fig. 4.2B). According

to the defined reflectors, the seismostratigraphy of the studied area is divided into four seismostratigraphic units (SSUs 1-4). In the basin interior, SSUs are characterized by well-stratified reflections with variable amplitudes (Fig. 4.2B). The surficial reflector of SSU 1 blurs downward, finally becoming transparent (Fig. 4.2 B). SSU 1 is gradually thinning out from the basin interior to the slopes. In SSU 2, two reflectors with low to moderate amplitudes are recognized. Between the echo observed within SSU 2. SSU 3 is defined by the thickest and strongest lower reflector. This unit is cha-

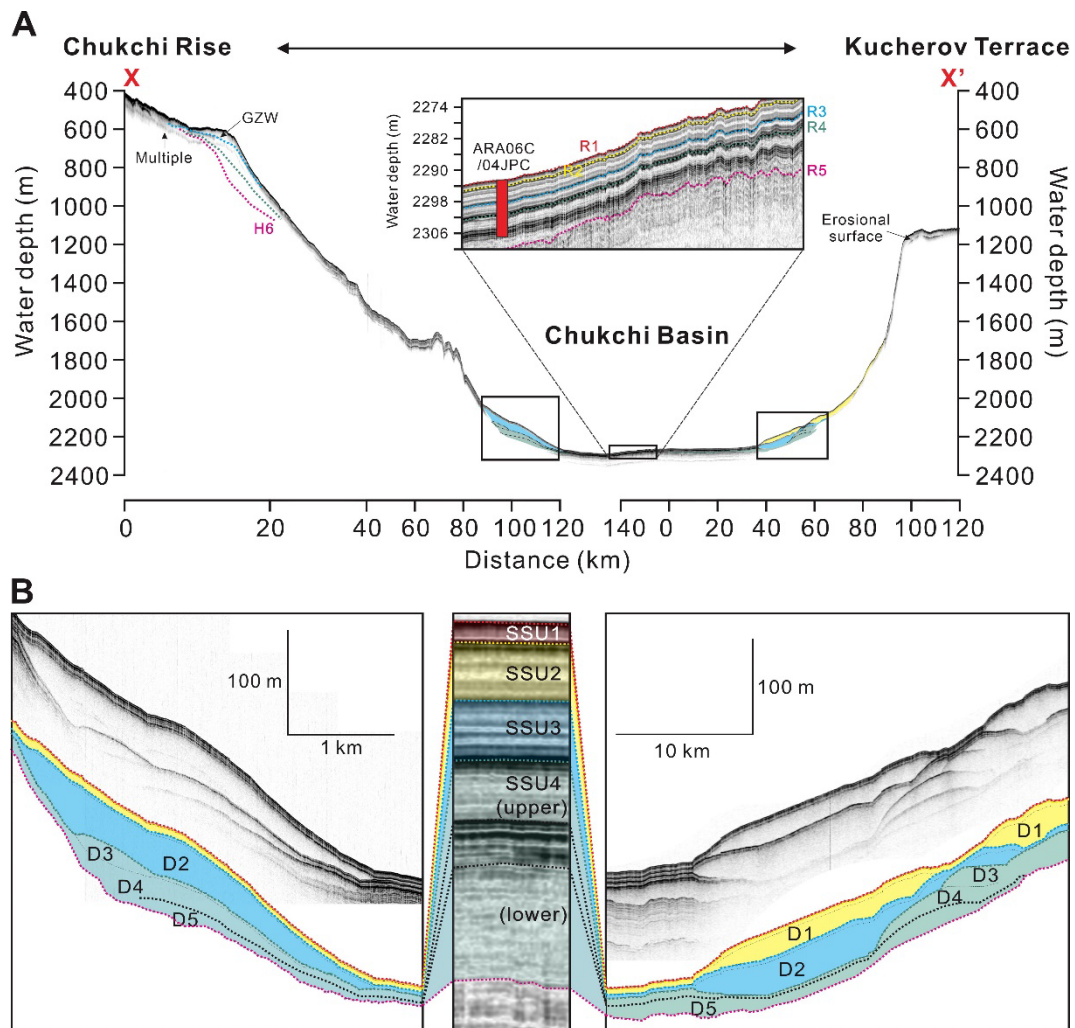


Fig. 4.2. High-resolution sub-bottom profile from the Chukchi Rise to Kucherov Terrace with the seismostratigraphic units (SSUs) defined in this study.

racterized by laterally discontinuous internal reflections. However, two continuous reflectors with moderate amplitude are observed in the middle to lower parts of this unit, which are merged towards the surrounding slopes. In this unit, debris lobes (D2) are identified on both sides of the Chukchi Basin. The debris lobes overlie the merged reflector observed in the lower part of SSU 3. The lowermost unit SSU 4 is the thickest of SSUs, overlying well-stratified older strata (see reflections below R5 in Fig. 4.2A). In the middle part of SSU 4, two strong reflectors are identified. The two reflectors can divide this unit into upper and lower sub-units (Fig. 4.2B). Both subunits in the basin interior are characterized by discontinuous or chaotic echoes with a low amplitude. Towards both sides of the Chukchi Basin, SSU 4 extends to at least three stacked debris lobes (D3-5) at the lower slopes. The defined reflectors could not be traced in the continental shelf areas due to reflector pinch-out and erosion by debris lobes at the outside slopes. However, identified on the western Chukchi Rise, the recessional moraine is partly covered by a well-stratified sediment layer of ~5 m thick. The erosional surface under the recessional moraine can be traced within the stratified sediment layer (see a white dashed line in Fig. 4.1B).

4.4.2. Lithostratigraphy

1) ARA06C/04JPC (Chukchi Basin)

In the Chukchi Basin, core 04JPC presents cyclical lithology patterns of alternating brownish, greyish, and yellowish to whitish-pinkish layers (Fig. 4.3). In core 04JPC, sixteen brown layers (indexed B1 to B16) can be defined based on sediment color, texture and structure, physical properties, and elemental composition (e.g., Stein et al., 2010; Schreck et al., 2018). The brown layer is relatively thin (less

than 10 cm) and composed of bioturbated (gravelly) sandy mud to mud (Bsm/Bm) with low to moderate amounts of iceberg-rafted debris (IRD, >1 mm). The brown layers are mostly bordered by sharp upper and mottled lower boundaries (Fig. 4.4). The brown layers are generally characterized by low WBD, high MS, and high Mn/Fe ratio. At 1297-1245 cm and 646-641 cm, two yellowish to brownish sediment layers were not defined as brown layers (Fig. 4.3) because of different lithological characteristics from the general brown layers. These layers are composed of massive or slightly stratified (gravelly) sandy mud (Msm). In addition, the numbers of IRD and the Ca/Sr ratio are relatively rich and higher, respectively (Fig. 4.3).

As counterparts, Mn-poor greyish layers (G1-G16) generally consist of fine-grained materials. Each greyish layer has a different thickness and lithofacies (Fig. 4.3). With high sediment deposition, G1-5, G7, and G16 are characterized by crudely laminated mud (CLm) and couplets of thinly laminated mud (TLm) and homogenous mud (Hm) (Fig. 4.4). Notably, G16 is the thickest of the greyish layers. In the lower part (120-1183 cm) of G16, a ~25 cm-thick thinly interlaminated sand layer (TLs) is identified. Above 1134 cm core depth, couplets of TLs and Hm are dominant. The upper part (1185-886 cm) of G16 is characterized by contorted or plastically deformed mud (Dm). In the uppermost part (886-795 cm) of G16, lithofacies changes from Dm to CLm. Coinciding with an abrupt decrease of WBD, a prominent change in sediment color is observed at 867-855 cm (Fig. 4.4). On the other hand, G6 and G8-15 are characterized by Bsm/Bm facies with low sediment deposition.

Yellowish to whitish-pinkish IRD layers are slightly bioturbated, composed of (gravelly) sandy mud. These layers are characterized by high peaks of Ca/Sr ratio and physical properties (Fig. 4.3). In general, the Ca-enriched layers have been widely used

to determine detrital carbonate-rich IRD deposition by Laurentide icebergs (Bischof and Darby, 1997; England et al., 2009; Polyak et al., 2009; Stein et al., 2010; Bazhenova et al., 2017). In addition to typical carbonate layers (W3, PW2, and PW1) in the western Arctic Ocean (Stein et al., 2010), remarkable pinkish layers are visually identified at the bottoms of B3, B12, and B15 layers (Fig. 4.4). Furthermore, prominent Ca/Sr peaks are recognizable in the interval between B8 and B16 (Fig. 4.3).

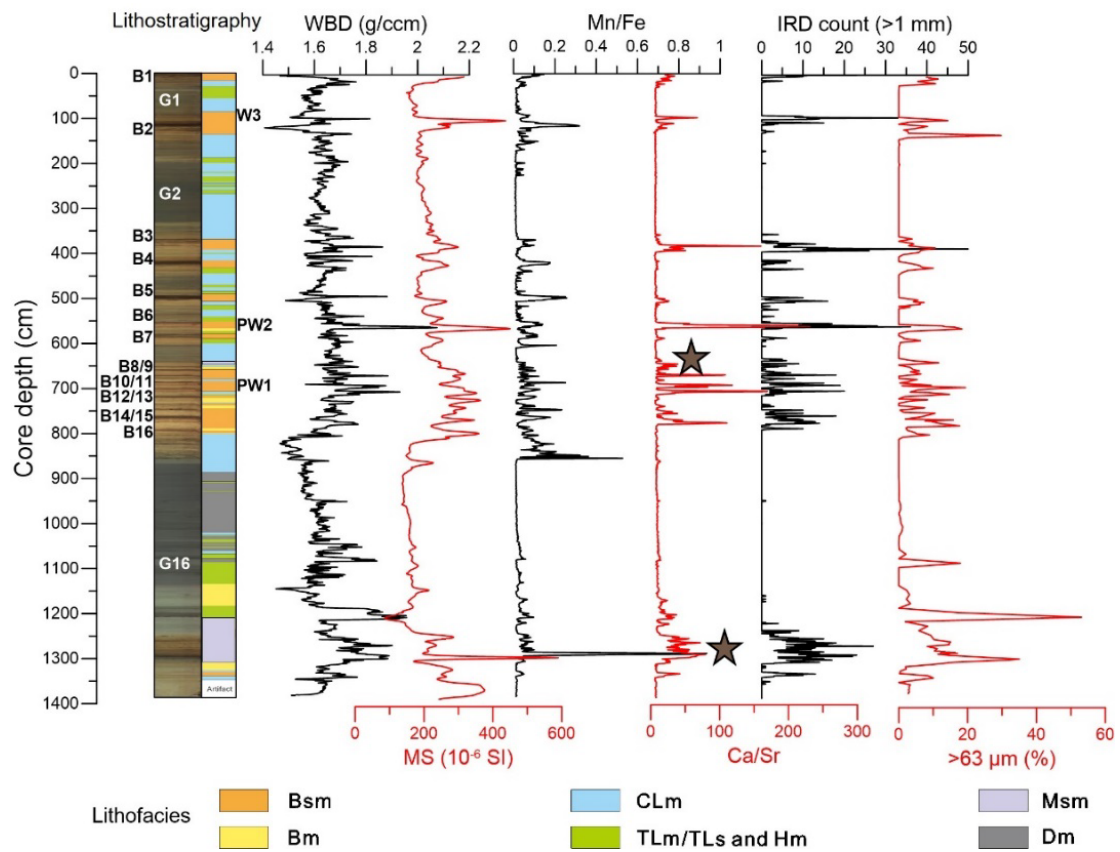


Fig. 4.3. Results of multiple lithostratigraphic measurements for ARA06C/04JPC (see Fig. 4.4 for details of lithofacies). Brown stars indicate IRD-rich layers with relatively high Ca/Sr ratio values.

2) ARA09C/ST13 and ST08 (western Chukchi Rise)

Lithostratigraphy of two Chukchi Rise cores (ST13 and ST08) can be easily defined through downcore variations in sediment color (L^* and a^*) and Mn/Fe and Ca/Sr ratios. Based on the stratigraphic correlation between two cores 04JPC and ARA02B/16B-GC from the Chukchi Basin and Arliss Plateau-ward slope (Joe et al., 2020), B1 and B2 layers are identified in two cores ST13 and ST08 (Fig. 4.5). The pinkish W3 layer with Ca/Sr peaks is found above B2 in both cores. Below B2, an abrupt increase in sand contents ($>10\%$) correlates with core 04JPC. The first greyish layer (G1) in both cores is relatively coarse-grained and thicker than 300 cm. In the upper part of G1, a coarse-grained dark greyish interval is identified with pinkish particles (possibly dolomite) as well as Ca/Sr peaks (Fig. 4.5). This interval is massive at the bottom and stratified upwards with alternations of greenish-grey and dark grey layers. The G1 layer becomes thinner toward the Chukchi Basin, and the dark grey layer within G1 disappears in the Chukchi Basin.

Based on AMS ^{14}C dating of planktic foraminiferal tests from core 04JPC, B1 and B2 layers are assigned to the time intervals of MIS 1 and MIS 3, respectively (Fig. 4.5). As shown in Fig. 4.5, the lithostratigraphic correlation corroborates that the bottom of two cores ST13 and ST08 can be constrained to the late MIS 3. This chronological lithostratigraphy is consistent with earlier stratigraphic results (e.g., Polyak et al., 2004, 2009; Adler et al., 2009; Stein et al., 2010).

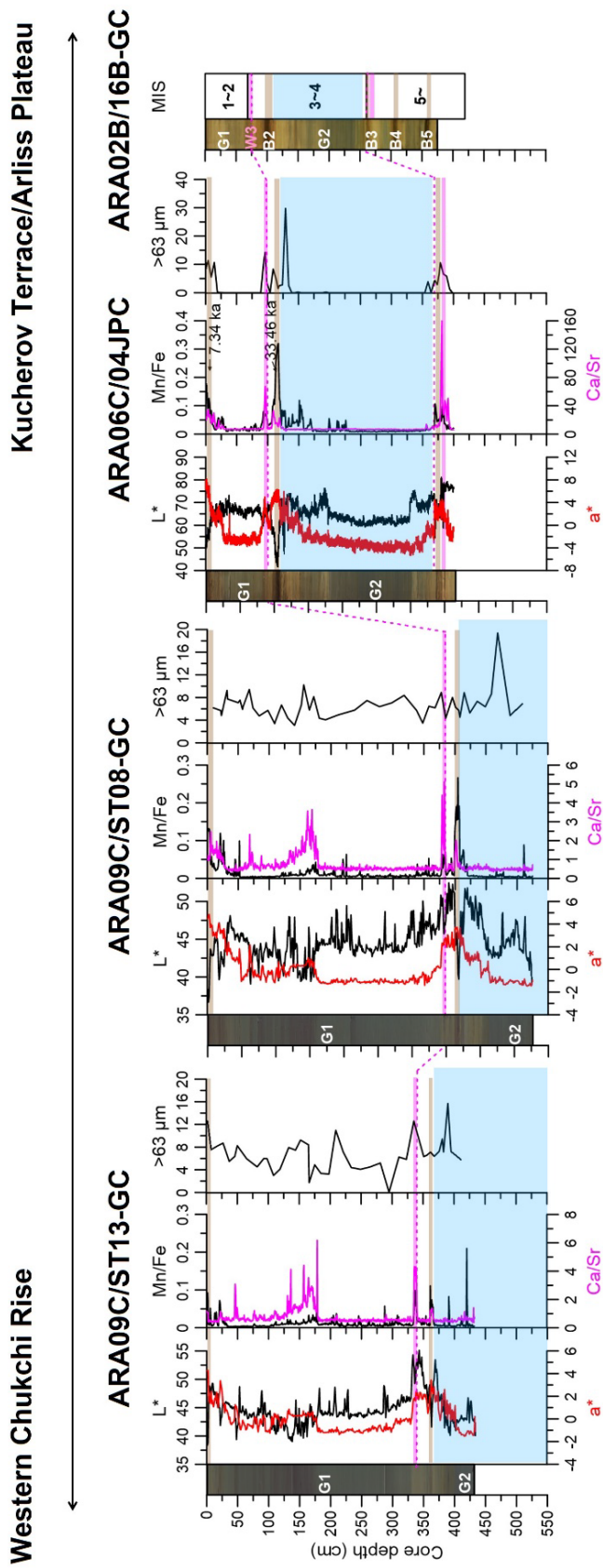


Fig. 4.5. Lithostratigraphy of two cores ST13 and ST08 based on stratigraphic correlation with core 04JPC and a reference core (ARA02B/16B-GC) (Joe et al., 2020).

4.4.3. Mineralogy

In this study, dolomite, plagioclase, kaolinite, and illite were analyzed from bulk sediments of core 04JPC (Fig. 4.6). Down-core variations in dolomite content (%) correlate well with those of the Ca/Sr ratio and the number of IRD (Fig. 4.3). The content of plagioclase ranges from 2% to 20% with an average value of 11.7 %. In the brown layers, plagioclase generally increases. In greyish layers, plagioclase varies highly and mostly increases in the couplets of TLm/TLs and Hm facies (Fig. 4.6). Kaolinite contents range from 1.6 to 6.2 % in bulk sediments, which corresponds to 3 to 19% of clay mineral groups ($K_{\text{clay sum}} = \text{kaolinite}/(\text{illite} + \text{kaolinite} + \text{chlorite} + \text{smectite})$). The increase in kaolinite is generally identified around high peaks of dolomite. The illite content ranges from 4.3 to 55.4% in bulk sediments. Illite (35.8-88.5%, average 72.7%) is predominant in the clay mineral groups (see $I_{\text{clay sum}} (\%)$ in Fig. 4.6). In brown layers, illite mostly increases. Strong amplitudes in the illite variations are identified in the G16 layer. Above 900 cm core depth, illite overall decreases toward the B8 layer. High peaks of illite occur in the G7 layer. Upward increasing patterns in illite contents are repeated from G7 to the middle part of G2 and from the upper part of G2 to G1.

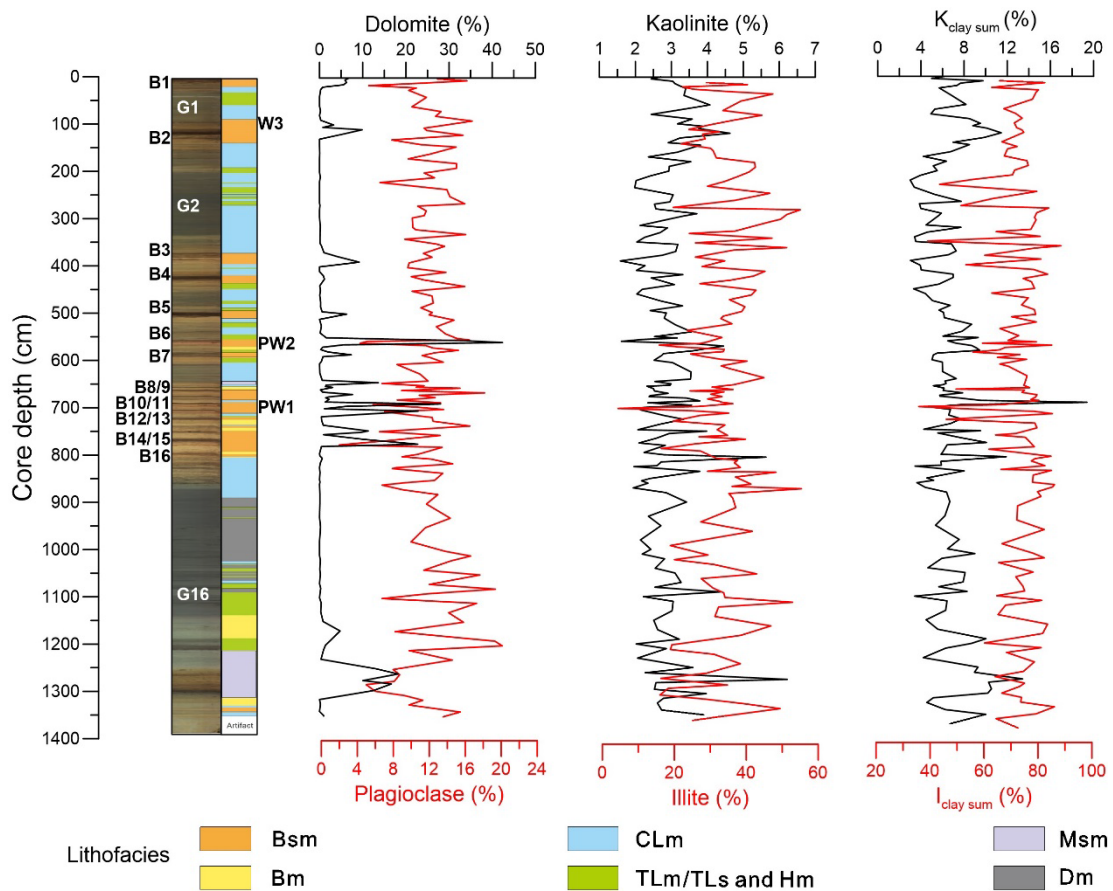


Fig. 4.6. Distribution of dolomite, Plagioclase, kaolinite, and illite in core 04JPC. $K_{\text{clay sum}}$ and $I_{\text{clay sum}}$ indicate kaolinite and illite portions of the sum of four major clay mineral groups (illite, kaolinite, chlorite, and smectite).

4.5. Discussions

4.5.1. Chronology lithostratigraphic units

Based on variations in Mn, Ca, and paleomagnetic inclination, core 04JPC correlates with previously constrained stratigraphic records for the western Arctic Ocean exemplified by cores HLY0503-8JPC (Adler et al., 2009; Xiao et al., 2020) and ARC6-C22 (Wang et al., 2021) from the Mendeleev Ridge and Northwind Ridge, respectively (Fig. 4.6). Variations in litho-, bio-, and chemostratigraphy (e.g., color, density, microfossils, Mn content) combined with independent age controls, such as

coccolith stratigraphy, luminescence dating, and ^{14}C -calibrated amino acid racemization, enabled the development of the upper to middle Quaternary stratigraphy for Arctic Ocean sediments on orbital time scales (e.g., Jakobsson et al., 2000, 2003; O'Regan et al., 2008; Kaufman et al., 2008; Xiao et al., 2020; West et al., 2021). The constrained age model appears to be robust for MIS 1-6 due to its consistency with the history of Circum-Arctic glaciations (Spielhagen et al., 2004; Dong et al., 2017; Xiao et al., 2020, 2021). An alternative age model based on U-series radioisotopes (Not and Hillaire-Marcel, 2010; Hillaire-Marcel et al., 2017) lacks this consistency, and its stratigraphic application should be improved (Xu et al., 2021; Xiao et al., 2022).

In the upper part, this age model is corroborated by two AMS ^{14}C datings of planktic foraminiferal tests, relating the age of the two uppermost brown units B1 and B2 containing foraminifers to MIS 1 and MIS 3, respectively (Fig. 4.7). This age assignment is consistent with earlier stratigraphic results on multiple Arctic Ocean cores (e.g., Polyak et al., 2004, 2009; Adler et al., 2009; Stein et al., 2010). In the general age framework for the Arctic Ocean sediments during the Late Quaternary, grey lithostratigraphic units G1-G7 of core 04JPC can be correlated with glacial and major stadial climatic intervals from MIS 2 (Last Glacial Maximum) to MIS 6 (Figs. 4.7).

Although the chronology for sediments older than MIS 6 is still uncertain, a relatively reasonable age framework has been developed for the Middle Quaternary section as well (e.g., Jakobsson et al., 2000; O'Regan et al., 2008; Polyak et al., 2009; Stein et al., 2010; Park et al., 2020; Xiao et al., 2020). According to the lithostratigraphic correlation, the predominantly brown layers in core 04JPC enclosing several ~10 cm-thick brown layers (B8-16) can be attributed to MIS 7 (Fig. 4.6). In

cores with lower resolution, the correlative interval contains lesser amounts of brown, Mn-enriched layers, likely resulting from their merging due to bioturbation at low sedimentation rates typical for the Arctic deep-sea environments (e.g., Chiu et al., 2017). This correlation is corroborated by a characteristic decline in magnetic inclination at this stratigraphic interval recorded in numerous Arctic cores (Fig. 4.6). While the nature of this paleomagnetic feature is not fully understood (e.g., Jakobsson et al., 2000; Stein et al., 2010; Channell and Xuan, 2009; Xuan and Channell, 2010), it would be related to MIS 7 recorded in many sediment cores. Accordingly, the thick grey unit G16 at the bottom of 04JPC is attributed to the glacial MIS 8 (Fig. 4.6).

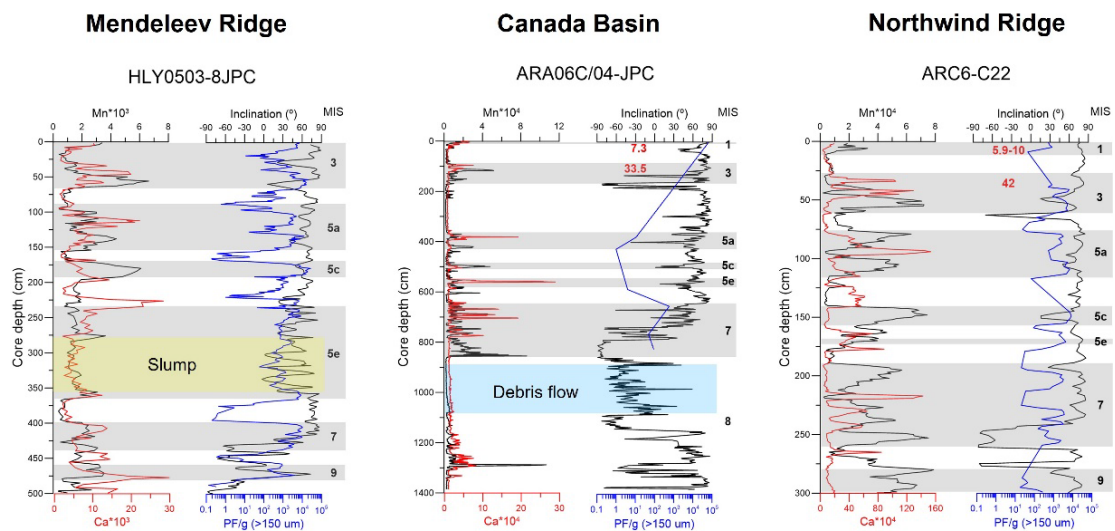


Fig. 4.7. The age model for core 04JPC based on correlation with cores HLY0503-8JPC and ARC6-C22 (Xiao et al., 2020; Wang et al., 2021). Red numbers indicate the calibrated ^{14}C dates from planktic foraminifera. For locations of core 04JPC and referenced cores, see Fig. 1A. The abundance of planktic foraminifera (PF) in 04JPC is from Grosfeld (2016) [Characteristics of Brown Layers in Core ARA06C-04 from the Chukchi Sea/Arctic Ocean covering the Mid-Pleistocene to Holocene: Age Model and Paleoenvironmental Significance]. Blue shading debris flow deposits correspond to the distribution of lithofacies Dm. For locations of core 04JPC and referenced cores see Fig. 4.1 and Table 4.1.

A recent study of Arctic nannofossil biochronology using a sediment core from the Lomonosov Ridge (Vermassen et al., 2021), suggests that the age model may need to be revised below MIS 6. According to this study, the interval regarded as MIS 7 may contain a longer stratigraphy, possibly extending to MIS 9 or 11. In that case, the lower unit G16 in core 04JPC could be older than MIS 8, like MIS 10 or 12. However, a lack of apparent glacial deposits between MIS 6 and this unit suggests MIS 8 as a more straightforward age assignment until more records need to be tested for the biostratigraphy of Vermassen et al. (2021).

4.5.2. Age constraints of glacial debris lobes

Debris lobes at the outer slopes can be contributed by glacial erosion on the surrounding continental margins. Although debris flows can potentially occur from various slope instability processes, these lobes in the Arctic Ocean consistently originated from glacial erosion and deposition downstream of continental margins and plateaux (Powell, 1990; Niessen et al., 2013; Dove et al., 2014; Batchelor and Dowdeswell, 2015; Joe et al., 2020; Kim et al., 2021). Hence, the timing of debris lobe emplacement can provide essential information for the glacial activities associated with ice-grounding events.

To accurately match the sediment core record to the seismic reflection on the Chukchi Basin sub-seafloor, acoustic impedance (AI) was calculated by multiplying wet bulk density (WBD) and p-wave velocity (V_p) from core 04JPC. Compared to WBD, some V_p values were partly not measured due to some technical problems. To obtain a continuous downcore record of V_p , the missing data were predicted by linear regression based on interpolation with WBD and V_p ($R = 0.758$). Furthermore, the AI

values were resampled from core depth (cm) to two-way travel time (TWT) using the measured V_p values.

Strong AI contrasts reflect changes in lithology such as intercalation of remarkable IRD-rich layers and sand layers (Fig. 4.8). Hence, this lithological change can form strong reflectors (Joe et al., 2020). In the Chukchi Basin, strong sub-seafloor reflectors (R2, R3, and other reflectors below upper SSU 4) are likely related to depositions of IRD-rich pinkish layers and intermittent sandy layers (Fig. 4.7). Exceptionally, the impedance contrast coinciding with reflector R4 reflects denser materials as shown in the x-ray image rather than IRD deposition. According to the core-seismic correlation applying the age model of core 04JPC, we could assign each SSU to the following time intervals (Fig. 4.8A): SSU 1 - MIS 2 to Holocene, SSU 2 - MIS 3-5, SSU 3 - MIS 6-7, SSU 4 - MIS 8.

In this context, the absence of glacial debris lobes within SSU 1 indicates that glacial erosion on the Kutcherov Terrace and western Chukchi Rise during MIS 2 including the LGM was unlikely consistent with previous estimation (Niessen et al., 2013). The first debris lobe (D1) occurs within SSU 2 on the Kutcherov Terrace slope extending to the Chukchi Basin. The emplacement of D1 corresponds to the last glacial erosion during MIS 4 and/or early MIS 3 (Joe et al., 2020). Towards the western Chukchi Rise, the coherent debris lobe did not occur. However, we note the recessional moraine on the outer shelf of western Chukchi Rise (Fig. 4.1B). Using core ST13, the core-seismic correlation can define SSUs 1 and 2 coinciding with those in the Chukchi Basin (Fig. 4.8B). In this sediment drape on top of the recessional moraine, a strong reflector corresponds to the pinkish layer W3. Core ST13 was not fully retrieved to determine the timing of the moraine formation. However, the G1 layer markedly

thickens from the Chukchi Basin to the western Chukchi Rise (Fig. 4.5). G2 in core ST13 is expected to be thicker than 2 m, supported by a uniform internal reflection pattern of the upper part of SSU 2 in the western Chukchi Rise (Fig. 4.8B). Hence, the formation of the recessional moraine can be constrained to MIS 4 to early MIS 3 (Fig. 4.7B). On both sides of the Chukchi Basin, the D2 horizon is located above two reflectors in the lower part of SSU 3 (Fig. 4.8A). The D3-5 horizons correspond to SSU 4. Based on core-seismic correlation with the age model of core 04JPC, the D2 and D3-5 are constrained to MIS 6 and MIS 8, respectively (Fig. 4.8A).

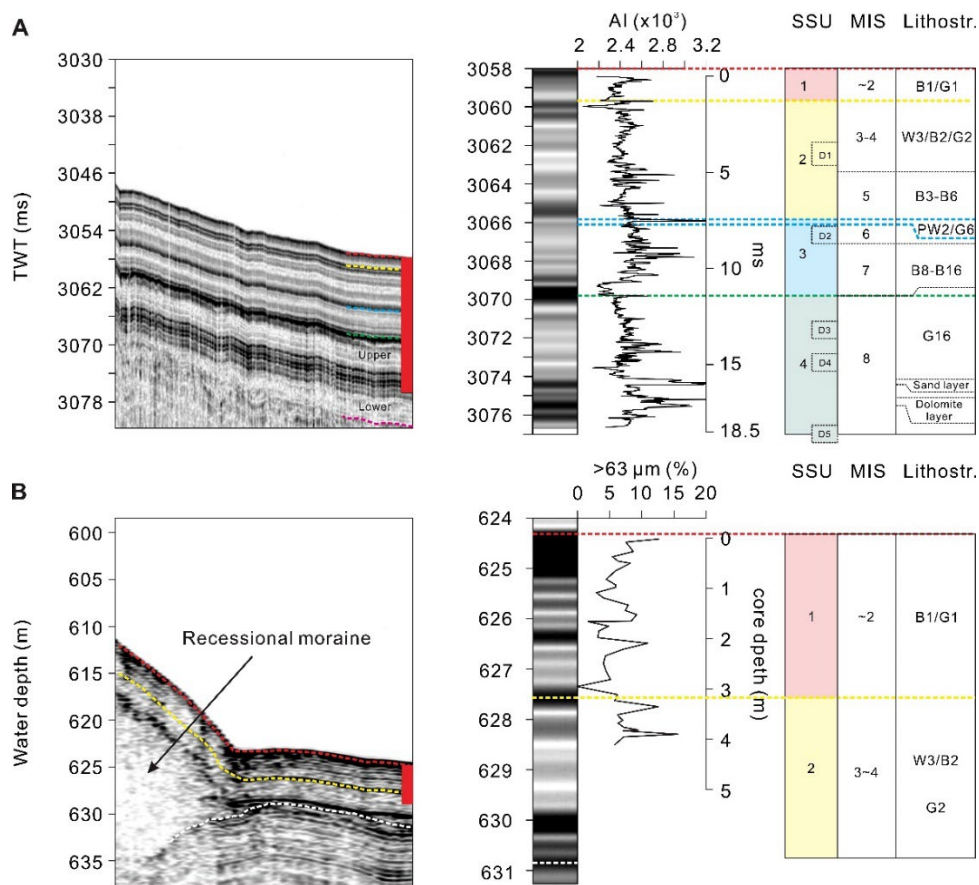


Fig. 4.8. Core-seismic correlations based on down-core variations in acoustic impedance of core 04JPC (A) and sand to gravel content (>63 μm) of core ST13 (B). Acronyms: AI, acoustic impedance. TV, Termination V; TWT, two-way travel time.

4.5.3. Glaciations on the East Siberian and Chukchi margins since MIS 8

Based on the lithostratigraphic correlation, core 04JPC may record the glacial history since MIS 8 (Fig. 4.7). The sixteen brown layers (B1-B16) characterized by intense bioturbation with some coarse debris reflects hemipelagic environments influenced by drifting ice (sea ice and/or iceberg) during interglacial/interstadial periods (Jakobsson et al., 2000; Polyak et al., 2004, 2009; März et al., 2011; Löwemark et al., 2014; Ye et al., 2019). On the other hand, fine-grained Mn-poor greyish layers (G1-G16), including several IRD-rich yellowish to whitish-pinkish layers, have been assigned to glacial to deglacial environments. For each greyish layer, differences in thickness and lithofacies suggest spatiotemporal differences in ice conditions depending on the occurrence of marine-based glaciers and/or ice sheets. Notably, in core 04JPC, the deposition of CLm and couplets of TLm/TLs and Hm facies indicates glacier-derived conditions including meltwater discharges (Hesse et al., 1996; ÓCofaigh et al., 2003; Joe et al., 2020) and glacigenic flow-type deposition, such as turbidity currents (Piper, 1978; Yoon et al., 1991), respectively. Deformed mud (Dm) facies is interpreted as glacigenic debris flow deposits, of which the deformed or contorted structure is similar to a slump deposit of core 8JPC (e.g., Adler et al., 2009). The prevalent glacial deposits such as lithofacies CLm, couplets of TLm/TLs and Hm, and Dm in G1-5, G7, and G16 layers indicate the presence of the marine-based glaciers on the continental margins surrounding the Chukchi Basin during MIS 2, MIS 4/3, MIS 5 stadials (5b, 5d), MIS 6, and MIS 8. In particular, G2, G7, and G16 correspond to the emplacements of the recessional moraine and glacigenic debris lobes (D1-D5), which further suggests the full glacier coverage on both the East Siberian and Chukchi margins during MISs 4/3, 6, and 8.

These regions can be covered by *in-situ* formed ESIS partly with the ice shelf extending from LIS (hereafter Laurentide ice shelf). The relative influence of LIS can be evaluated by changes in the sediment provenance (Fig. 4.9) with supporting seafloor morphological evidence (Figs 4.1B and C). The mineral assemblage is a typical proxy for identifying sediment sources. Plagioclase and illite are indicative of the provenance of East Siberia (Dong et al., 2017; Xiao et al., 2021; Zhang et al., 2021; Zhao et al., 2022), whereas kaolinite most likely originates from northern Alaska and Canada (Darby, 1975; Naidu and Mowatt, 1983).

During MIS 8, both ESIS and the Laurentide ice shelf had likely covered the East Siberian and Chukchi margins. At the bottom of G16 in core 04JPC, the peaks of kaolinite and dolomite with the prominent IRD deposition indicate the high sediment flux from the Laurentide ice shelf during the early stage of deglaciation. Subsequently, the shifts in the primary mineral abundance to plagioclase and illite suggest enhanced sediment inputs from ESIS. This change in sediment provenance possibly reflects either different retreat patterns between the Laurentide ice shelf and ESIS or relative distances from source areas (i.e., glaciers) to core 04JPC. As the sea level increases during deglaciation, the ice shelf would rapidly collapse and thus contributes an episodic sediment deposition. On the other hand, retreating marine ice sheets (ESIS) potentially causes a long-lasting sediment supply. However, a high abundance of kaolinite in core C22 on the Northwind Ridge during MIS 8 represents a continuous sediment input from the Laurentide ice shelf (e.g., Wang et al., 2021), ruling out the first hypothesis. Indeed, the sediments in core ICE6 on the Makarov Basin during MIS 8 were predominantly derived from ESIS as shown in relative high illite and low kaolinite (Xiao et al., 2021). This suggests that the upward disappearance of kaolinite

in core 04JPC can be attributed to a diminished influence of the Laurentide ice shelf on the Chukchi Basin during MIS 8. During this glacial period, the predominant occurrence of huge ESIS may contribute to the oldest glacial lineations on the northern Arliss Plateau (pink dashed lines in Fig. 1C) although a lack of morphological evidence is available on the Chukchi Borderland.

An overall pattern of dolomite abundances in core 04JPC during MIS 6 is similar to that of MIS 8, whereas kaolinite, illite, and plagioclase show a slight increasing trend. This suggests that the Laurentide ice shelf was likely more expanded to the Chukchi Rise than MIS 8 glacial period. The enhanced glacial influence of the Laurentide ice shelf to the Chukchi Rise is consistent with the increased sediment supply to the Northwind Ridge as recorded by the increase in kaolinite coinciding with the decrease in illite (Wang et al., 2021). Morphologically, the NEE-SWW and NNE-SSW glacial lineations are observed near the Arliss Plateau (yellow dashed lines in Fig. 1C) and the western slope (780-940 m water depth) of the Chukchi Rise, respectively. The lineation near the Arliss Plateau should have formed later than the deeper glacial erosions on the northern Arliss Plateau (pink dashed lines in Fig. 1C), and thus should be younger than MIS 8, possibly constrained to MIS 6. On the other hand, a distinct orientation (NNE-SSW) of glacial lineations on the Chukchi slope indicates a different ice flow direction in this region. This probably resulted from the coalescence of the two ice masses and consequent changes in overall ice motion (Kim et al., 2021). In the presence of ESIS, the enhanced expansion of Laurentide ice shelf can be a potential candidate, implying that the glacier lineation on the Chukchi slope was formed during MIS 6.

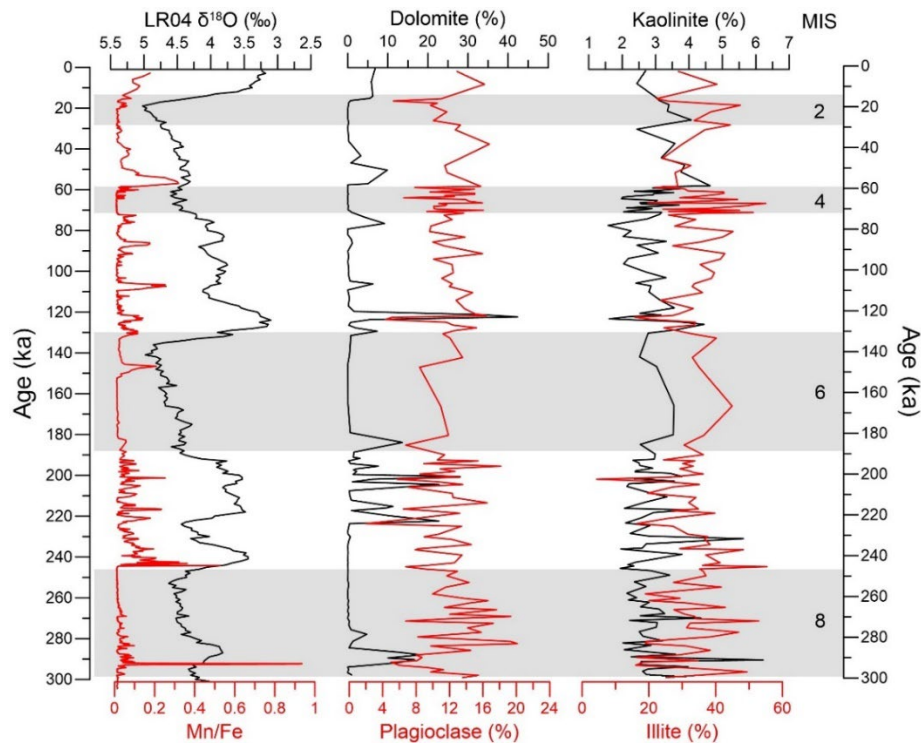


Fig. 4.9. For core 04JPC, Mn/Fe, Ca/Sr, and mineral composition time series. LR04 $\delta^{18}\text{O}$ was referred by Lisiecki and Raymo (2005).

During MIS 4, illite and kaolinite contents in core 04JPC are relatively higher and lower than MISs 8 and 6, respectively. This indicates the predominant ESIS-sourced sediments, in agreement with the previous reconstruction of ESIS during MIS 4 (Joe et al., 2020). The prominent low contents of kaolinite in the Northwind Ridge (Wang et al., 2021) point out the limited expansion of LIS up to this region. However, the glacial erosion (E-W) formed on only the southern Northwind Ridge during MIS 4 (flute 2 in Polyak et al., 2007) suggests that the Laurentide ice shelf possibly extended to the southern Northwind Ridge, possibly along with the Alaska margin (Polyak et al., 2007; Jakobsson et al., 2008; Dove et al., 2014).

Along with relatively thin and laminated G3-G5 layers (30-60 cm thick), the absence of debris lobes likely indicates the occurrences of relatively small marine-based glaciers on the Kutcherov Terrace and/or Chukchi Rise during MIS 5 stadials

(cf., 5d). During MIS 5, the up-core increase of illite and the opposite kaolinite variations may indicate that the ESIS had expanded from MIS 5 to 4. This estimation can be supported by several glacial wedges that intercalated with well-stratified hemipelagic sediment on the East Siberian margin (Niessen et al., 2013). Although the timings of the wedge emplacements have not yet been dated, Niessen et al. (2015) reported the tentative correlation between the glacial wedges and diamicton horizons in sediment cores. These correlations suggest that the ice-grounding events on the Kuchero Terrace occurred during MIS stadials, possibly MIS 5b and 5d.

Deposition of a 65 cm-thick and laminated G1 is indicative of an ice-grounding event on the Chukchi Borderland and/or East Siberian margin during MIS 2, supported by increases in illite and kaolinite of G1 in core 04JPC (Fig. 4.9). However, the absence of a debris lobe within the SSU 1 suggests that relatively small glaciers were grounded on the adjacent continental margins. E-W-oriented glacial erosion (flute 1) at water depths of shallower than ~450 m on the eastern Chukchi shelf margin indicates grounded ice extending from the LIS, age-constrained to MIS 2 (Polyak et al., 2007). In addition, on the northwestern Chukchi Rise, the presence of the youngest till deposit (T1 in Kim et al., 2021) suggests that the glacier was extended to part of the Chukchi Rise. In the East Siberian margin, recessional moraines on the seafloor of ~650 m water depth were identified in the previous study (Niessen et al., 2013). Niessen et al. (2013) postulated that this event occurred before the LGM, as a ~ 5 m-thick hemipelagic sediment layer on top of the moraines could not be deposited during the last deglacial to the Holocene based on mean sedimentation rates of the time interval MIS 1 to 5 (Stein et al., 2010). However, this glacier advance is younger than the last glacial erosion on the crest of the Arliss Plateau (Niessen et al., 2013). On the Arliss

Plateau, the last glacial erosion was recently constrained to MIS 4 to early MIS 3 (Schreck et al., 2018; Joe et al., 2020). Therefore, it suggests that the youngest ESIS likely occurred during late MIS 3 or MIS 2.

4.5.4. New Insight on the Late Quaternary Arctic ice conditions

Combined with previous reconstructions of the western Arctic glaciations (Polyak et al., 2007; Jakobsson et al., 2014; Batchelor et al., 2019), the high-resolution seismostratigraphy and sediment records in this study provide precise reconstructions of ice configuration including ESIS and the ice shelf that extends from LIS since MIS 8 (Fig. 4.10). For the glacial periods older than MIS 4, the timings of the occurrences of the huge ESIS can be constrained to MIS 6 and 8 in this study. These results are consistent with several sets of streamlined glacial lineations the Arliss Plateau (Niessen et al., 2013) and the Chukchi Borderland (Polyak et al., 2007; Dove et al., 2014; Jakobsson et al., 2014; Kim et al. 2021). These ice configurations potentially provide essential information to interpret the impacts of glaciers on the western Arctic deep-sea environments. The recurrence of huge ESIS likely provides an additional ice volume lowering the eustatic sea level during MISs 4, 6, and 8. With the approximate thickness of 1 km and the extent ($1.12 \times 10^6 \text{ km}^2$) outlined in the MIS 6 ice reconstruction (e.g., Batchelor et al., 2019), the volume of ESIS can be calculated to be $\sim 1.12 \times 10^6 \text{ km}^3$. This ice volume is approximately a quarter of that ($\sim 4.67 \times 10^6 \text{ km}^3$) of the Arctic ice shelf proposed by Jakobsson et al. (2016). Considering the relatively thin ice thickness in the Chukchi Borderland, ESIS can affect the eustatic sea level by $\sim 0.08 \text{ m}$. Hence, these findings may provide valuable information to better understand sea-level changes associated with global climate variability during the Late Quaternary.

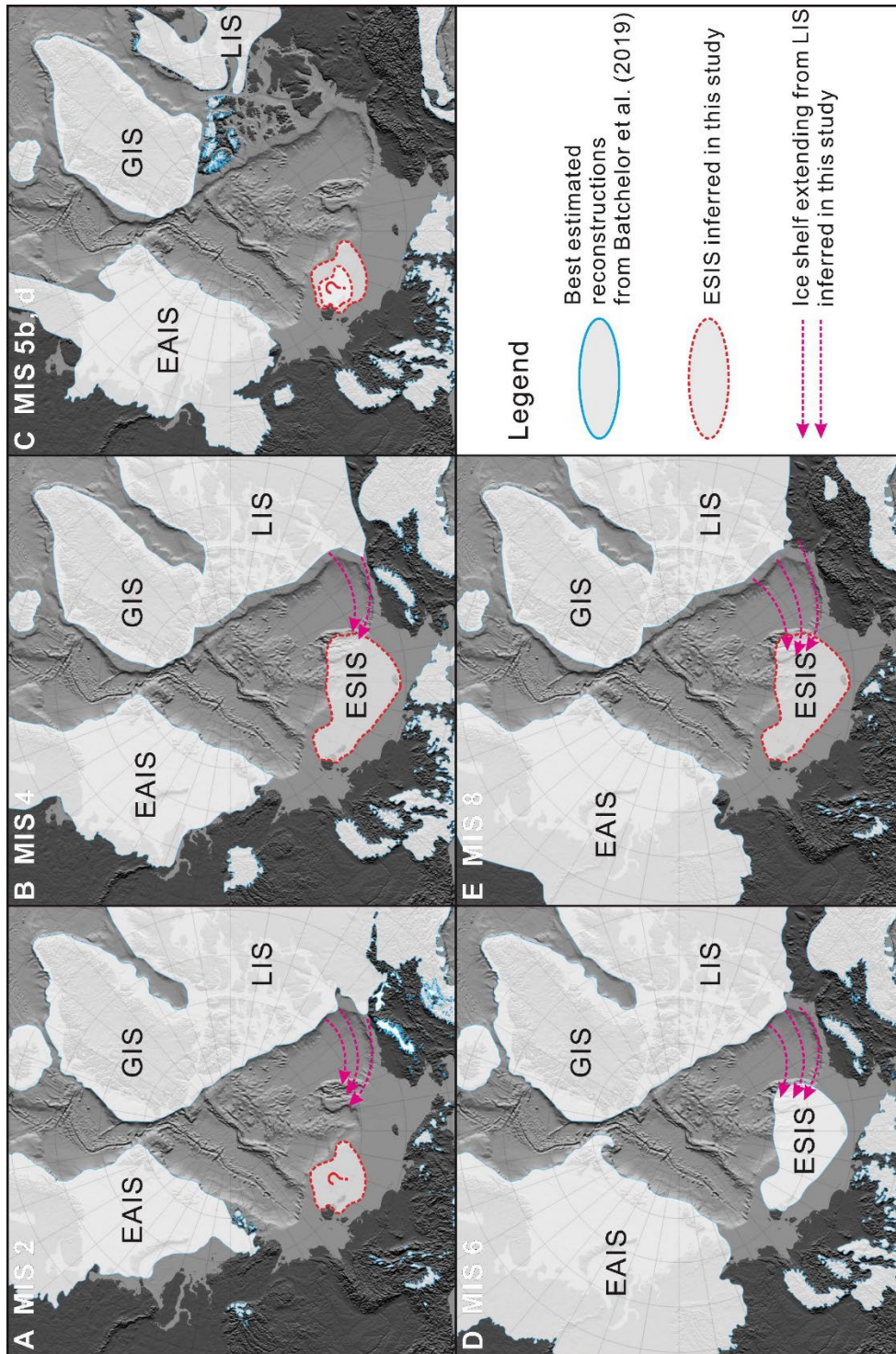


Fig. 4.10. Ice configuration of ESIS and ice shelf extending from LIS since MIS 8.

4.6. Conclusions

This study reconstructed a long-term glacial history on the East Siberian and Chukchi margins using high-resolution sediment core records and seismic data from the Chukchi Basin and adjacent areas. Based on lithostratigraphic correlation with the earlier developed stratigraphic records (8JPC, C22) from Northwind Ridge and Mendeleev Ridge, lithostratigraphy of core 04JPC and high-resolution seismostratigraphy present spatiotemporal variations in glacial impacts on the Chukchi Basin since MIS 8. For core 04JPC, multiple lithostratigraphic parameters including elemental composition, lithofacies, and mineralogy indicate that the Chukchi Basin has experienced complex glaciations by the ESIS and the ice shelf extending from the LIS. Combined with morphological evidence in the Chukchi Basin and adjacent continental margins, glacial sediments of core 04JPC suggest that a km-thick ESIS fully covered East Siberian and Chukchi margins had repeatedly occurred during MISs 4, MIS 6, and MIS 8. These findings provide new insight into the previous ice conditions of the Arctic Ocean, which contribute to a better understanding of the Arctic glacial history during the Late Quaternary.

CHAPTER 5

Conclusions

5.1. Summary

In this thesis, multi-beam bathymetry, high-resolution sub-bottom profiles, and sediment core records were analyzed to reconstruct the Arctic glacial history and attendant depositional environments in the centennial to millennial and orbital time scales. The main findings are summarized below.

Chapter 2 reconstructed the glacial history of Little Storfjorden and its tributary, Hambergbukta, since the Younger Dryas. In Little Storfjorden, two NE-SW-oriented ridges (R2) were identified. Based on the core-seismic correlation, this study for the first time proposed that R2 indicates a marine-based glacier was expanded to the vicinity of Hambergbukta during YD. In Little Storfjorden, lithofacies changes and chronological lithostratigraphy presented that the marine-based glacier rapidly melted out as the Holocene began and persisted in the open marine condition until the middle Holocene. During the late Holocene, Little Storfjorden was mostly influenced by seasonal sea ice. In Little Storfjorden, noticeable advances (or surges) and retreats of tidewater glaciers in coastal tributary fjords, including Hambergbukta, were identified as the deposition of IRD-rich surface sediments after ~1000 years BP. Based on this lithological feature and seismostratigraphy, this study provided a new age constraint on the formation of the large terminal moraine at the mouth of Hambergbukta, unlike the previous estimation.

In Chapter 3, the glacial history was reconstructed in the Arliss Plateau (AP) and the adjacent Chukchi Basin (CB) in the western Arctic Ocean off the East Siberian margin during MIS 4. This study corroborated that the last glacial erosion on the crest of the Arliss Plateau occurred during MIS 4 to early MIS 3. Combined with

chronological lithostratigraphy and lithofacies, the core-seismic correlation presented that the occurrence of a km-thick East Siberian marine ice sheet (ESIS) resulted in the deposition of glacial debris lobes as well as thick and well-laminated glacial sediments (meltwater plume deposits and turbidites) in the Chukchi Basin.

Chapter 4 reconstructed the longer-term glacial history during MIS 8 in the East Siberian and Chukchi margins as an extension of Chapter 3. This study first provided morphological evidence indicating that the ESIS was expanded to the western Chukchi Rise during MIS 4. A ~14 m-long sediment core obtained from the Chukchi Basin presented additional prominent glacial deposits, which are composed of meltwater plume deposits, turbidites, and glacial slump deposits. Corresponding to the glacial debris lobes stacked in the Chukchi Basin slopes, the glacial deposits were constrained to MISs 6 and 8 in this study. These results provided age constraints for the older glaciations by huge ESIS that were roughly postulated as several Pleistocene glaciations in the previous study.

5.2. Conclusions

This thesis presents that integrating multi-beam bathymetry, high-resolution seismostratigraphy, and sediment records allow a better understanding of the Late Quaternary glacial impacts associated with the Arctic (marine) ice sheets and/or marine-based glaciers. Precise reconstruction of the glacial history requires accurate chronology for sediment records. If sufficient biogenic calcareous material is available, this approach could reconstruct precisely glacial history and attendant depositional environments in the ranges of ^{14}C dating (40-45 ka). In the Arctic Ocean, the longer-

term chronology (especially older than MIS 6) has uncertainties in the Arctic lithostratigraphy as discussed in Chapter 4.5.1. However, this study could provide the chronology of a high-resolution lithostratigraphy from the Chukchi Basin during MIS 8 based on multiple lithostratigraphic parameters well correlative with earlier developed stratigraphic records. Regardless of the chronology, this study presents geological evidence indicating that a km-thick East Siberian marine ice sheet (ESIS) occurred repeatedly at least three times (MISs 4, 6, and 8) during the Late Quaternary. The volume of the huge ESIS is approximately a quarter of that ($\sim 4.67 \times 10^6 \text{ km}^3$) of the MIS 6 Arctic ice shelf, which can affect the eustatic sea level by $\sim 0.08 \text{ m}$. Hence, these findings provide valuable information to better understand global climate and sea-level changes during the Late Quaternary.

References

- Aagaard, K., Carmack, E.C., 1989. The role of sea ice and other fresh water in the Arctic circulation. *Journal of Geophysical Research: Oceans* 94, 14485-14498.
- Adler, R.E., Polyak, L., Ortiz, J.D., Kaufman, D.S., Channell, J.E., Xuan, C., Grottoli, A.G., Sellén, E., Crawford, K.A., 2009. Sediment record from the western Arctic Ocean with an improved Late Quaternary age resolution: HOTRAX core HLY0503-8JPC, Mendeleev Ridge. *Global and Planetary Change* 68, 18-29.
- Alekseev, M., 1997. Paleogeography and geochronology in the Russian Eastern Arctic during the second half of the Quaternary. *Quaternary International* 41, 11-15.
- Allaart, L., Müller, J., Schomacker, A., Rydningen, T.A., Håkansson, L., Kjellman, S.E., Mollenhauer, G., Forwick, M., 2020. Late Quaternary glacier and sea-ice history of northern Wijdefjorden, Svalbard. *Boreas*. <http://doi.org/10.1111/bor.12435>. ISSN 0300-9483.
- Anderson, L.G., Falck, E., Jones, E.P., Jutterström, S., Swift, J.H., 2004. Enhanced uptake of atmospheric CO₂ during freezing of seawater: A field study in Storfjorden, Svalbard. *Journal of Geophysical Research: Oceans* 109.
- Backman, J., Fornaciari, E., Rio, D., 2009. Biochronology and paleoceanography of late Pleistocene and Holocene calcareous nannofossil abundances across the Arctic Basin. *Marine Micropaleontology* 72, 86-98.
- Bartels, M., Titschack, J., Fahl, K., Stein, R., Seidenkrantz, M.-S., Hillaire-Marcel, C., Hebbeln, D., 2017. Atlantic Water advection vs. glacier dynamics in northern Spitsbergen since early deglaciation. *Clim. Past.* 13, 1717.
- Batchelor, C.L., Dowdeswell, J.A., 2014. The physiography of High Arctic cross-shelf troughs. *Quat. Sci. Rev.* 92, 68-96.
- Batchelor, C., Dowdeswell, J., 2015. Ice-sheet grounding-zone wedges (GZWs) on high-latitude continental margins. *Marine Geology* 363, 65-92.
- Batchelor, C.L., Margold, M., Krapp, M., Murton, D.K., Dalton, A.S., Gibbard, P.L., Stokes, C.R., Murton, J.B., Manica, A., 2019. The configuration of Northern Hemisphere ice sheets through the Quaternary. *Nature Communications* 10, 3713.
- Bazhenova, E., Fagel, N., Stein, R., 2017. North American origin of “pink–white” layers at the Mendeleev Ridge (Arctic Ocean): New insights from lead and neodymium isotope composition of detrital sediment component. *Marine Geology* 386, 44-55.
- Belt, S.T., Massé, G., Rowland, S.J., Poulin, M., Michel, C., LeBlanc, B., 2007. A novel chemical fossil of palaeo sea ice: IP25. *Organic Geochemistry* 38, 16-27.
- Bennett, M.R., Hambrey, M.J., Huddart, D., Glasser, N.F., Crawford, K., 1999. The landform and sediment assemblage produced by a tidewater glacier surge in Kongsfjorden, Svalbard. *Quaternary Science Reviews* 18, 1213-1246.
- Bischof, J.F., Darby, D.A., 1997. Mid-to Late Pleistocene ice drift in the western Arctic Ocean: evidence for a different circulation in the past. *Science* 277, 74-78.
- Blaauw, M., Christen, J.A., 2011. Flexible paleoclimate age-depth models using an autoregressive gamma process. *Bayesian analysis* 6, 457-474.
- Boulton, G., Van Der Meer, J.J.M., Harts, J., Beets, D., Ruegg, G., Van Der Wateren,

- F.M., Jarvis, J., 1996. Till and moraine emplacement in a deforming bed surge—an example from a marine environment. *Quat. Sci. Rev.* 15, 961-987.
- Burton, D.J., Dowdeswell, J.A., Hogan, K.A., Noormets, R., 2016. Marginal fluctuations of a Svalbard surge-type tidewater glacier, Blomstrandbreen, since the Little Ice Age: a record of three surges. *Arctic, Antarctic, and Alpine Research* 48, 411-426.
- Channell, J., Xuan, C., 2009. Self-reversal and apparent magnetic excursions in Arctic sediments. *Earth and Planetary Science Letters* 284, 124-131.
- Chough, S., 1984. Fine-grained turbidites and associated mass-flow deposits in the Ulleung (Tsushima) Back-arc Basin, East Sea (Sea of Japan). *Geol. Soc. London Spec. Publ.* 15, 185-196.
- Chiu, P.-Y., Chao, W.-S., Gyllencreutz, R., Jakobsson, M., Li, H.-C., Löwemark, L., O'Regan, M., 2017. New constraints on Arctic Ocean Mn stratigraphy from radiocarbon dating on planktonic foraminifera. *Quaternary International* 447, 13-26.
- Clark, C.D., 1994. Large-scale ice-moulding: a discussion of genesis and glaciological significance. *Sedimentary Geology* 91, 253-268.
- Clark, D.L., Whitman, R.R., Morgan, K.A., Mackey, S.D., 1980. Stratigraphy and glacial-marine sediments of the Amerasian Basin, central Arctic Ocean. Geological Society of America.
- Clement Kinney, J., Assmann, K.M., Maslowski, W., Björk, G., Jakobsson, M., Jutterström, S., Lee, Y.J., Osinski, R., Semiletov, I., Ulfsbo, A., 2022. On the circulation, water mass distribution, and nutrient concentrations of the western Chukchi Sea. *Ocean Science* 18, 29-49.
- Coulthard, R.D., Furze, M.F., Pieńkowski, A.J., Nixon, F.C., England, J.H., 2010. New marine ΔR values for Arctic Canada. *Quaternary Geochronology* 5, 419-434.
- Cronin, T.M., Dwyer, G.S., Farmer, J., Bauch, H.A., Spielhagen, R.F., Jakobsson, M., Nilsson, J., Briggs Jr, W., Stepanova, A., 2012. Deep Arctic Ocean warming during the last glacial cycle. *Nature Geoscience* 5, 631.
- Darby, D.A., Bischof, J.F., Jones, G.A., 1997. Radiocarbon chronology of depositional regimes in the western Arctic Ocean. *Deep Sea Research Part II: Topical Studies in Oceanography* 44, 1745-1757.
- Dallmann, W.K., Ohta, Y., Elvevold, S., Blomeier, D., 2002. Bedrock Map of Svalbard and Jan Mayen: Berggrunnskart Over Svalbard Og Jan Mayen. Norsk polarinstitutt.
- Dong, L., Liu, Y., Shi, X., Polyak, L., Huang, Y., Fang, X., Liu, J., Zou, J., Wang, K., Sun, F., 2017. Sedimentary record from the Canada Basin, Arctic Ocean: implications for late to middle Pleistocene glacial history. *Climate of the Past* 13, 511-531.
- Dong, L., Polyak, L., Liu, Y., Shi, X., Zhang, J., Huang, Y., 2020. Isotopic fingerprints of ice-rafted debris offer new constraints on Middle to Late Quaternary Arctic circulation and glacial history. *Geochemistry, Geophysics, Geosystems* 21, e2020GC009019.
- Dove, D., Polyak, L., Coakley, B., 2014. Widespread, multi-source glacial erosion on the Chukchi margin, Arctic Ocean. *Quaternary Science Reviews* 92, 112-122.
- Dowdeswell, J.A., Canals, M., Jakobsson, M., Todd, B., Dowdeswell, E., Hogan, K., 2016. The variety and distribution of submarine glacial landforms and implications for ice-sheet reconstruction. Geological Society, London, Memoirs

- 46, 519-552.
- Dowdeswell, J.A., Elverhøi, A., 2002. The timing of initiation of fast-flowing ice streams during a glacial cycle inferred from glacimarine sedimentation. *Mar. Geol.* 188, 3-14.
- Dowdeswell, J.A., Hogan, K., Evans, J., Noormets, R., Ó Cofaigh, C., Ottesen, D., 2010. Past ice-sheet flow east of Svalbard inferred from streamlined subglacial landforms. *Geology* 38, 163-166.
- Dypvik, H., Harris, N.B., 2001. Geochemical facies analysis of fine-grained siliciclastics using Th/U, Zr/Rb and (Zr+ Rb)/Sr ratios. *Chemical geology* 181, 131-146.
- Ehlers, J., Gibbard, P.L., 2007. The extent and chronology of Cenozoic global glaciation. *Quaternary International* 164, 6-20.
- England, J.H., Furze, M.F., Doupe, J.P., 2009. Revision of the NW Laurentide Ice Sheet: implications for paleoclimate, the northeast extremity of Beringia, and Arctic Ocean sedimentation. *Quaternary Science Reviews* 28, 1573-1596.
- Farnsworth, W. R., Ingólfsson, Ó., Alexanderson, H., Allaart, L., Forwick, M., Noormets, R., Retelle, M., Schomacker, A., 2020. Holocene glacial history of Svalbard: Status, perspectives and challenges. *Earth-Science Reviews*, 103249.
- Ferrat, M., Weiss, D.J., Spiro, B., Large, D., 2012. The inorganic geochemistry of a peat deposit on the eastern Qinghai-Tibetan Plateau and insights into changing atmospheric circulation in central Asia during the Holocene. *Geochimica et Cosmochimica Acta* 91, 7-31.
- Flink, A.E., Hill, P., Noormets, R., Kirchner, N., 2018. Holocene glacial evolution of Mohnbukta in eastern Spitsbergen. *Boreas* 47, 390-409.
- Flink, A.E., Noormets, R., Fransner, O., Hogan, K.A., ÓRegan, M., Jakobsson, M., 2017. Past ice flow in Wahlenbergfjorden and its implications for late Quaternary ice sheet dynamics in northeastern Svalbard. *Quaternary Science Reviews* 163, 162-179.
- Forman, S., Lubinski, D., Ingólfsson, Ó., Zeeberg, J., Snyder, J., Siegert, M., Matishov, G., 2004. A review of postglacial emergence on Svalbard, Franz Josef Land and Novaya Zemlya, northern Eurasia. *Quaternary Science Reviews* 23, 1391-1434.
- Forwick, M., Vorren, T.O., 2009. Late Weichselian and Holocene sedimentary environments and ice rafting in Isfjorden, Spitsbergen. *Palaeogeography, Palaeoclimatology, Palaeoecology* 280, 258-274.
- Gasson, E.G., DeConto, R.M., Pollard, D., Clark, C.D., 2018. Numerical simulations of a kilometre-thick Arctic ice shelf consistent with ice grounding observations. *Nature communications* 9, 1-9.
- Gilbert, R., 1990. Rafting in glacimarine environments. Geological Society, London, Special Publications 53, 105-120.
- Grobe, H., 1987. A simple method for the determination of ice-rafted debris in sediment cores. *Polarforschung* 57, 123-126.
- Gualtieri, L., Vartanyan, S., Brigham-Grette, J., Anderson, P., 2005. Evidence for an ice-free Wrangel Island, northeast Siberia during the Last Glacial Maximum. *Boreas* 34, 264-273.
- Hald, M., Ebbesen, H., Forwick, M., Godtlibsen, F., Khomenko, L., Korsun, S., Olsen, L.R., Vorren, T.O., 2004. Holocene paleoceanography and glacial history of the West Spitsbergen area, Euro-Arctic margin. *Quat. Sci. Rev.* 23, 2075-2088.
- Hanslik, D., Jakobsson, M., Backman, J., Björck, S., Sellén, E., O'Regan, M.,

- Fornaciari, E., Skog, G., 2010. Pleistocene Arctic Ocean sea ice and deep water isolation times. *Quat. Sci. Rev* 29, 3430-3441.
- Hambrey, M.J., Huddart, D., Bennett, M.R., Glasser, N.F., 1997. Genesis of 'hummocky moraines' by thrusting in glacier ice: evidence from Svalbard and Britain. *Journal of the Geological Society* 154, 623-632.
- Heaton, T.J., Köhler, P., Butzin, M., Bard, E., Reimer, R.W., Austin, W.E., Ramsey, C.B., Grootes, P.M., Hughen, K.A., Kromer, B., 2020. Marine20-the marine radiocarbon age calibration curve (0–55,000 cal BP). *Radiocarbon* 62, 779-820.
- Hesse, R., Ryan, W., Edwards, M., Piper, D., Group, N.S., 1996. Imaging Laurentide Ice Sheet drainage into the deep sea: impact on sediments and bottom water: *GS A Today*. September.
- Hillaire-Marcel, C., Ghaleb, B., De Vernal, A., Maccali, J., Cuny, K., Jacobel, A., Le Duc, C., McManus, J., 2017. A new chronology of late Quaternary sequences from the central Arctic Ocean based on "extinction ages" of their excesses in ^{231}Pa and ^{230}Th . *Geochemistry, Geophysics, Geosystems* 18, 4573-4585.
- Hodell, D.A., Channell, J.E., Curtis, J.H., Romero, O.E., Röhl, U., 2008. Onset of "Hudson Strait" Heinrich events in the eastern North Atlantic at the end of the middle Pleistocene transition (~ 640 ka)? *Paleoceanography* 23.
- Hu, A., Meehl, G.A., Otto-Bliesner, B.L., Waelbroeck, C., Han, W., Loutre, M.-F., Lambeck, K., Mitrovica, J.X., Rosenbloom, N., 2010. Influence of Bering Strait flow and North Atlantic circulation on glacial sea-level changes. *Nature Geoscience* 3, 118-121.
- Hughes, A.L., Gyllencreutz, R., Lohne, Ø.S., Mangerud, J., Svendsen, J.I., 2016. The last Eurasian ice sheets—a chronological database and time-slice reconstruction, DATED-1. *Boreas* 45, 1-45.
- Jakobsson, M., Andreassen, K., Bjarnadóttir, L.R., Dove, D., Dowdeswell, J.A., England, J.H., Funder, S., Hogan, K., Ingólfsson, Ó., Jennings, A., 2014. Arctic Ocean glacial history. *Quaternary Science Reviews* 92, 40-67.
- Jakobsson, M., Backman, J., Murray, A., Løvlie, R., 2003a. Optically stimulated luminescence dating supports central Arctic Ocean cm-scale sedimentation rates. *Geochemistry, Geophysics, Geosystems* 4.
- Jakobsson, M., Grantz, A., Kristoffersen, Y., Macnab, R., 2003b. Physiographic provinces of the Arctic Ocean seafloor. *Geological Society of America Bulletin* 115, 1443-1455.
- Jakobsson, M., Løvlie, R., Al-Hanbali, H., Arnold, E., Backman, J., Mörrh, M., 2000. Manganese and color cycles in Arctic Ocean sediments constrain Pleistocene chronology. *Geology* 28, 23-26.
- Jakobsson, M., Løvlie, R., Arnold, E., Backman, J., Polyak, L., Knutsen, J.-O., Musatov, E., 2001. Pleistocene stratigraphy and paleoenvironmental variation from Lomonosov Ridge sediments, central Arctic Ocean. *Glob. Planet. Change* 31, 1-22.
- Jakobsson, M., Mayer, L.A., Bringensparr, C., Castro, C.F., Mohammad, R., Johnson, P., Ketter, T., Accettella, D., Ambias, D., An, L., 2020. The international bathymetric chart of the Arctic Ocean version 4.0. *Scientific data* 7, 1-14.
- Jakobsson, M., Nilsson, J., Anderson, L., Backman, J., Björk, G., Cronin, T.M., Kirchner, N., Koshurnikov, A., Mayer, L., Noormets, R., 2016. Evidence for an ice shelf covering the central Arctic Ocean during the penultimate glaciation. *Nature Communications* 7, 1-10.

- Jakobsson, M., Polyak, L., Edwards, M., Kleman, J., Coakley, B., 2008. Glacial geomorphology of the Central Arctic Ocean: the Chukchi Borderland and the Lomonosov Ridge. *Earth Surf. Proc. Land.* 33, 526-545.
- Jang, K., Ahn, Y., Joe, Y.J., Braun, C.A., Joo, Y.J., Kim, J.-H., Bayon, G., Forwick, M., Vogt, C., Nam, S.-I., 2021. Glacial and environmental changes in northern Svalbard over the last 16.3 ka inferred from neodymium isotopes. *Global and Planetary Change*, 103483.
- Jang, K., Han, Y., Huh, Y., Nam, S.-I., Stein, R., Mackensen, A., Matthiessen, J., 2013. Glacial freshwater discharge events recorded by authigenic neodymium isotopes in sediments from the Mendeleev Ridge, western Arctic Ocean. *Earth and Planetary Science Letters* 369, 148-157.
- Jessen, S. P., Rasmussen, T. L., Nielsen, T., Solheim, A., 2010. A new late Weichselian and Holocene marine chronology for the western Svalbard slope 30,000-0 cal years BP. *Quat. Sci. Rev.* 29, 1301-1312.
- Joe, Y.J., Polyak, L., Schreck, M., Niessen, F., Yoon, S.H., Kong, G.S., Nam, S.-I., 2020. Late Quaternary depositional and glacial history of the Arliss Plateau off the East Siberian margin in the western Arctic Ocean. *Quaternary Science Reviews* 228, 106099.
- Johannessen, O., 1987. Introduction: Summer marginal ice zone experiments during 1983 and 1984 in Fram Strait and the Greenland Sea. Wiley Online Library.
- Jokat, W., 2008. The expedition of the research vessel "Polarstern" to the Arctic in 2008 (ARK-XXIII/3).
- Joo, Y.J., Forwick, M., Park, K., Joe, Y., Son, Y.J., Nam, S.-I., 2019. Holocene environmental changes in Dicksonfjorden, west Spitsbergen, Svalbard. *Polar Research*.
- Kaufman, D.S., Polyak, L., Adler, R., Channell, J.E., Xuan, C., 2008. Dating late Quaternary planktonic foraminifer *Neogloboquadrina pachyderma* from the Arctic Ocean using amino acid racemization. *Paleoceanography* 23.
- Kim, S., Polyak, L., Joe, Y.J., Niessen, F., Kim, H.J., Choi, Y., Kang, S.G., Hong, J.K., Nam, S.I., Jin, Y.K., 2021. Seismostratigraphic and geomorphic evidence for the glacial history of the northwestern Chukchi margin, Arctic Ocean. *Journal of Geophysical Research: Earth Surface* 126, e2020JF006030.
- Kirschvink, J., 1980. The least-squares line and plane and the analysis of palaeomagnetic data. *Geophysical Journal International* 62, 699-718.
- Kleiber, H., Knies, J., Niessen, F., 2000. The Late Weichselian glaciation of the Franz Victoria Trough, northern Barents Sea: ice sheet extent and timing. *Marine Geology* 168, 25-44.
- Knies, J., Matthiessen, J., Mackensen, A., Stein, R., Vogt, C., Frederichs, T., Nam, S.-I., 2007. Effects of Arctic freshwater forcing on thermohaline circulation during the Pleistocene. *Geology* 35, 1075-1078.
- Landvik, J.Y., Ingolfsson, O., Mienert, J., Lehman, S.J., Solheim, A., Elverhøi, A., Ottesen, D., 2005. Rethinking Late Weichselian ice-sheet dynamics in coastal NW Svalbard. *Boreas* 34, 7-24.
- Łącka, M., Zajączkowski, M., Forwick, M., Szczuciński, W., 2015. Late Weichselian and Holocene palaeoceanography of Storfjordrenna, southern Svalbard. *Clim. Past* 11, 587-603.

- Lawrence Phillips, R., Grantz, A., 1997. Quaternary history of sea ice and paleoclimate in the Amerasia basin, Arctic Ocean, as recorded in the cyclical strata of Northwind Ridge. *Geological Society of America Bulletin* 109, 1101-1115.
- Lefauconnier, B., Hagen, J.O., Rudant, J.P., 1994. Surging and calving glaciers in eastern Svalbard. *Norsk Polarinstitut* 1991.
- Liu, Z., Carlson, A.E., He, F., Brady, E.C., Otto-Bliesner, B.L., Briegleb, B.P., Wehrenberg, M., Clark, P.U., Wu, S., Cheng, J., 2012. Younger Dryas cooling and the Greenland climate response to CO₂. *Proceedings of the National Academy of Sciences* 109, 11101-11104.
- Löwemark, L., März, C., O'Regan, M., Gyllencreutz, R., 2014. Arctic Ocean Mn-stratigraphy: genesis, synthesis and inter-basin correlation. *Quaternary Science Reviews* 92, 97-111.
- Löwemark, L., O'Regan, M., Hanebuth, T., Jakobsson, M., 2012. Late Quaternary spatial and temporal variability in Arctic deep-sea bioturbation and its relation to Mn cycles. *Paleogeogr. Paleoclimatol. Paleoecol.* 365, 192-208.
- Lucchi, R., Camerlenghi, A., Rebesco, M., Colmenero-Hidalgo, E., Sierro, F., Sagnotti, L., Urgeles, R., Melis, R., Morigi, C., Bárcena, M.-A., 2013. Postglacial sedimentary processes on the Storfjorden and Kveithola trough mouth fans: Significance of extreme glacial marine sedimentation. *Global and planetary change* 111, 309-326.
- Lønne, I., 2001. Dynamics of marine glacier termini read from moraine architecture. *Geology* 29, 199-202.
- Margold, M., Stokes, C.R., Clark, C.D., 2018. Reconciling records of ice streaming and ice margin retreat to produce a palaeogeographic reconstruction of the deglaciation of the Laurentide Ice Sheet. *Quaternary science reviews* 189, 1-30.
- Martín-Moreno, R., Allende Álvarez, F., Hagen, J.O., 2017. 'Little Ice Age' glacier extent and subsequent retreat in Svalbard archipelago. *The Holocene* 27, 1379-1390.
- Matthiessen, J., Niessen, F., Stein, R., Naafs, B.D.A., 2010. Pleistocene glacial marine sedimentary environments at the eastern Mendeleev Ridge, Arctic Ocean. *Polarforschung* 79, 123-137.
- März, C., Stratmann, A., Matthießen, J., Meinhardt, A.-K., Eckert, S., Schnetger, B., Vogt, C., Stein, R., Brumsack, H.-J., 2011. Manganese-rich brown layers in Arctic Ocean sediments: composition, formation mechanisms, and diagenetic overprint. *Geochimica et Cosmochimica Acta* 75, 7668-7687.
- Melles, M., Brigham-Grette, J., Minyuk, P.S., Nowaczyk, N.R., Wennrich, V., DeConto, R.M., Anderson, P.M., Andreev, A.A., Coletti, A., Cook, T.L., 2012. 2.8 million years of Arctic climate change from Lake El'gygytgyn, NE Russia. *science* 337, 315-320.
- Meredith, M., Sommerkorn, M., Cassotta, S., Derksen, C., Ekaykin, A., Hollowed, A., Kofinas, G., Mackintosh, A., Melbourne-Thomas, J., Muelbert, M., 2019. Polar Regions. Chapter 3, IPCC Special Report on the Ocean and Cryosphere in a Changing Climate.
- Miller, G.H., Alley, R.B., Brigham-Grette, J., Fitzpatrick, J.J., Polyak, L., Serreze, M.C., White, J.W., 2010. Arctic amplification: can the past constrain the future? *Quaternary Science Reviews* 29, 1779-1790.
- Möller, P., Alexanderson, H., Funder, S., Hjort, C., 2015. The Taimyr Peninsula and

- the Severnaya Zemlya archipelago, Arctic Russia: a synthesis of glacial history and palaeo-environmental change during the Last Glacial cycle (MIS 5e–2). *Quat. Sci. Rev.* 107, 149-181.
- Niessen, F., Hong, J.K., Hegewald, A., Matthiessen, J., Stein, R., Kim, H., Kim, S., Jensen, L., Jokat, W., Nam, S.-I., 2013. Repeated Pleistocene glaciation of the East Siberian continental margin. *Nature Geoscience* 6, 842-846.
- Nielsen, T., Rasmussen, T.L., 2018. Reconstruction of ice sheet retreat after the Last Glacial maximum in Storfjorden, southern Svalbard. *Mar. Geol.* 402, 228-243.
- Nilsson, J., Jakobsson, M., Borstad, C., Kirchner, N., Björk, G., Pierrehumbert, R.T., Stranne, C., 2017. Ice-shelf damming in the glacial Arctic Ocean: dynamical regimes of a basin-covering kilometre-thick ice shelf. *The Cryosphere* 11, 1745-1765.
- Noormets, R., Flink, A., Kirchner, N., 2021. Glacial dynamics and deglaciation history of Hambergbukta reconstructed from submarine landforms and sediment cores, SE Spitsbergen, Svalbard. *Boreas* 50, 29-50.
- Norwegian Polar institute, 2013. Glacier Area Outlines – Svalbard, <https://doi.org/10.21334/npolar.2013.89f430f8>.
- Not, C., Hillaire-Marcel, C., 2010. Time constraints from 230Th and 231Pa data in late Quaternary, low sedimentation rate sequences from the Arctic Ocean: an example from the northern Mendeleev Ridge. *Quaternary Science Reviews* 29, 3665-3675.
- Nørgaard-Pedersen, N., Spielhagen, R.F., Thiede, J., Kassens, H., 1998. Central Arctic surface ocean environment during the past 80,000 years. *Paleoceanography* 13, 193-204.
- O'Regan, M., Backman, J., Barrientos, N., Cronin, T.M., Gemery, L., Kirchner, N., Mayer, L.A., Nilsson, J., Noormets, R., Pearce, C., 2017. The De Long Trough: a newly discovered glacial trough on the East Siberian continental margin. *Clim. Past* 13, 1269.
- O'Regan, M., King, J., Backman, J., Jakobsson, M., Pälike, H., Moran, K., Heil, C., Sakamoto, T., Cronin, T.M., Jordan, R.W., 2008. Constraints on the Pleistocene chronology of sediments from the Lomonosov Ridge. *Paleoceanography* 23
- ÓCofaigh, C., Taylor, J., Dowdeswell, J.A., Pudsey, C.J., 2003. Palaeo-ice streams, trough mouth fans and high-latitude continental slope sedimentation. *Boreas* 32, 37-55.
- Ottesen, D., Dowdeswell, J., 2006. Assemblages of submarine landforms produced by tidewater glaciers in Svalbard. *Journal of Geophysical Research: Earth Surface* 111
- Pälli, A., Moore, J.C., Jania, J., Glowacki, P., 2003. Glacier changes in southern Spitsbergen, Svalbard, 1901–2000. *Annals of Glaciology* 37, 219-22
- Pieńkowski, A.J., Husum, K., Furze, M.F., Missana, A.F., Irvall, N., Divine, D.V., Eilertsen, V.T., 2021. Revised ΔR values for the Barents Sea and its archipelagos as a pre-requisite for accurate and robust marine-based ^{14}C chronologies. *Quaternary Geochronology*, 101244.
- Piper, D.W., 1978. Turbidite muds and silts on deepsea fans and abyssal plains. In Stanley, D.J. and Kelling, G. (eds.), *Sedimentation in submarine canyons, fans, and trenches*, Hutchinson and Ross Stroudsburg, 163-176.

- Plassen, L., Vorren, T.O., Forwick, M., 2004. Integrated acoustic and coring investigation of glacial deposits in Spitsbergen fjords. *Polar Research* 23, 89-110.
- Poirier, R.K., Cronin, T.M., Briggs Jr, W.M., Lockwood, R., 2012. Central Arctic paleoceanography for the last
- Polyak, L., Bischof, J., Ortiz, J.D., Darby, D.A., Channell, J.E., Xuan, C., Kaufman, D.S., Løvlie, R., Schneider, D.A., Eberl, D.D., 2009. Late Quaternary stratigraphy and sedimentation patterns in the western Arctic Ocean. *Global and Planetary Change* 68, 5-17.
- Polyak, L., Darby, D.A., Bischof, J.F., Jakobsson, M., 2007. Stratigraphic constraints on late Pleistocene glacial erosion and deglaciation of the Chukchi margin, Arctic Ocean. *Quat. Res.* 67, 234-245.
- Polyak, L., Curry, W.B., Darby, D.A., Bischof, J., Cronin, T.M., 2004. Contrasting glacial/interglacial regimes in the western Arctic Ocean as exemplified by a sedimentary record from the Mendeleev Ridge. *Palaeogeography, Palaeoclimatology, Palaeoecology* 203, 73-93.
- Poore, R., Osterman, L., Curry, W., Phillips, R., 1999. Late Pleistocene and Holocene meltwater events in the western Arctic Ocean. *Geology* 27, 759-762.
- Powell, R.D., 1990, Glacimarine processes at grounding-line fans and their growth to ice-contact deltas, in Dowdeswell, J.A., and Scourse, J.D., eds., *Glacimarine Environments: Processes and Sediments: Geological Society of London Special Publication* 53, p. 53-73.
- Powell, R.D., Alley, R.B., 1997. Grounding-line systems: processes, glaciological inferences and the stratigraphic record. *Geology and seismic stratigraphy of the Antarctic Margin*, 2 71, 169-187.
- Rasmussen, T.L., Thomsen, E., 2014. Brine formation in relation to climate changes and ice retreat during the last 15,000 years in Storfjorden, Svalbard, 76-78 N. *Paleoceanography* 29, 911-929.
- Rasmussen, T.L., Thomsen, E., 2015. Palaeoceanographic development in S torfjorden, S valbard, during the deglaciation and H olocene: evidence from benthic foraminiferal records. *Boreas* 44, 24-44.
- Rasmussen, T.L., Thomsen, E., 2021. Climate and ocean forcing of ice-sheet dynamics along the Svalbard-Barents Sea ice sheet during the deglaciation ~ 20,000-10,000 years BP. *Quaternary Science Advances* 3, 100019.
- Rigor, I.G., Wallace, J.M., Colony, R.L., 2002. Response of sea ice to the Arctic Oscillation. *Journal of Climate* 15, 2648-2663.
- Romanovskii, N., Hubberten, H.-W., Gavrilov, A., Tumskey, V., Kholodov, A., 2004. Permafrost of
- Rothwell, R.G., Croudace, I.W., 2015. Twenty years of XRF core scanning marine sediments: what do geochemical proxies tell us? In: Croudace, I.W., Rothwell, R.G. (Eds.), *Micro-XRF Studies of Sediment Cores*. Springer, Dordrecht, pp. 25-102.
- Schauer, U., Fahrbach, E., Osterhus, S., Rohardt, G., 2004. Arctic warming through the Fram Strait: Oceanic heat transport from 3 years of measurements. *Journal of Geophysical Research: Oceans* 109.
- Schauer, U., 1995. The release of brine-enriched shelf water from Storfjord into the Norwegian sea. *J. Geophys. Res.* 100, 16015-16028
- Schreck, M., Nam, S.-I., Polyak, L., Vogt, C., Kong, G.-S., Stein, R., Matthiessen, J.,

- Niessen, F., 2018. Improved Pleistocene sediment stratigraphy and paleoenvironmental implications for the western Arctic Ocean off the East Siberian and Chukchi margins. *arktos* 4, 1-20.
- Serreze, M.C., Barry, R.G., 2011. Processes and impacts of Arctic amplification: A research synthesis. *Global and planetary change* 77, 85-96.
- Skirbekk, K., Kristensen, D.K., Rasmussen, T.L., Koç, N., Forwick, M., 2010. Holocene climate variations at the entrance to a warm Arctic fjord: evidence from Kongsfjorden trough, Svalbard. Geological Society, London, Special Publications 344, 289-304.
- Skogseth, R., Haugan, P., Jakobsson, M., 2005. Watermass transformations in Storfjorden. *Continental Shelf Research* 25, 667-695.
- Skogseth, R., Sandvik, A., Asplin, L., 2007. Wind and tidal forcing on the meso-scale circulation in Storfjorden, Svalbard. *Continental Shelf Research* 27, 208-227.
- Solheim, A., Elverhøi, A., Andersen, E.S., Jahre, H., 1991. Marine geological/geophysical cruise on the western Svalbard margin 1990: cruise report.
- Spielhagen, R.F., Baumann, K.-H., Erlenkeuser, H., Nowaczyk, N.R., Nørgaard-Pedersen, N., Vogt, C., Weiel, D., 2004. Arctic Ocean deep-sea record of northern Eurasian ice sheet history. *Quat. Sci. Rev.* 23, 1455-1483.
- Spielhagen, R.F., Erlenkeuser, H., Siegert, C., 2005. History of freshwater runoff across the Laptev Sea (Arctic) during the last deglaciation. *Global and Planetary Change* 48, 187-207.
- Spielhagen, R.F., Werner, K., Sørensen, S.A., Zamelczyk, K., Kandiano, E., Budeus, G., Husum, K., Marchitto, T.M., Hald, M., 2011. Enhanced modern heat transfer to the Arctic by warm Atlantic water. *Science* 331, 450-453.
- Stein, R., Matthiessen, J., Niessen, F., Krylov, A., Nam, S.-i., Bazhenova, E., 2010. Towards a better (litho-) stratigraphy and reconstruction of Quaternary paleoenvironment in the Amerasian Basin (Arctic Ocean). *Polarforschung* 79, 97-121.
- Stokes, C., Margold, M., Clark, C., Tarasov, L., 2016. Ice stream activity scaled to ice sheet volume during Laurentide Ice Sheet deglaciation. *Nature* 530, 322.
- Stroeve, J., Notz, D., 2018. Changing state of Arctic sea ice across all seasons. *Environmental Research Letters* 13, 103001.
- Stuiver, M., Reimer, P.J., 1993. Extended 14C data base and revised CALIB 3.0 14C age calibration program. *Radiocarbon* 35, 215-230.
- Svendsen, J.I., Alexanderson, H., Astakhov, V.I., Demidov, I., Dowdeswell, J.A., Funder, S., Gataullin, V., Henriksen, M., Hjort, C., Houmark-Nielsen, M., 2004. Late Quaternary ice sheet history of northern Eurasia. *Quaternary Science Reviews* 23, 1229-1271.
- Svendsen, J.I., Elverhmi, A., Mangerud, J., 1996. The retreat of the Barents Sea Ice Sheet on the western Svalbard margin. *Boreas* 25, 244-256
- Tjallingii, R., Röhl, U., Kölling, M., Bickert, T., 2007. Influence of the water content on X-ray fluorescence core-scanning measurements in soft marine sediments. *Geochemistry, Geophysics, Geosystems* 8.
- van Aken, H.M., Quadfasel, D., Warpakowski, A., 1991. The Arctic front in the Greenland Sea during February 1989: Hydrographic and biological observations. *Journal of Geophysical Research: Oceans* 96, 4739-4750.
- Vermassen, F., O'Regan, M., West, G., Cronin, T.M., Coxall, H.K., 2021. Testing the

- stratigraphic consistency of Pleistocene microfossil bioevents identified on the Alpha and Lomonosov Ridges, Arctic Ocean. *Arctic, Antarctic, and Alpine Research* 53, 309-323.
- Vorren, T.O., Laberg, J.S., F., B., Dowdeswell, J.A., N.H., K., J., M., J., R., Werner, F., 1998. The Norwegian-Greenland Sea Continental Margins: Morphology and Late Quaternary Sedimentary Processes and Environment. *Quat. Sci. Rev.* 17, 273-302.
- Wang, R., Polyak, L., Xiao, W., Wu, L., Zhang, T., Sun, Y., Xu, X., 2018. Late-Middle Quaternary lithostratigraphy and sedimentation patterns on the Alpha Ridge, central Arctic Ocean: Implications for Arctic climate variability on orbital time scales. *Quat. Sci. Rev.* 181, 93-108.
- Wang, R., Polyak, L., Zhang, W., Yu, X., Ye, L., Dong, L., Liu, Y., Wang, W., Diekmann, B., 2021. Glacial-interglacial sedimentation and paleocirculation at the Northwind Ridge, western Arctic Ocean. *Quaternary Science Reviews* 258, 106882.
- Wang, R., Xiao, W., März, C., Li, Q., 2013. Late Quaternary paleoenvironmental changes revealed by multi-proxy records from the Chukchi Abyssal Plain, western Arctic Ocean. *Glob. Planet. Change* 108, 100-118.
- Wassmann, P., Kosobokova, K., Slagstad, D., Drinkwater, K., Hopcroft, R., Moore, S., Ellingsen, I., Nelson, R., Carmack, E., Popova, E., 2015. The contiguous domains of Arctic Ocean advection: trails of life and death. *Progress in Oceanography* 139, 42-65.
- Weingartner, T.J., Danielson, S., Sasaki, Y., Pavlov, V., Kulakov, M., 1999. The Siberian Coastal Current: A wind-and buoyancy-forced Arctic coastal current. *Journal of Geophysical Research: Oceans* 104, 29697-29713.
- West, G., Alexanderson, H., Jakobsson, M., O'Regan, M., 2021. Optically stimulated luminescence dating supports pre-Eemian age for glacial ice on the Lomonosov Ridge off the East Siberian continental shelf. *Quaternary Science Reviews* 267, 107082.
- Wiberg, D.H., Haflidason, H., Laberg, J.S., 2022. An updated Weichselian chronostratigraphic framework of the Kongsfjorden Trough Mouth Fan and its implications for the glacial history of Svalbard. *Boreas*.
- Winkelmann, D., Knies, J., 2005. Recent distribution and accumulation of organic carbon on the continental margin west off Spitsbergen. *Geochemistry, Geophysics, Geosystems* 6.
- Winsor, P., Chapman, D.C., 2004. Pathways of Pacific water across the Chukchi Sea: A numerical model study. *Journal of Geophysical Research: Oceans* 109.
- Wollenburg, J.E., Kuhnt, W., 2000. The response of benthic foraminifers to carbon flux and primary production in the Arctic Ocean. *Marine Micropaleontology* 40, 189-231.
- Woodgate, R.A., Weingartner, T.J., Lindsay, R., 2012. Observed increases in Bering Strait oceanic fluxes from the Pacific to the Arctic from 2001 to 2011 and their impacts on the Arctic Ocean water column. *Geophysical Research Letters* 39.
- Xiao, W., Polyak, L., Wang, R., Löwemark, L., Mei, J., You, D., Wang, W., Wu, L., Jin, X., 2020. Middle to Late Pleistocene Arctic paleoceanographic changes based on sedimentary records from Mendeleev Ridge and Makarov Basin. *Quaternary Science Reviews* 228, 106105.

- Xiao, W., Polyak, L., Wang, R., Not, C., Dong, L., Liu, Y., Ma, T., Zhang, T., 2021. A sedimentary record from the Makarov Basin, Arctic Ocean, reveals changing middle to Late Pleistocene glaciation patterns. *Quaternary Science Reviews* 270, 107176.
- Xiao, X., Fahl, K., Müller, J., Stein, R., 2015a. Sea-ice distribution in the modern Arctic Ocean: Biomarker records from trans-Arctic Ocean surface sediments. *Geochimica et Cosmochimica Acta* 155, 16-29.
- Xiao, X., Stein, R., Fahl, K., 2015b. MIS 3 to MIS 1 temporal and LGM spatial variability in Arctic Ocean sea ice cover: Reconstruction from biomarkers. *Paleoceanography* 30, 969-983.
- Xu, Q., Xiao, W., Wang, R., Sufke, F., Lippold, J., Not, C., 2021. Driving mechanisms of sedimentary ^{230}Th and ^{231}Pa variability in the western Arctic Ocean through the last glacial cycle. *Paleoceanography and Paleoclimatology* 36, e2020PA004039.
- Xuan, C., Channell, J.E., 2010. Origin of apparent magnetic excursions in deep-sea sediments from Mendeleev-Alpha Ridge, Arctic Ocean. *Geochemistry, Geophysics, Geosystems* 11.
- Ye, L., März, C., Polyak, L., Yu, X., Zhang, W., 2019. Dynamics of manganese and cerium enrichments in Arctic Ocean sediments: a case study from the Alpha Ridge. *Frontiers in Earth Science* 6, 236.
- Yoon, S., Chough, S., Thiede, J., Werner, F., 1991. Late Pleistocene sedimentation on the Norwegian continental slope between 67 and 71 N. *Mar. Geol.* 99, 187-207.
- Ziaja, W., Ostafin, K., 2015. Landscape–seascape dynamics in the isthmus between Sørkapp Land and the rest of Spitsbergen: Will a new big Arctic island form? *Ambio* 44, 332-342.
- Zuchuat, V., Sleveland, A., Twitchett, R., Svensen, H., Turner, H., Augland, L.E., Jones, M.T., Hammer, Ø., Hauksson, B., Haflidason, H., 2020. A new high-resolution stratigraphic and palaeoenvironmental record spanning the End-Permian Mass Extinction and its aftermath in central Spitsbergen, Svalbard. *Palaeogeography, Palaeoclimatology, Palaeoecology* 554, 109732.
- Zhao, S., Liu, Y., Dong, L., Shi, X., Polyak, L., Zou, X., Wang, W., Wu, D., 2022. Sedimentary record of glacial impacts and melt water discharge off the East Siberian Continental Margin, Arctic Ocean. *Journal of Geophysical Research: Oceans* 127, e2021JC017650.

국문요지

북극해는 지구온난화에 가장 민감하게 반응하는 지역으로써 기후변화를 이해하기 위한 최적의 장소이다. 이러한 북극해의 대륙 빙상과 해양기저빙하는 과거 지구기후변화와 범세계적인 해수면 변동을 조절하는 주요 요인으로, 북극해의 빙하 역사를 더욱 정밀하게 복원하는 것은 과거 기후변화를 이해하는데 있어서 필수적이다. 본 학위논문의 연구목적은 정밀한 해저지형, 고해상도 탄성과층서 및 시추 퇴적물 코어에 대한 암층서와 암상을 토대로 제4기 후기 동안 북극해의 빙하역사 및 빙·해양 퇴적 환경의 변화를 정밀하게 복원하는 것이며, 백년-천년(centennial to millennial) 및 천체시간규모(orbital timescales)의 빙하 역사를 다루었다.

첫 번째 연구는 스발바르 남동부에 위치한 리틀 스토르피오르덴과 연안 피오르드 햄버그북타에서 Younger Dryas (YD) 이후 빙하 역사를 100년-1000년 시간 규모로 복원하였다. 탄성과층서, 퇴적물 코어에 대한 연대 분석, 암층서 분석 및 암상 분석결과를 토대로, 햄버그북타에서 확보된 시추 퇴적물 코어는 1900년 이후로 퇴적된 빙·해양 퇴적물로 구성되며, 리틀 스토르피오르덴에서 퇴적물 기록(HH19-905-GC)은 YD 동안 퇴적된 빙하 퇴적물을 포함하는 것으로 확인되었다. 햄버그북타와 인접한 리틀 스토르피오르덴 해저지형에서는 북동-남서 방향의 두 해령(R1, R2)이 발견되었고, 코어-탄성과 대비 결과로부터 해령 R2가 YD 시기의 해양기저빙하의 발달을 지시하는 해저지형임이 확인되었다. 코어 905의 퇴적물 기록에 근거하여, 스발바르 남동부 해양기저빙하는 홀로세 초기 동안 빠르게 후퇴하였음을 보여주었다. 홀로세 초·중기 동안 빙하가 없는 해양환경 하에 강한 저층류의 영향은 리틀 스토르피오르덴에서 매우 낮은 퇴적율을 야기하였다. 홀로세 후기는 주로 계절빙(seasonal sea ice) 환경이 조성되었으며, 햄버그북타를 포함하여 연안 피오르드에서 조수빙하의 강한 전진과 후퇴는 오직 지난 1000년 이후 퇴적된 뚜렷한 IRD (ice-rafted debris)층의 발달로 확인되었다. 이러한 결과를 바탕으로, 본 연구에서는 기존 연구와 다르게 햄버그북타 종퇴석 복합체(terminal moraine complex)가 소빙하기 (Little Ice Age) 동안

전진하였던 조수 빙하에 의해 형성된 빙하기원 지형으로써 새로운 해석을 제안하였다.

두 번째 연구는 서 북극해 동시베리아 주변 해역에 위치한 앨리스 대지(Arliss Plateau)와 동부 사면으로 이어지는 척치 분지(Chukchi Basin)에서 해저지형, 탄성파층서 및 암층서와 암상 분석을 통해 marine isotope stage (MIS) 4 이후의 빙하역사와 퇴적환경을 복원하였다. 암층서 대비에 근거하여, 앨리스 대지의 사면 하부에서 획득된 시추 퇴적물 코어(ARA02B/16B-GC)는 지난 약 100 ka 동안의 기록이 보존된 것으로 확인되었고, 빙하기-간빙기 순환에 따른 뚜렷한 퇴적양상을 보여주었다. 간빙기 퇴적층은 비교적 얇고 망간이 풍부한 생교란된 사질니 퇴적상으로 구성되어 있으며, 이는 반원양성 퇴적환경을 지시한다. 반면, MIS 4/3와 MIS 2/1의 빙하기/해빙기 퇴적층은 해양기저빙하에서 반복적으로 형성되는 용빙수, 저탁류 및 빙산에 의한 IRD 퇴적 등 다양한 빙하기원 퇴적양상을 보여주었다. 앨리스 대지 사면에서 수평 연속성이 양호한 강한 반사면에 의해 탄성파층서 단위(SSUs 1, 2)가 정의되었으며, 탄성파층서와 시추 퇴적물 코어 간에 대비를 통해, SSU 1과 SSU 2는 각각 MIS 3-1과 MIS 5c-3의 시기로 제한되었다. SSU 2에서 관찰된 음향학적으로 투명한 렌즈는 앨리스 대지의 빙하침식 흔적으로부터 하부사면으로 이어지는 암설류로 해석되었다. 이러한 지형 발달 및 퇴적양상은 앨리스 대지의 빙하침식과 이와 관련된 퇴적환경 변화를 지시한다. 암층서 및 암상 분포에 근거하여, 빙하기원 암설류는 후기 MIS 4에서 초기 MIS 3 동안 빙하기/해빙기에 퇴적된 반면, SSU 1에서의 빙하기원 암설류가 발달되지 않았다는 것은 마지막 최대 빙하기 동안에 앨리스 대지가 직접적인 빙하작용을 받지 않았음을 지시한다. 특히, 이 연구는 동시베리아 주변부 앨리스 대지를 침식시켰던 마지막 거대빙하의 발달 시기를 MIS 4/3로 제안함으로써 제4기 후기 동안 서 북극 대륙붕 해역에 마지막으로 존재하였던 거대빙하의 시기를 처음으로 제시하였다.

세 번째 연구는 서 북극해 빙하역사복원에 대한 후속연구로써 동시베리아와 척치 주변 해역에 지난 30만년 동안의 장주기적인 빙하역사를 복원하였다. 이 연구는 척치 라이즈(Chukchi Rise)에서 쿠체로프 테라스(Kutcherov Terrace)를 아우르는 탄성파층서와 척치 분지에서 획득한 약 14 m 길이의 고해상도 시추 퇴적물

코어(ARA06C/04JPC)를 보여준다. 이와 더불어, MIS 4/3 동안 동시베리아 거대빙상(ESIS)이 척치 라이즈까지 확장되었는지 평가하기 위해 비교적 짧은 두 점의 시추 퇴적물 코어(ARA09C/ST13, ST08)가 추가적으로 분석되었다. 수평 연속성이 좋은 강한 반사면을 기준으로, 본 연구지역에서 4개의 탄성파층서 단위(SSUs 1-4)가 정의되었으며, 각 층서 단위에서 빙하기원 암설류가 확인되었다. 코어 04JPC에서, 간빙기/아간빙기를 지시하는 총 16개의 갈색층(B1-B16)이 정의되었으며, 생교란된 사질니(Bsm)와 생교란 니(Bm)로 구성된다. 각 갈색층 사이에서, 다양한 두께와 암상을 보이는 회색층(G1-16)이 구분되며, 비교적 두껍게 발달된 회색층, G1-5와 G7은 용빙수, 세립질 저탁류를 지시하는 암상(CLm, TLm/Hm)이 우세하였다. 특히, 가장 두껍게 발달된 G16은 용빙수에 의한 퇴적을 포함하여 조립질 저탁류와 빙하기원 암설류를 지시하는 암상(TLs/Hm, Dm)이 특징적으로 확인되었으며, 이는 빙하 거동에 의해 야기되는 역동적인 퇴적환경을 지시한다. 코어 04JPC의 연대모델을 적용하여, 빙하기원 암상의 발달은 해양기저빙하가 MISs 2, 4/3, 5d 혹은 5b, 6 및 8에 존재했음을 지시하였다. 빙하기원 암설류를 동반한 G2, G7 및 G16의 퇴적은 동시베리아와 척치 주변해역까지 완전히 덮을만한 거대빙하가 MISs 4/3, 6 및 8에 걸쳐 발달되었음을 보여주었다. 이와 더불어, 코어 04JPC에서 분석된 광물 조성의 변화를 바탕으로, 각 빙하기와 해빙기는 ESIS와 로렌타이드 빙상(Laurentide Ice Sheet)으로부터 확장된 빙붕의 영향이 시공간적으로 다르게 영향을 미쳤던 것으로 해석되었다. 특히, 동시베리아와 척치 주변해역에서 발달되었던 이러한 거대빙하는 대략적으로 MIS 6 북극해 거대빙붕 부피($\sim 4.67 \times 10^6 \text{ km}^3$)의 4분의 1에 해당하며, 이는 범세계적인 해수면을 0.08 m 정도 낮출 수 있는 부피이다. 따라서, 이러한 결과는 제4기 후기동안 지구 기후 및 해수면 변동을 보다 정확히 이해할 수 있는 유용한 정보를 제공한다.

본 학위논문은 고해상도 해저지형, 탄성파층서 및 퇴적물 기록을 종합하여 연구하는 것이 북극 대륙 빙상 및 해양기저빙하에 형성과 관련된 제4기 후기 빙하의 영향을 보다 정확히 이해할 수 있음을 보여주었다. 빙하 역사를 복원하기 위해선, 퇴적물 기록에 대한 정확한 연대정보를 얻는 것이 필수적이다. 탄소연대분석 범위를 넘어선,

보다 과거의 기록에 대한 북극 시층서는 현재까지도 불확실하다. 그러나, 본 학위논문은 최근까지 발전된 층서기록과 잘 일치하는 여러 암층서 인자들을 바탕으로, 서 북극해 척치분지에서 MIS 8 기간을 아우르는 고해상도의 북극 시층서를 제시할 수 있었으며, 이러한 연대정보와 무관하게 본 학위논문의 연구결과는 제4기 후기동안 범세계적인 해수면 변화에 영향을 미칠 수 있는 동시베리아와 척치 주변 해역에 발달되었던 거대빙하의 존재를 입증하는 지질학적 증거를 제공하였다.

감사의 글

해양 퇴적학 및 탄성파층서학 분야에 가르침을 주시고 북극 연구에 매진할 수 있도록 지원해주신 윤석훈 교수님께 먼저 감사드립니다. 연구자로서의 철학과 북극에 대한 이해를 가르쳐주시고, 매우 귀중한 북극해 시료 제공해주시고 북극 빙하역사 및 고환경 복원연구를 위한 기반을 마련해주신 남승일 박사님께 진심으로 감사드립니다. 지금은 은퇴하신 Frank Niessen 박사님을 비롯하여, 서 북극해의 빙하역사에 대한 이해와 가르침을 주신 Leonid Polyak 박사님께 감사하다는 인사를 전해드리며, 북극 스발바르 빙하거동의 이해와 논문 작성에 큰 도움을 주신 트롬소 북극 대학교 Matthias Forwick 교수님과 Jan Sverre Laberg 교수님께 감사드립니다. 학위 논문 작성과 더불어, 저의 푸념과 치열한 토의를 마다하지 않고 들어주셨던 장광철 박사님께도 너무 감사하다는 말씀드립니다. 극지연구소 북극 지질팀에서 연구자로서의 성실함과 태도를 가르쳐주신 김정현 박사님, 팀 내에서 함께 해온 영주누나, 다해씨, 영규, 지금은 부산대에 있는 박광규 박사님에게도 감사의 말씀드립니다.

북극해 맵핑과 탄성파 자료를 잘 활용할 수 있게 큰 도움 주신 홍종국 박사님, 진영근 박사님, 김수관 박사님께 감사의 인사를 드리며, 퇴적물 코어를 능숙하게 다루고 귀중한 분석결과를 만들 수 있게 도와준 문홍수 선생님께도 깊은 감사의 말씀드립니다. 한국지질자원연구원에서 XRF 분석과 입도분석을 흔쾌히 지원해주신 공기수 박사님과 임재수 박사님 감사합니다. 북극 탐사를 같이하며, 많은 토의를 하고 저에게 격려와 조언을 주신 한덕기 교수님, 이동현 박사님께도 감사의 말씀드립니다. 제주대학교 지구해양과학과 환경지질학 실험실에서 석사과정동안 선의의 경쟁을 하며 동거동락한 동기들, 지금은 박사가 된 창성이, 박사학위를 준비하고 있는 우석이, 그리고 재선이형에게 고마웠고, 앞으로도 좋은 동료로서 함께 연구할 수 있는 날이 오기를 기대합니다.

학위를 하는 동안, 부족한 제가 올바른 길을 갈 수 있도록 매일같이 응원해주시고, 걱정해주시고, 믿어주신 부모님께 정말 감사드리고 사랑합니다. 충남대학교에서 박사학위

졸업을 준비하는 형, 분명 잘 할 것이라 믿고, 같이 학업에 정진하여 서로 새로운 연구에 대해 논의하고 함께할 수 있는 날이 오길 진심으로 바랍니다. 마지막으로, 박사학위 심사를 흔쾌히 허락해주시고, 귀중한 조언을 해주신 우경식 교수님과 문재홍 교수님께도 감사드립니다.

